12-2020

Molecular Mechanisms and Design of Hydrogen-Bonded Materials for Thermal Applications

Jinlong He
Utah State University

MOLECULAR MECHANISMS AND DESIGN OF HYDROGEN-BONDED MATERIALS FOR THERMAL APPLICATIONS

by

Jinlong He

A dissertation submitted in partial fulfillment
of the requirements for the degree

of

DOCTOR OF PHILOSOPHY

in

Mechanical Engineering

Approved:

_____	_____
Ling Liu, Ph.D. Major Professor	Hailei Wang, Ph.D. Committee Member
_____	_____
Juhyeong Lee, Ph.D. Committee Member	Nick Roberts, Ph.D. Committee Member
_____	_____
Yi Rao, Ph.D. Committee Member	D. Richard Cutler, Ph.D. Interim Vice Provost of Graduate Studies

UTAH STATE UNIVERSITY
Logan, Utah

2020

ABSTRACT

Molecular Mechanisms and Design of Hydrogen-Bonded Materials

for Thermal Applications

by

Jinlong He, Doctor of Philosophy

Utah State University, 2020

Major Professor: Dr. Ling Liu
Department: Mechanical and Aerospace Engineering

Nano-engineering of biomaterials and energy storage materials often requires an improved understanding of how heat is conducted in these materials at the molecular level. Due to unique size effects, heat transfer at the nanoscale is governed by many factors such as defects, molecular morphology, interfacial properties, and atomic bonding. To guide materials design, it is important to understand the basic mechanism through which those influencing factors control thermal processes. The achieved fundamental knowledge may inspire innovative molecular design of materials to enhance their thermal performance, potentially enabling many practical applications, especially those serving in complex environments controlled by multi-physical factors. In this dissertation, we will systematically demonstrate how different hydrogen bonds and their networks dictate nanoscale thermal transport processes in hydrogen-bonded materials. Several new designs of hydrogen-bonded molecular structures will be probed to modulate their thermal properties.

The hydrogen bond is a special secondary bond that widely exists in many natural and man-made materials including DNA, proteins, polymers, and composite materials. In this work, the study of hydrogen bonding effects on thermal transport will be focused on two representative material systems including (1) protein secondary structures and (2) the electrode/electrolyte interface in solid-state lithium ion batteries. Numerical simulation and theoretical analysis of the thermal transport characteristics will systematically reveal how heat is conducted in the presence of hydrogen bonds. The underlying thermal transport mechanisms will be elaborated by analyzing the molecular structures, vibrational modes and their coupling, phonon density of states, spectral energy density, phonon dispersion relations, and the interfacial power exchange. These results will not only provide a new physical perspective for understanding thermal transport mechanisms in hydrogen-bonded materials, but will also introduce novel concepts of materials design with improved thermal properties towards a broad range of applications.

(165 pages)

PUBLIC ABSTRACT

Molecular Mechanisms and Design of Hydrogen-Bonded Materials

for Thermal Applications

Jinlong He

Heat transfer at the nanoscale plays an important role in determining the reliability and performance of many innovative advanced materials technologies such as nanoelectronics, semiconductor, biomedical devices, polymers, and composites. Extensive efforts have been made to design materials with extraordinary thermal properties. However, fundamental understanding of heat transfer in many of these materials is still not lacking, because the thermal transport processes are governed by several factors including molecular morphology and chemical bonding. Among these factors, the atomic bonding between two dissimilar materials or within single materials is of particular interest due to its ubiquity and importance in physical processes. This work will focus on the demonstration and fundamental understanding of nanoscale thermal transport enhanced by incorporating hydrogen bonds in materials design.

Molecular dynamics is performed for studying heat transfer processes in two typical hydrogen-bonded materials: (1) protein secondary structures, and (2) electrode/electrolyte composites in lithium ion batteries. Theoretical calculation and analysis show that heat transfer can be tuned in a wide range by modifying the hydrogen bonds. Results will not only provide new physical insights, but will also guide the rational design of materials for desired thermal properties towards many applications.

ACKNOWLEDGMENTS

I first give my deepest gratitude to my advisor, Prof. Ling Liu, for giving me an opportunity to work with him. His continuous support throughout my Ph.D. study features so much wisdom, enthusiasm, motivation, patience, insights and immense knowledge. Without his guidance and encouragement, I could not ever complete the Ph.D. work that I have done. He opened the door for me to see many exicting research ideas, develop critical thinking, and pave the way towards a scholarly career. To me, he is not only an advisor on research, but also more like a friend and a role model who is so trustworthy, intellegent, kind, and friendly, providing support to me through all possible means.

I also give my sincere gratitudes to Prof. Juhyeong Lee, Prof. Yi Rao, Prof. Nick Roberts, and Prof. Hailei Wang for taking their precious time to serve in my dissertation committee. I would like to thank Prof. Nick Roberts to help me develop a comprehensive understanding of nanoscale thermal transport. I would like to thank Prof. Hailei Wang for his support and discussions. I would like to thank Prof. Juhyeong Lee for his insightful comments and advices. I would like to thank Prof. Yi Rao for his comments realting to molecular chemistry. I am also grateful to the MAE department chaired by Prof. Zhongquan (Charlie) Zheng for financial support of the last semester.

I would like to futher extend gratitude to all the past and present lab colleagues including Lin Zhang, Alden Hyde, and MD Mohaiminul Islam for my life they filled, the cooperation, and the excellent traits I learned from them. I also would like to thank Dr. Zheyong Fan of Aalto University for fruitful discussion on molecular dynamic simulation.

Besides, I gratefully acknowledge the financial support from the Department of Energy and National Science Foundation through grants awarded to Prof. Ling Liu.

Finally, I also want to express the special appreciation to my dear parents for their support, patience, love, care, and upbringing. I also thank all of my friends who provided help and advices during this journey.

Jinlong He

CONTENTS

Page

LIST OF FIGURES

Figure Page

CHAPTER 1

INTRODUCTION

1.1 Motivations and Practical Significance

1.1.1 Challenges of Nanoscale Thermal Management

Understanding nanoscale thermal transport is crucial to fundamentally describe the energy flow in materials, as well as to achieve many technological applications including thermal management in nanoelectronics and soft electronics, nano-enhanced photovoltaics, thermoelectric devices, nanocomposites and nanoparticle-mediated thermal therapies [1-7]. Since their critical sizes are in the order of nanometers, heat transfer of these technologies is usually dominated by the distribution of phonon mean free path and energy dispersion, and is fundamentally different from that at the micro and macro scales. Nanoscale thermal transport is in the dimension that is comparable to the corresponding mean free path or the wavelength of energy carriers. For example, chip-level power density at the 14nm is usually close to 100 W/cm^2, which can further increase with the scaling of integration and miniaturization [8]. However, the increased power density is usually accompanied by fast battery drain in portable devices and malfunction of devices if an effective cooling technology is not present. Hence, thermal management at the nanoscale is critical to the overall performance of devices. Over the past few decades, driven by renewable energy innovations, numerous studies have been carried out to understand nanoscale thermal transport mechanisms. Many new materials have been engineered with novel microstructures and chemistry at the nanoscale for desired thermal properties [9-11]. Despite this progress, nanoscale heat transfer is still underexplored in many aspects. For example,

to understand the relationship between allosteric communication pathways and energy transport in biological macromolecules [12-14], it is necessary to explore the thermal transfer mechanisms in proteins. Again, one of the major challenges of nanoelectronics is the thermal management in demanding application such as modern technical devices, as these devices can generate a huge amount of heat during operation. If the heat cannot be efficiently removed, devices temperatures increase which will speed up the degradation of their overall performance. These studies provide opportunities to improve the fundamental understanding of thermal physics in advanced materials and to create new materials at the nanoscale.

1.1.2 Importance of Nanoscale Thermal Transport

Heat transfer at the nanoscale significantly differs from that at the macro and micro scales. Firstly, when the device or structural characteristic length is comparable to the phonon mean free path and wavelength of heat carriers [15] (such as electrons, photons, phonons, and molecules), classical heat transfer laws will break down and new approaches have to be developed to predict thermal transport at the nanoscale. Secondly, phonon properties including vibrational modes, group velocity and density of states experience strong size effects, which inevitably affect thermal transport. In addition, heat conduction across heterogeneous interfaces or boundaries at the nanoscale (such as the solid/solid interface, solid/liquid interface, solid/organic interface and grain boundary) plays a major role in determining the overall performance of materials due to the large number of interfaces or grain boundaries that exist in materials. At the nanoscale, heat transfer between two dissimilar materials is usually expounded by phonon transport and scattering.

Phonons usually represent the quantized energy wave related to atomic vibrations. When heat flux is impeded at the interface or grain boundary, thermal resistance is developed due to phonon scattering. Therefore, phonon scattering across interfaces or boundaries is a key factor at the nanoscale, which significantly governs thermal transport processes [16-18].

1.1.3 Atomic-Level Design with Hydrogen Bond

In this dissertation, the interface within the same material and that between two dissimilar materials are explored [16-18].

When heat is transferred across an interface within the same material, e.g. the interface between molecular chains that comprise β-sheets of proteins, the effect of interchain and intrachain interactions on thermal transport processes can usually be described by the Frenkel-Kontorova lattice model [19-22]. In this model, the non-bonded interactions are described as either harmonic springs or van der Waals interactions. Studies have shown that thermal conductivity will increase with the strengthened non-bonded interactions [23-25]. The interchain covalent bonding is described as on-site potentials, and thermal conductivity increases with the increased strength of covalent bonding when the potential is larger than 10.0 [23]. Moreover, numerous studies have proved that stronger non-bonded interactions can improve the thermal conductivity of layered or bundled materials such as bundled carbon nanotubes [26], crystalline polymer nanofibers [27], few-layer graphene [28, 29], β-sheets proteins [24, 25], multilayer boron nanoribbons [30], cross-linked polymers [31] and multi-walled carbon nanotubes [32]. These investigations show that thermal conductivity can be improved by enhancing the intrachain, interchain or interlayer interactions.

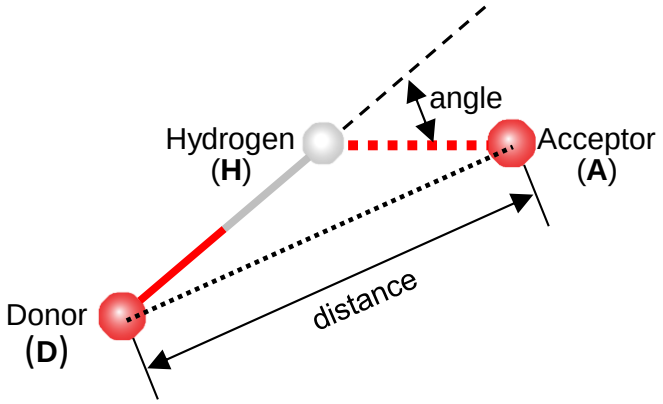

Figure 1.1 The representative configuration of a hydrogen bond (red dashed line).

When heat is transferred across interfaces between two disimilar materials, such as the crystal/crystal interface [33], solid/gas interface [34, 35], liquid/surfactant interface [36], solid/polymer interface [37-39], solid/liquid interface [40-42], and solid/self-assembled monolayer/solid interface [43-45], the effects of interfacial bonding on heat transfer have been widely explored by molecular dynamics simulations and experiments. These studies have demonstrated that the relationship between thermal conductance across interfaces and the strength of interfacial bonding is correlated in a linear fashion, which is also well in accordance with the experiments [46]. These findings indicate that the interfacial thermal conductance between dissimilar materials can be improved by ehancing interfacial bonding.

The above discussions indicate that thermal transport processes across the same material or between two dissimilar materials can be tuned by modifying the strength of non-bonded interactions. In chemistry, non-bonded interactions mainly include the van der Waals interaction, hydrogen bonding, and electrostatic interaction. A hydrogen bond (denoted as D-H…A) is a secondary bond, as shown in **Figure 1.1**, which forms between a hydrogen atom (H) which is covalently bonded to a more electronegative atom, namely

the donor (D), and another nearby highly electronegative atom, namely the acceptor (A) [47-49]. Importantly, the strength of hydrogen bonds is stronger than van der Waals interaction by 1~2 orders of magnitude, within a range from 10 to 100 kJ mol^{-1} [47, 48, 50]. In this work, we mainly focus on how to achieve desired thermal properties by materials design and interface design in combination with hydrogen bonding.

The hydrogen bond is a ubiquitous and fundamental component at the atomic level, as shown in **Figure 1.2**. It widely exists in many materials in our daily life including water, proteins, DNA, polymers, and so on. Further, hydrogen bonds can also influence properties of materials. For example, water's boiling point is as high as 100 °C due to hydrogen bonds. The Kevlar material is so tough making them ideal for making body armors due to the hydrogen bonds. Hydrogen bonds also play a key role in proteins and DNA structures because it stabilizes protein secondary structures such as the beta sheets, alpha helix, some turns and loops. The hydrogen bond can also serve as a bridge that binds the polar group of polymers with water, developing hydrogels with higher mechanical and thermal properties [51]. Besides, hydrogen bonds can also be used to improve other properties of materials [52]. Therefore, hydrogen bonds provide a novel path for designing materials to achieve outstanding mechanical and thermal properties at the atomic level.

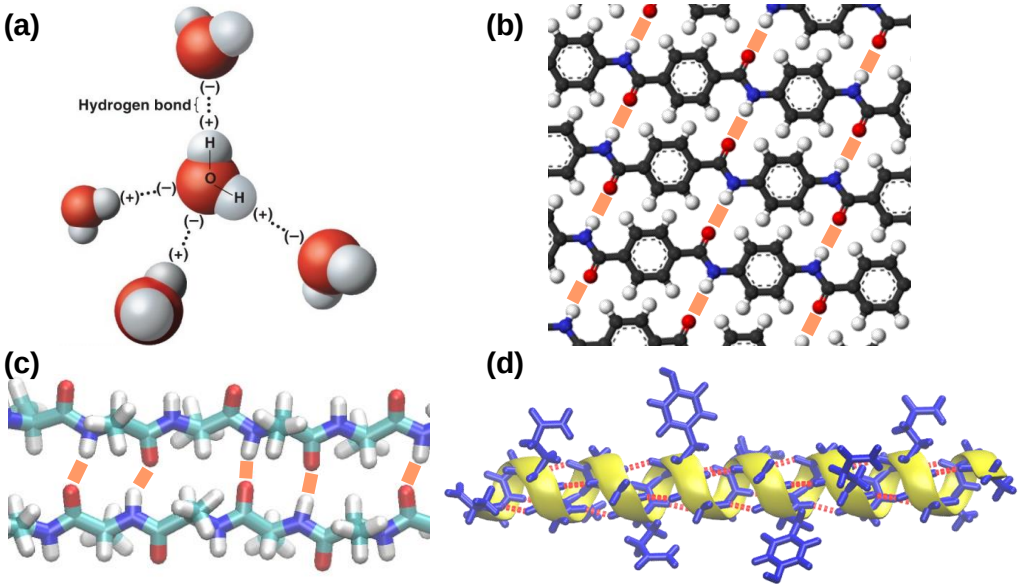

Figure 1.2. Hydrogen bonds (red dashed line) exist in various materials including (a) water, (b) Kevlar polymer, (c) beta sheets, and (d) helical protein structure.

1.1.4 Applications of Hydrogen Bonds in Materials Design

Both experiments and theoretical studies have provided evidences that hydrogen bonds can improve heat transfer efficiency by reinforcing the existing thermal pathways and developing new ones. In addition, thermal properties of materials can influence their overall functionality and reliability, and can be described by their thermal conductivities. For example, as shown in **Figure 1.3**a-b, polymers usually have very low thermal conductivties, e.g. 0.1-0.5 W m^{-1} K^{-1} for poly(acrylic acid) (PAA) and poly(N-acryloyl piperidine) (PAP). Interestingly, studies have indicated that a blend of the two polymers can induce a thermal network with dense and homogeneous distribution due to their high miscibility. Thermal conductivity of the polymer blend shows a sharp increase due to the formed inter/intra-chain hydrogen bonds, reaching over 1.5 W m^{-1} K^{-1}, an order of magnitude higher than that of the constituent polymers or other amorphous polymers [53].

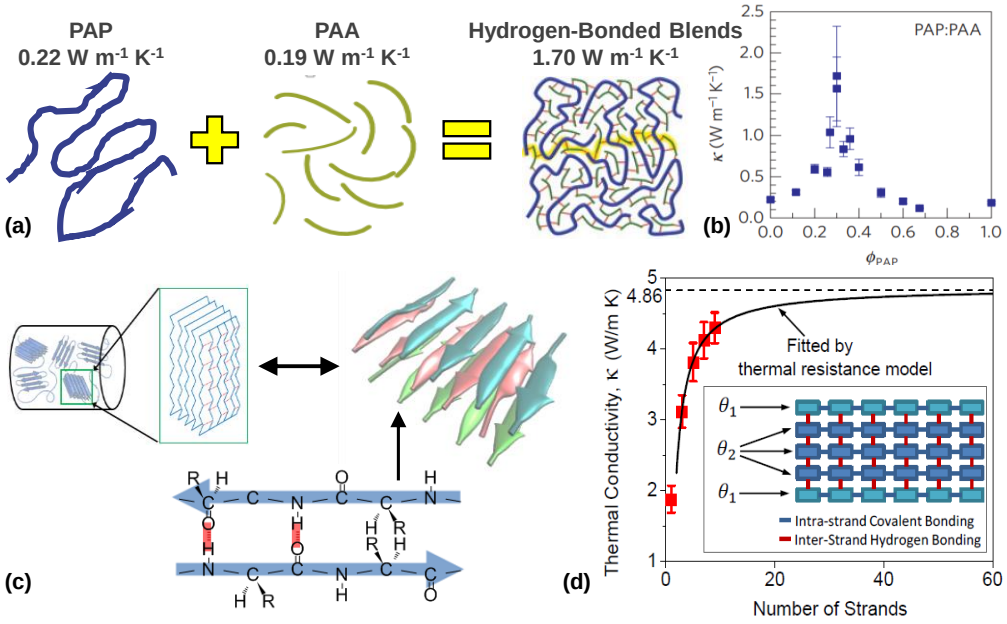

Figure 1.3. Applications of hydrogen bond in material design to improve thermal conductivity. (a) Hydrogen bonds serve as the percolation thermal pathway (yellow) in mixture of PAP and PAA polymer, and (b) The measured thermal conductivity of spin-cast PAP:PAA at various fractions of PAP polymer [53]. (c) Dragline comprises numerous β-sheet crystal units embedded in an amorphous matrix, and each β-sheet consists of β-strands interlocked by hydrogen bonding, and (d) Thermal conductivities of 16-alanine β-sheets calculated by molecular dynamic simulation (red squares) and a thermal resistance model (black curve). Thermal resistance model is shown as the inset. Thermal resistances of exterior and interior strands are defined by θ_1 and θ_2, respectively [25].

Another example is the protein secondary structures, e.g. β-sheet as shown in **Figure 1.3**c-d, which is an essential building block of spider silk protein. Studeis have demonstrated that thermal conductivity of β-sheet is 1-2 orders of magnitude higher than that of other protein structures studied in literature due to the presence of hydrogen bonds, which shows that hydrogen bonds can improve the nanoscale thermal transport of materials [25]. More importantly, In comparsion with some other similar bundled and layered structures, such as bundled carbon nanotudes and few-layer graphene, β-sheet still shows an increased

thermal conductivity due to the role of hydrogen bonds with the increase of the number of constituting units, such as β-strand.

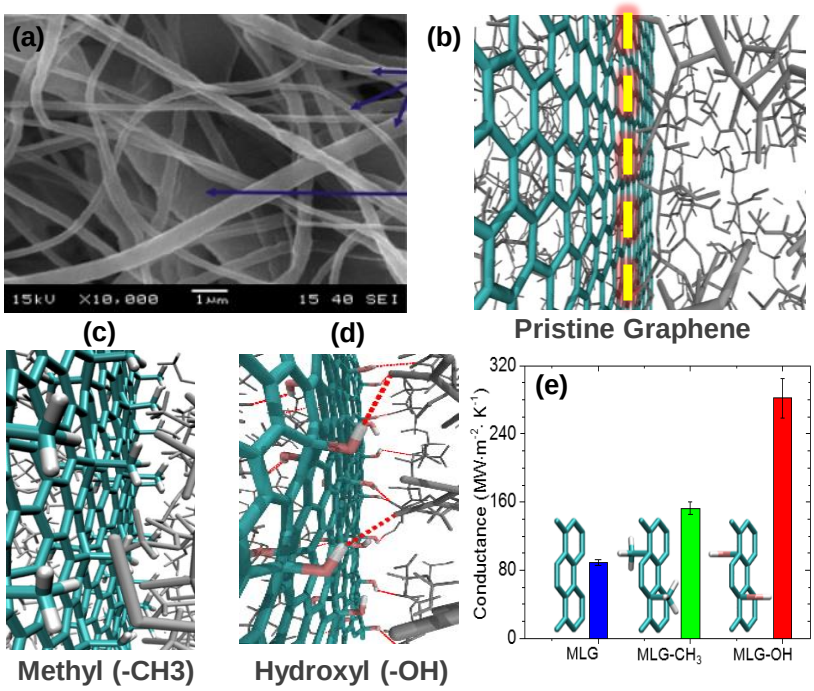

Figure 1.4. (a) SEM image of graphene/polymer composites [54], in which the blue arrows denote the interface between graphene and polymer. Applications of hydrogen bonds in interface design [38] for (b) the pristine interface between graphene (cyan) and polymer (gray), (c) the interface between methyl-functionalized graphene and polymer, (d) the interface between hydroxyl-functionalized graphene and polymer with numerous hydrogen bonds (red dashed lines). (e) Interfacial thermal conductance for case (b), (c) and (d).

1.1.5 Applications of Hydrogen Bonds in Interfaces Design

Both theoretical analysis and experiment have indicated that thermal properties of heterogeneous materials can be obviously improved by assembling hydrogen bonds onto their interfaces. Here, hydrogen bonds can serve as a bridge for linking the two heterogeneous materials. Then the interfacial heat transfer efficiency will be improved as a result of the developed new pathway and the strengthened original pathway. As shown

in **Figure 1.4**, experiment shows that amorphous polymethyl methacrylate (PMMA) polymer has a low thermal conductivity, about 0.2 W m^{-1} K^{-1} [55]. Instead, carbon nanotubes has a thermal conductivity within the range of 2000-6600 W m^{-1} K^{-1} [56] and graphene shows a super-high thermal conductivity in the range of 4840-5300 W m^{-1} K^{-1} at room temperature [57]. Despite graphene and carbon nanotubes have the superior thermal conductivity, studies have demonstrated that thermal conductivtiy of polymeric nanocomposites incorporated carbon nanotubes or graphene is only in the order of 10 W m^{-1} K^{-1}, which is much lower than that of their constituents and not improved as much as our expected [58, 59]. Further studies have shown that the drastic discrepancy is attributed to the high interfacial thermal resistance between polymeric matrix and the embeded materials [60]. To improve the interfacial thermal conductance, the general route is to improve the interfacial bonding between the two dissimilar materials, and this is where hydrogen bonds can play a big role. However, when the interface between graphene and PMMA is functionalized by different functional groups, as shown in **Figure 1.4**, studies show that the interface functionalized with hydroxyl group has the highest thermal conductance since it forms hydrogen bonds at the interface [38].

1.2 Material Systems and Objectives

In this dissertation, two representative material systems, such as protein secondary structure and electrode/electrolyte interface in solid-state Li ion battery, will be employed to demonstrate how hydrogen bonds guide the thermal transport process in nanostructures, and what role hydrogen bonds play in thermal transfer across material interfaces. For the protein secondary structure, three typical structures including 3_{10}-helix, α-helix and π-helix

are employed for studying how hydrogen bond configuration affects nanoscale thermal transport. Besides, the effect of side-chain mass on heat transfer in protein secondary structures is also considered. For electrode/electrolyte interface in the solid-state Li ion battery, due to mechanically dissimilar materials across the electrode/electrolyte interface, it is necessary to explore how hydrogen bonds improve the thermal conductance across their interfaces. Also, to better understand thermal conductance across the electrode/electrolyte interface, thermal properties of electrode materials are also considered.

1.2.1 Protein Secondary Structures

The vast functional duties of proteins (from structural building blocks to molecular recognition, conformational changes, enzyme catalysis, conformational changes, intermolecular affinities and energy transduction [61-66]) are governed or influenced by energetic vibrations of the biomolecules. Thus, the connection between protein structures and the energy flow pathway is a fundamental question that dictates protein functionality and reactivity. To guide the functionality and reactivity of proteins, the first and foremost task is to understand the heat transfer process of proteins in bioprocesses.

In addition to their fundamental importance in bioprocesses, proteins present a virtually unexplored avenue to study the fundamentals of thermal transport in naturally occurring nanostructured, percolating networks. To date, thermal conduction in biological materials has often been explored in the context of amorphous solids and evaluated through comparison with some variations of the so-called “minimum limit to thermal conductivity” at elevated temperatures as well as data from atomistic molecular dynamics simulations [67-71].

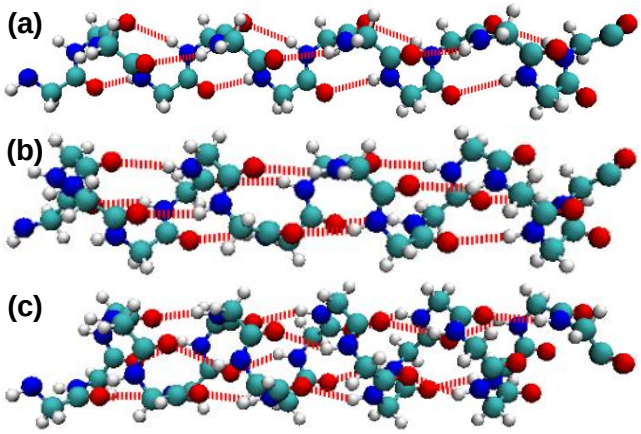

Figure 1.5. Three isomers of poly-G helices: (a) 3_{10} helix, (b) α-helix and (c) π-helix (cyan color: the backbone with carbon atoms; blue color: backbone with nitrogen atoms; white color: side chain with hydrogen atoms; red color: side chain with oxygen atoms; and the red dashed lines denote the H-bonds).

Numerus efforts have been made to study the energy flow in proteins and its relationship with protein dynamics [25, 72-76]. Research on heat flow in different structures, such as peptide helices [75], heme cofactors [76], beta sheets [25] and functionalized materials [77, 78] have been reported in the literature. These reports have shown that the excess of energy deposited in particular sites can propagate along structures through the covalent backbone of molecules [75, 78] and also through weaker interactions, such as hydrogen bonds [25, 77]. Hydrogen bonds have been an inexhaustible source of research for decades [79]. Their role as stabilizing agents of protein structures have been clearly established [80]. Also, they can modulate the chemical reactivity of proteins [81] and, as has been earlier proposed from the field of physics, can also serve as energy carriers in protein structures [82]. Therefore, how to mediate their structural determinants is of major importance to improve energy transfer among different parts of proteins.

Structurally, Protein "nanowires" as shown in **Figure 1.5**, differ from many other inorganic nanowires and nanotubes in that they feature tortuous covalent pathways "reinforced" by H-bonds as "stiffeners." Proteins of the same sequence may form different types of helices depending on how H-bonds are formed in **Figure 1.5**. In the 3_{10}-helix, the carbonyl group in residue *i* is H-bonded with the nitrogen in residue *i*+3, and in the α-helix, the carbonyl group in residue *i* is H-bonded with the nitrogen in residue *i*+4. However, in the π-helix, the carbonyl group in residue *i* is H-bonded with the nitrogen in residue *i*+5. The different H-bond locations make the 3_{10}-helix longer and thinner than its α-helix and π-helix counterpart. Similar to black/blue phosphorene [83], the two helices must also have distinct thermal transport characteristics. Nevertheless, the thermal transport mechanism of proteins with the same amine acid sequence but different hydrogen bond configuration still remains unknown.

Studies have shown that hydrogen bonds can underpin the thermal transport by influencing molecular structures, interfacial bonding and phonon transport. Here, three protein helical isomers including 3_{10}-helix, α-helix and π-helix have the same protein sequence and different hydrogen bond locations. The more tightly "twisted" 3_{10}-helix is hypothesized to have a higher thermal conductivity along the length than α-helix and π-helix. The amorphous phase of the three protein helical isomers will be excluded from our discussion, despite the fact that they also includes hydrogen bonds. Compared with the 3_{10}-helix, α-helix and π-helix, the amorphous phase in proteins is typically associated with more phonon scattering and shorter phonon mean free path, which are expected to significantly reduce thermal conductivities [84]. Furthermore, based on the intimate relation

between thermal conductivity and elasticity [85], 3_{10}-helix, α-helix and π-helix crystals are assumed to be good thermal conductors. As a result, this dissertation will focus on their nanocrystals, and their amorphous phase are not considered.

This work will first focus on how different hydrogen bond configurations affect heat transfer process in proteins with the same amine acid sequence. In addition to this, being able to manipulate the amine acid sequence of side chains makes it possible to change the way that hydrogen bonds hold the secondary structures and tune material properties. Specifically, hydrogen bonds, denoted by N-H…O=C in protein, can be easily designed between the amino acids. However, it is relatively unknown how heat flow in protein secondary structures is manipulated by different side-chain groups. Understanding the underlying transport mechanisms will not only provide novel insights into thermal properties of proteins and biomaterials, but may also open a new door for designing the synthetic silk or other proteins [86-88] to achieve desired thermal properties for a wide range of biomedical applications.

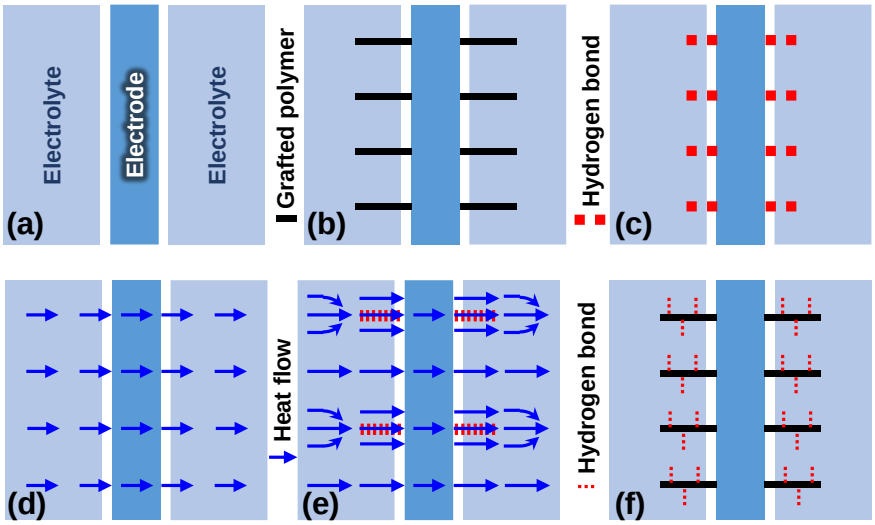

Figure 1.6. Schematics of (a) a pristine electrode/electrolyte interface, (b) the electrode/electrolyte interface functionalized by polymer (without hydrogen bonds), and (c) the electrode/electrolyte interface functionalized by polymers (with hydrogen bonds). (d) Heat flow without hydrogen bonds. (e) Hypothesized heat flow with hydrogen bonds providing some new thermal pathways. (f) Heat transfer by hierarchical hydrogen bond network combining (b) and (c).

1.2.2 Electrode/Electrolyte Nanocomposites

Recently, experiments have shown that interfacial thermal conduction between the inorganic cathode and the organic electrolyte contributes 88% to the overall thermal resistance of a Li ion battery; and chemical bridging at the interface leads to four times reduction in the thermal contact resistance [89]. On the other hand, significant efforts have been made to improve thermal conductivities of polymers by incorporating other materials with low-dimensions and high thermal conductivities such as graphene [58] and carbon nanotube [59]. However, thermal conductivities of such composites were found to be significantly lower than expectations by the effective medium theory [90, 91], mainly due to the high interfacial thermal resistance on the order of 10^{-8} $m^2 K / W$ [92, 93] caused by phonon scattering [94, 95]. Techniques using covalent [96] and non-covalent interactions [97-99] have been introduced to improve interfacial thermal conduction. At the interfaces, heat flow is inhibited due to weak interfacial interactions. To facilitate thermal transport across the interfaces, enormous efforts have been made including grafting polymer chains [89 100] and tailoring phonon modes with functionalization [101].

In this work, Lithium cobalt oxide ($LiCoO_2$) and polyethylene oxide (PEO) are respectively chosen as the electrode and electrolyte. At the pristine electrode/electrolyte interface (**Figure 1.6**a), the van der Waals interaction (**Figure 1.6**d) between the electrode and electrolyte controls heat transfer across the interface, while conduction is inefficient

due to the weak van der Waals interaction. To reinforce the vibrational coupling between the electrode and electrolyte, polymer chains (**Figure 1.6**b) with different functional groups will be incorporated to electrode surfaces. These polymer chains with different functional groups are used for functionalizing the electrode surface, serving as "molecular bridges" between the electrolyte and electrode to improve the interfacial thermal conduction. Morphology for these functional polymer chains is governed by their length and stiffness. Recent advances in surface functional groups, particularly covalent modifications, permit persistent alteration of the interfaces. The study will provide additional insights to extend the application of low-dimensional materials, and open an avenue to engineer hydrogen-bonded supramolecular carbon structures for new properties that are otherwise not achievable [102-104].

Our hypothesis is that hydrogen bonds can reinforce the nanoscale thermal transport normal to the material interface (**Figure 1.6**c) by developing some new pathways to conduct heat (**Figure 1.6**e). By incorporating polymer-functionalized electrode materials (**Figure 1.6**b) and hydrogen-bonded interfaces (**Figure 1.6**c), a hierarchical design concept will be proposed as illustrated in **Figure 1.6**f. Some key parameters including the chain length, chain morphology, chain type and number of hydrogen bonds will be optimized for obtaining the desirable thermal properties.

1.3 Significance of the Proposed Research

Our research efforts will yield new physical insights into the role of hydrogen bonds in nanoscale thermal transport through hydrogen-bonded materials including proteins, polymers, and nanocomposite interfaces. Material designs that garner the improved

fundamental understanding may lead to novel synthetic proteins, and nanocomposites with tunable thermal properties. Thermally conductive materials with better biocompatibility may solve some key issues in cancer treatment [105] and nanoelectronics [106]. The improved understanding of the thermal transport phenomena will accelerate design stability, development, and deployment. The obtained knowledge will enrich the understanding of hydrogen bond physics, nanoscale thermal transport, allosteric communication pathways in protein, and thermal mangagement in Li ion battery.

1.4 Structural Organization of This Dissertation

This dissertation is constructed in the form of multi-papers. Each chapter displayed as follows either has been published as a paper in one journal or has been submitted as a paper in a journal. References are listed by chapters and placed at the end. Supplementary materials of each chapter are exhibited at the end of this dissertation according to the order of chapters.

A summary of each chapter is stated as follows, each of which will be described in more detail in the upcoming sections of this dissertation. Chapter 2 investigates the thermal properties of an electrode material (lithium cobalt oxide) as the monocrystal, polycrystal, and at grain boundaries. Chapter 3 focuses on improving the thermal conductance across the electrode/electrolyte interface by using a hierarchical hydrogen bonds network. Chapter 4 mainly explores how hydrogen bond configurations affect nanoscale thermal transport in helical protein nanotubes such as the 3_{10}-helix, α-helix and π-helix nanocrystals in protein secondary structures. The effects of side-chain mass on thermal transport in hydrogen-

bonded protein systems are discussed in Chapter 5. Finally, conclusions and recommendations of future work are summerized in Chapter 6.

REFERENCES

[1] Ghosh, S., Calizo, I., Teweldebrhan, D., Pokatilov, E. P., Nika, D. L., Balandin, A. A., Bao, W., Miao, F., and Lau, C. N., 2008, "Extremely high thermal conductivity of graphene: Prospects for thermal management applications in nanoelectronic circuits," Applied Physics Letters, 92(15), p. 151911.

[2] Akinwande, D., Petrone, N., and Hone, J., 2014, "Two-dimensional flexible nanoelectronics," Nature Communications, 5, p. 5678.

[3] Dominguez, M., Vian, J. G., Astrain, D., Esarte, J., Aldave, L., and Aguas, J., "Thermoelectric device to measure the thermal conductivity of materials," Proc. Twenty-First International Conference on Thermoelectrics, 2002. Proceedings ICT '02., pp. 341-344.

[4] Allan, J., Pinder, H., and Dehouche, Z., 2016, "Enhancing the thermal conductivity of ethylene-vinyl acetate (EVA) in a photovoltaic thermal collector," AIP Advances, 6(3), p. 035011.

[5] Huang, C., Qian, X., and Yang, R., 2018, "Thermal conductivity of polymers and polymer nanocomposites," Materials Science and Engineering: R: Reports, 132, pp. 1-22.

[6] Xu, X., Chen, J., Zhou, J., and Li, B., 2018, "Thermal Conductivity of Polymers and Their Nanocomposites," Advanced Materials, 30(17), p. 1705544.

[7] Krishnan, S., Diagaradjane, P., and Cho, S. H., 2010, "Nanoparticle-mediated thermal therapy: evolving strategies for prostate cancer therapy," Int J Hyperthermia, 26(8), pp. 775-789.

[8] Pop, E., Sinha, S., and Goodson, K. E., 2006, "Heat Generation and Transport in Nanometer-Scale Transistors," Proc. IEEE, 94(8), pp. 1587-1601.

[9] Cahill, D. G., Braun, P. V., Chen, G., Clarke, D. R., Fan, S. H., Goodson, K. E., Keblinski, P., King, W. P., Mahan, G. D., Majumdar, A., Maris, H. J., Phillpot, S. R., Pop, E., and Shi, L., 2014, "Nanoscale thermal transport. II. 2003-2012," Appl Phys Rev, 1(1).

[10] Cahill, D. G., Ford, W. K., Goodson, K. E., Mahan, G. D., Majumdar, A., Maris, H. J., Merlin, R., and Sr, P., 2003, "Nanoscale thermal transport," J Appl Phys, 93(2), pp. 793-818.

[11] Leitner, D. M., 2008, "Energy flow in proteins," Annu Rev Phys Chem, 59, pp. 233-259.

[12] Burendahl, S., and Nilsson, L., 2012, "Computational studies of LXR molecular interactions reveal an allosteric communication pathway," Proteins, 80(1), pp. 294-306.

[13] Miño-Galaz, G. A., 2015, "Allosteric Communication Pathways and Thermal Rectification in PDZ-2 Protein: A Computational Study," The Journal of Physical Chemistry B, 119(20), pp. 6179-6189.

[14] Ota, N., and Agard, D. A., 2005, "Intramolecular signaling pathways revealed by modeling anisotropic thermal diffusion," J Mol Biol, 351(2), pp. 345-354.

[15] Chen, G., "Nanoscale Energy Transport and Conversion: A Parallel Treatment of Electrons, Molecules, Phonons, and Photons."

[16] Cahill, D. G., Braun, P. V., Chen, G., Clarke, D. R., Fan, S., Goodson, K. E., Keblinski, P., King, W. P., Mahan, G. D., Majumdar, A., Maris, H. J., Phillpot, S. R., Pop, E., and Shi, L., 2014, "Nanoscale thermal transport. II. 2003–2012," Appl. Phys. Rev., 1(1), p. 011305.

[17] Cahill, D. G., Ford, W. K., Goodson, K. E., Mahan, G. D., Majumdar, A., Maris, H. J., Merlin, R., and Phillpot, S. R., 2002, "Nanoscale thermal transport," J. Appl. Phys., 93(2), pp. 793-818.

[18] Maldovan, M., 2012, "Transition between ballistic and diffusive heat transport regimes in silicon materials," Appl. Phys. Lett., 101(11), p. 113110.

[19] Ai, B.-q., and Hu, B., 2011, "Heat conduction in deformable Frenkel-Kontorova lattices: Thermal conductivity and negative differential thermal resistance," Physical Review E, 83(1), p. 011131.

[20] Zhong, W.-R., 2010, "Different thermal conductance of the inter- and intrachain interactions in a double-stranded molecular structure," Physical Review E, 81(6), p. 061131.

[21] Sun, T., Wang, J., and Kang, W., 2013, "Van der Waals interaction-tuned heat transfer in nanostructures," Nanoscale, 5(1), pp. 128-133.

[22] Díaz, E., Gutierrez, R., and Cuniberti, G., 2011, "Heat transport and thermal rectification in molecular junctions: A minimal model approach," Phys. Rev. B, 84(14), p. 144302.

[23] Zhong, W.-R., 2010, "Different thermal conductance of the inter- and intrachain interactions in a double-stranded molecular structure," Phys. Rev. E Stat. Nonlin. Soft Matter Phys., 81, p. 061131.

[24] Zhang, L., Bai, Z., Ban, H., and Liu, L., 2015, "Effects of the amino acid sequence on thermal conduction through β-sheet crystals of natural silk protein," PCCP, 17(43), pp. 29007-29013.

[25] Zhang, L., Chen, T., Ban, H., and Liu, L., 2014, "Hydrogen bonding-assisted thermal conduction in β-sheet crystals of spider silk protein," Nanoscale, 6(14), pp. 7786-7791.

[26] Hone, J., Batlogg, B., Benes, Z., Johnson, A. T., and Fischer, J. E., 2000, "Quantized Phonon Spectrum of Single-Wall Carbon Nanotubes," Science, 289(5485), p. 1730.

[27] Zhang, L., Ruesch, M., Zhang, X., Bai, Z., and Liu, L., 2015, "Tuning thermal conductivity of crystalline polymer nanofibers by interchain hydrogen bonding," RSC Adv., 5(107), pp. 87981-87986.

[28] Ghosh, S., Bao, W., Nika, D. L., Subrina, S., Pokatilov, E. P., Lau, C. N., and Balandin, A. A., 2010, "Dimensional crossover of thermal transport in few-layer graphene," Nat. Mater., 9(7), pp. 555-558.

[29] Singh, D., Murthy, J. Y., and Fisher, T. S., 2011, "Mechanism of thermal conductivity reduction in few-layer graphene," J. Appl. Phys., 110(4), p. 044317.

[30] Yang, J., Yang, Y., Waltermire, S. W., Wu, X., Zhang, H., Gutu, T., Jiang, Y., Chen, Y., Zinn, A. A., Prasher, R., Xu, T. T., and Li, D., 2012, "Enhanced and switchable nanoscale thermal conduction due to van der Waals interfaces," Nat. Nanotechnol., 7(2), pp. 91-95.

[31] Rashidi, V., Coyle, E. J., Sebeck, K., Kieffer, J., and Pipe, K. P., 2017, "Thermal Conductance in Cross-linked Polymers: Effects of Non-Bonding Interactions," J. Phys. Chem. B, 121(17), pp. 4600-4609.

[32] Pettes, M. T., and Shi, L., 2009, "Thermal and Structural Characterizations of Individual Single-, Double-, and Multi-Walled Carbon Nanotubes," Adv. Funct. Mater., 19(24), pp. 3918-3925.

[33] Shen, M., Evans, W., Cahill, D., and Keblinski, P., 2011, "Bonding and pressure-tunable interfacial thermal conductance," Phys. Rev. B, 84.

[34] Hwang, G. S., and Kaviany, M., 2009, "Molecular dynamics simulation of effective thermal conductivity of vapor-filled nanogap and nanocavity," J. Appl. Phys., 106(2), p. 024317.

[35] Zhang, L., Song, Z., Zhao, B., Villarreal, E., and Ban, H., 2020, "Fast atom effect on helium gas/graphite interfacial energy transfer," Carbon, 161, pp. 206-218.

[36] Shenogina, N., Godawat, R., Keblinski, P., and Garde, S., 2009, "How Wetting and Adhesion Affect Thermal Conductance of a Range of Hydrophobic to Hydrophilic Aqueous Interfaces," Phys. Rev. Lett., 102(15), p. 156101.

[37] Hu, M., Keblinski, P., and Schelling, P. K., 2009, "Kapitza conductance of silicon--amorphous polyethylene interfaces by molecular dynamics simulations," Phys. Rev. B, 79(10), p. 104305.

[38] Zhang, L., Bai, Z., and Liu, L., 2016, "Exceptional Thermal Conductance across Hydrogen-Bonded Graphene/Polymer Interfaces," Adv. Mater. Interfaces, 3(13), p. 1600211.

[39] Zhang, L., and Liu, L., 2019, "Hierarchically hydrogen-bonded graphene/polymer interfaces with drastically enhanced interfacial thermal conductance," Nanoscale, 11(8), pp. 3656-3664.

[40] Ramos-Alvarado, B., Kumar, S., and Peterson, G. P., 2016, "Solid–Liquid Thermal Transport and Its Relationship with Wettability and the Interfacial Liquid Structure," The Journal of Physical Chemistry Letters, 7(17), pp. 3497-3501.

[41] Han, H., Schlawitschek, C., Katyal, N., Stephan, P., Gambaryan-Roisman, T., Leroy, F., and Müller-Plathe, F., 2017, "Solid–Liquid Interface Thermal Resistance Affects the Evaporation Rate of Droplets from a Surface: A Study of Perfluorohexane on Chromium Using Molecular Dynamics and Continuum Theory," Langmuir, 33(21), pp. 5336-5343.

[42] Giri, A., Braun, J. L., and Hopkins, P. E., 2016, "Implications of Interfacial Bond Strength on the Spectral Contributions to Thermal Boundary Conductance across Solid, Liquid, and Gas Interfaces: A Molecular Dynamics Study," The Journal of Physical Chemistry C, 120(43), pp. 24847-24856.

[43] Hu, L., Zhang, L., Hu, M., Wang, J.-S., Li, B., and Keblinski, P., 2010, "Phonon interference at self-assembled monolayer interfaces: Molecular dynamics simulations," Phys. Rev. B, 81(23), p. 235427.

[44] Luo, T., and Lloyd, J. R., 2010, "Non-equilibrium molecular dynamics study of thermal energy transport in Au–SAM–Au junctions," Int. J. Heat Mass Transfer, 53(1), pp. 1-11.

[45] Tian, Z., Marconnet, A., and Chen, G., 2015, "Enhancing solid-liquid interface thermal transport using self-assembled monolayers," Appl. Phys. Lett., 106, p. 211602.

[46] Ge, Z., Cahill, D. G., and Braun, P. V., 2006, "Thermal Conductance of Hydrophilic and Hydrophobic Interfaces," Phys. Rev. Lett., 96(18), p. 186101.

[47] Aakeröy, C. B., and Seddon, K. R., 1993, "The hydrogen bond and crystal engineering," Chem. Soc. Rev., 22(6), pp. 397-407.

[48] Steiner, T., 2002, "The Hydrogen Bond in the Solid State," Angew. Chem. Int. Ed., 41(1), pp. 48-76.

[49] Elangannan, A., Gautam, R. D., Roger, A. K., Joanna, S., Steve, S., Ibon, A., David, C. C., Robert, H. C., Joseph, J. D., Pavel, H., Henrik, G. K., Anthony, C. L., Benedetta, M., and David, J. N., 2011, "Definition of the hydrogen bond (IUPAC Recommendations 2011)," Pure Appl. Chem., 83(8), pp. 1637-1641.

[50] Perrin, C. L., and Nielson, J. B., 1997, "“STRONG” HYDROGEN BONDS IN CHEMISTRY AND BIOLOGY," Annu. Rev. Phys. Chem., 48(1), pp. 511-544.

[51] Guo, M., Pitet, L. M., Wyss, H. M., Vos, M., Dankers, P. Y. W., and Meijer, E. W., 2014, "Tough Stimuli-Responsive Supramolecular Hydrogels with Hydrogen-Bonding Network Junctions," J. Am. Chem. Soc., 136(19), pp. 6969-6977.

[52] Keten, S., Xu, Z., Ihle, B., and Buehler, M. J., 2010, "Nanoconfinement controls stiffness, strength and mechanical toughness of β-sheet crystals in silk," Nat. Mater., 9(4), pp. 359-367.

[53] Kim, G.-H., Lee, D., Shanker, A., Shao, L., Kwon, M. S., Gidley, D., Kim, J., and Pipe, K. P., 2015, "High thermal conductivity in amorphous polymer blends by engineered interchain interactions," Nat. Mater., 14(3), pp. 295-300.

[54] Jiang, X., and Drzal, L. T., 2012, "Multifunctional high-density polyethylene nanocomposites produced by incorporation of exfoliated graphene nanoplatelets 2: Crystallization, thermal and electrical properties," Polym. Compos., 33(4), pp. 636-642.

[55] Assael, M. J., Botsios, S., Gialou, K., and Metaxa, I. N., 2005, "Thermal Conductivity of Polymethyl Methacrylate (PMMA) and Borosilicate Crown Glass BK7," Int. J. Thermophys., 26(5), pp. 1595-1605.

[56] Berber, S., Kwon, Y.-K., and Tománek, D., 2000, "Unusually High Thermal Conductivity of Carbon Nanotubes," Phys. Rev. Lett., 84(20), pp. 4613-4616.

[57] Balandin, A. A., Ghosh, S., Bao, W., Calizo, I., Teweldebrhan, D., Miao, F., and Lau, C. N., 2008, "Superior Thermal Conductivity of Single-Layer Graphene," Nano Lett., 8(3), pp. 902-907.

[58] Potts, J. R., Dreyer, D. R., Bielawski, C. W., and Ruoff, R. S., 2011, "Graphene-based polymer nanocomposites," Polymer, 52(1), pp. 5-25.

[59] Han, Z., and Fina, A., 2011, "Thermal conductivity of carbon nanotubes and their polymer nanocomposites: A review," Prog. Polym. Sci., 36(7), pp. 914-944.

[60] Wojtaszek, M., Tombros, N., Caretta, A., van Loosdrecht, P. H. M., and van Wees, B. J., 2011, "A road to hydrogenating graphene by a reactive ion etching plasma," J. Appl. Phys., 110(6), p. 063715.

[61] Stern, H. A., 2010, "Proteins: Energy, Heat, and Signal Flow," Journal of the American Chemical Society, 132(11), pp. 4030-4030.

[62] Wergin, W., 2006, Essential cell biology (2nd edition). By Bruce Alberts, Dennis Bray, Karen Hopkin, Alexander Johnson, Julian Lewis, Martin Raff, Keith Roberts, Peter Walter. Garland Science/Taylor and Francis Group, New York and London (2003). ISBN 0-8153-3480-X; hardbac.

[63] Kukura, P., McCamant, D. W., Yoon, S., Wandschneider, D. B., and Mathies, R. A., 2005, "Structural Observation of the Primary Isomerization in Vision with Femtosecond-Stimulated Raman," Science, 310(5750), p. 1006.

[64] Engel, G. S., Calhoun, T. R., Read, E. L., Ahn, T.-K., Mančal, T., Cheng, Y.-C., Blankenship, R. E., and Fleming, G. R., 2007, "Evidence for wavelike energy transfer through quantum coherence in photosynthetic systems," Nature, 446, p. 782.

[65] Champion, P. M., 2005, "Following the Flow of Energy in Biomolecules," Science, 310(5750), p. 980.

[66] Miller, R. J. D., 1991, "Vibrational Energy Relaxation and Structural Dynamics of Heme Proteins," Annu. Rev. Phys. Chem., 42(1), pp. 581-614.

[67] Cahill, D. G., and Pohl, R. O., 1988, "Lattice Vibrations and Heat Transport in Crystals and Glasses," Annual Review of Physical Chemistry, 39(1), pp. 93-121.

[68] Cahill, D. G., and Pohl, R. O., 1989, "Heat flow and lattice vibrations in glasses," Solid State Communications, 70(10), pp. 927-930.

[69] Hopkins, P. E., and Piekos, E. S., 2009, "Lower limit to phonon thermal conductivity of disordered, layered solids," Applied Physics Letters, 94(18), p. 181901.

[70] E. Hopkins, P., and Beechem, T., 2010, Phonon Scattering and Velocity Considerations in the Minimum Phonon Thermal Conductivity of Layered Solids Above the Plateau.

[71] Lubchenko, V., and Wolynes, P. G., 2003, "The origin of the boson peak and thermal conductivity plateau in low-temperature glasses," Proceedings of the National Academy of Sciences, 100(4), p. 1515.

[72] Lervik, A., Bresme, F., Kjelstrup, S., Bedeaux, D., and Rubi, J., 2010, Heat transfer in protein–water interfaces.

[73] Kjelstrup, S., Miguel Rubi, J., and Bedeaux, D., 2005, "Energy dissipation in slipping biological pumps," Physical Chemistry Chemical Physics, 7(23), pp. 4009-4018.

[74] Helbing, J., Devereux, M., Nienhaus, K., Nienhaus, G. U., Hamm, P., and Meuwly, M., 2012, "Temperature Dependence of the Heat Diffusivity of Proteins," J. Phys. Chem. A, 116(11), pp. 2620-2628.

[75] Botan, V., Backus, E. H. G., Pfister, R., Moretto, A., Crisma, M., Toniolo, C., Nguyen, P. H., Stock, G., and Hamm, P., 2007, "Energy transport in peptide helices," Proceedings of the National Academy of Sciences, 104(31), p. 12749.

[76] Sagnella, D. E., and Straub, J. E., 2001, "Directed Energy “Funneling" Mechanism for Heme Cooling Following Ligand Photolysis or Direct Excitation in Solvated Carbonmonoxy Myoglobin," The Journal of Physical Chemistry B, 105(29), pp. 7057-7063.

[77] A.E. Schoen, P., Michel, B., Curioni, A., and Poulikakos, D., 2009, Hydrogen-bond enhanced thermal energy transport at functionalized, hydrophobic and hydrophilic silica-water interfaces.

[78] Lin, Z., and Rubtsov, I. V., 2012, "Constant-speed vibrational signaling along polyethyleneglycol chain up to 60-Å distance," Proc Natl Acad Sci U S A, 109(5), pp. 1413-1418.

[79] Lobunez, W., 1960, "Book Reviews : The Hydrogen Bond. George C. Pimentel and A. L. McClellan. San Francisco and London, W. H. Freeman and Co., 1960. xii + 475 pages. Price $11.40," Textile Research Journal, 30(12), pp. 1006-1007.

[80] Nick Pace, C., Scholtz, J. M., and Grimsley, G. R., 2014, "Forces stabilizing proteins," FEBS letters, 588(14), pp. 2177-2184.

[81] Ash, E., 1997, A Low-Barrier Hydrogen Bond in the Catalytic Triad of Serine Proteases? Theory Versus Experiment.

[82] Davydov, A. S., 1977, "Solitons and energy transfer along protein molecules," J. Theor. Biol., 66(2), pp. 379-387.

[83] Xiao, X., Wang, M., Tu, J., and Jiao, S., 2019, "The potential application of black and blue phosphorene as cathode materials in rechargeable aluminum batteries: a first-principles study," PCCP, 21(13), pp. 7021-7028.

[84] Liu, J., and Yang, R. G., 2010, "Tuning the thermal conductivity of polymers with mechanical strains," Phys Rev B, 81(17).

[85] Huang, X. P., Liu, G. Q., and Wang, X. W., 2012, "New Secrets of Spider Silk: Exceptionally High Thermal Conductivity and Its Abnormal Change under Stretching," Adv Mater, 24(11), pp. 1482-1486.

[86] Scheller, J., Guhrs, K. H., Grosse, F., and Conrad, U., 2001, "Production of spider silk proteins in tobacco and potato," Nat Biotechnol, 19(6), pp. 573-577.

[87] Lazaris, A., Arcidiacono, S., Huang, Y., Zhou, J. F., Duguay, F., Chretien, N., Welsh, E. A., Soares, J. W., and Karatzas, C. N., 2002, "Spider silk fibers spun from soluble recombinant silk produced in mammalian cells," Science, 295(5554), pp. 472-476.

[88] An, B., Jenkins, J. E., Sampath, S., Holland, G. P., Hinman, M., Yarger, J. L., and Lewis, R., 2012, "Reproducing Natural Spider Silks' Copolymer Behavior in Synthetic Silk Mimics," Biomacromolecules, 13(12), pp. 3938-3948.

[89] Vishwakarma, V., Waghela, C., Wei, Z., Prasher, R., Nagpure, S. C., Li, J., Liu, F., Daniel, C., and Jain, A., 2015, "Heat transfer enhancement in a lithium-ion cell through improved material-level thermal transport," J. Power Sources, 300, pp. 123-131.

[90] Huxtable, S. T., Cahill, D. G., Shenogin, S., Xue, L. P., Ozisik, R., Barone, P., Usrey, M., Strano, M. S., Siddons, G., Shim, M., and Keblinski, P., 2003, "Interfacial heat flow in carbon nanotube suspensions," Nature Materials, 2(11), pp. 731-734.

[91] Kim, H., Abdala, A. A., and Macosko, C. W., 2010, "Graphene/Polymer Nanocomposites," Macromolecules, 43(16), pp. 6515-6530.

[92] Deng, S., Xiao, C., Yuan, J., ma, D., Li, J., Yang, N., and He, H., 2019, Thermal Boundary Resistance Measurement and Analysis Across SiC/SiO2 Interface.

[93] Li, X., Yan, Y., Dong, L., Guo, J., Aiyiti, A., Xu, X., and Li, B., 2017, Thermal conduction across a boron nitride and SiO 2 interface.

[94] Hida, S., Hori, T., Shiga, T., Elliott, J., and Shiomi, J., 2013, "Thermal resistance and phonon scattering at the interface between carbon nanotube and amorphous polyethylene," International Journal of Heat and Mass Transfer, 67, pp. 1024-1029.

[95] Ju, S.-H., and Liang, X.-G., 2013, "Investigation on interfacial thermal resistance and phonon scattering at twist boundary of silicon," Journal of Applied Physics, 113(5), p. 053513.

[96] Jiang, T., Zhang, X., Vishwanath, S., Mu, X., Kanzyuba, V., Sokolov, D. A., Ptasinska, S., Go, D. B., Xing, H. G., and Luo, T., 2016, "Covalent bonding modulated graphene–metal interfacial thermal transport," Nanoscale, 8(21), pp. 10993-11001.

[97] Stankovich, S., Dikin, D. A., Dommett, G. H. B., Kohlhaas, K. M., Zimney, E. J., Stach, E. A., Piner, R. D., Nguyen, S. T., and Ruoff, R. S., 2006, "Graphene-based composite materials," Nature, 442(7100), pp. 282-286.

[98] Wang, G., Shen, X., Wang, B., Yao, J., and Park, J., 2009, "Synthesis and characterisation of hydrophilic and organophilic graphene nanosheets," Carbon, 47(5), pp. 1359-1364.

[99] Teng, C.-C., Ma, C.-C. M., Lu, C.-H., Yang, S.-Y., Lee, S.-H., Hsiao, M.-C., Yen, M.-Y., Chiou, K.-C., and Lee, T.-M., 2011, "Thermal conductivity and structure of non-covalent functionalized graphene/epoxy composites," Carbon, 49(15), pp. 5107-5116.

[100] Wang, M., Hu, N., Zhou, L., and Yan, C., 2015, "Enhanced interfacial thermal transport across graphene–polymer interfaces by grafting polymer chains," Carbon, 85, pp. 414-421.

[101] Wang, Y., Zhan, H. F., Xiang, Y., Yang, C., Wang, C. M., and Zhang, Y. Y., 2015, "Effect of Covalent Functionalization on Thermal Transport across Graphene–Polymer Interfaces," The Journal of Physical Chemistry C, 119(22), pp. 12731-12738.

[102] Medhekar, N. V., Ramasubramaniam, A., Ruoff, R. S., and Shenoy, V. B., 2010, "Hydrogen Bond Networks in Graphene Oxide Composite Paper: Structure and Mechanical Properties," ACS Nano, 4(4), pp. 2300-2306.

[103] Compton, O. C., Cranford, S. W., Putz, K. W., An, Z., Brinson, L. C., Buehler, M. J., and Nguyen, S. T., 2011, "Tuning the Mechanical Properties of Graphene Oxide Paper and Its Associated Polymer Nanocomposites by Controlling Cooperative Intersheet Hydrogen Bonding," ACS Nano, 6(3), pp. 2008-2019.

[104] Beese, A. M., Sarkar, S., Nair, A., Naraghi, M., An, Z., Moravsky, A., Loutfy, R. O., Buehler, M. J., Nguyen, S. T., and Espinosa, H. D., 2013, "Bio-Inspired Carbon Nanotube–Polymer Composite Yarns with Hydrogen Bond-Mediated Lateral Interactions," ACS Nano, 7(4), pp. 3434-3446.

[105] Wust, P., Hildebrandt, B., Sreenivasa, G., Rau, B., Gellermann, J., Riess, H., Felix, R., and Schlag, P. M., 2002, "Hyperthermia in combined treatment of cancer," The Lancet Oncology, 3(8), pp. 487-497.

[106] Moore, A. L., and Shi, L., 2014, "Emerging challenges and materials for thermal management of electronics," Materials Today, 17(4), pp. 163-174.

CHAPTER 2

THERMAL TRANSPORT IN MONOCRYSTALLINE AND POLYCRYSTALLINE LITHIUM COBALT OXIDE

2.1 Abstract

Efficient heat dissipation in batteries is important for the thermal management against thermal runway and chemical instability at elevated temperatures. Nevertheless, thermal transport processes in battery materials have not been well understood especially considering their complicated microstructures. In this study, lattice thermal transport in lithium cobalt oxide ($LiCoO_2$), a popular cathode material for lithium ion batteries, is investigated via molecular dynamics-based approaches and thermal resistance models. The $LiCoO_2$ single-crystal is shown to have thermal conductivities in the order of 100 W m^{-1} K^{-1} with strong anisotropy, temperature dependence, and size effects. By comparison, the polycrystalline $LiCoO_2$ is more isotropic with much lower thermal conductivities. The difference is caused by random grain orientations, thermal resistance of grain boundaries, and size-dependent intra-grain thermal conductivities that are unique to polycrystals. The grain boundary thermal conductance is calculated to be in the range of 7.16 - 25.21 GW m^{-2} K^{-1}. The size effects of intra-grain thermal conductivities are described by two empirical equations. Considering all of these effects, two thermal resistance models are formed to predict the thermal conductivity of polycrystalline $LiCoO_2$. The two models predict consistent thermal conductivity–grain size relationship that agrees well with molecular

He, J., Zhang, L., and Liu, L., 2019, "Thermal transport in monocrystalline and polycrystalline lithium cobalt oxide," Physical Chemistry Chemical Physics, 21(23), pp. 12192-12200.

dynamics simulation results. The insights revealed by this study may facilitate future efforts of battery materials design for improved thermal management.

2.2 Introduction

The Li-ion battery has been widely used in electronic devices, electric vehicles and many other consumer products and engineering systems for energy storage [1]. Among the four essential components of Li-ion batteries (i.e. cathode, anode, electrolyte and electrolyte), the cathode plays a key role in determining the capacity and voltage of batteries, for which lithium cobalt oxide ($LiCoO_2$) has been a popular choice. Despite the many advantages including excellent energy density, power density, stability and the long cycle life [2], $LiCoO_2$ has a drawback of relatively low thermal conductivities, which may potentially cause inefficient heat dissipation leading to thermal runaway and chemical instability at elevated temperatures. Hence, it is of great importance to study thermal transport mechanisms in $LiCoO_2$ to gain more physical insights and to guide materials design for improved thermal properties.

Despite the importance, thermal transport processes in $LiCoO_2$ and other electrode materials are relatively underexplored except a few recent studies [3, 4]. Many electrode materials share a common characteristic in that they have polycrystalline microstructures. $LiCoO_2$ in Li-ion batteries, for example, consist of grains with the size of 10-100 nm according to some experimental work [5, 6]. The repetitive grain boundaries are thermal transport barriers as they scatter energy carriers and adversely affect the thermal conductivity. The grain boundary scattering, together with the randomly oriented grains and the size effect associated with intra-grain thermal conductivities, makes thermal

transport processes in polycrystalline materials fundamentally different from that in their monocrystalline counterparts. As such, heat transfer in polycrystalline materials has attracted much attention with applications to silicon [7-9], diamond [9], argon [10], graphene [11] and metallic films [12]; and grain design has been an effective approach for tuning thermal properties of materials [13]. Several models [14-17] have been developed to quantify and predict thermal conduction in polycrystals considering the effects of grain boundaries and grain sizes. These models allow accurate extrapolative predictions of thermal conductivities for polycrystals of larger grains based on the data of nanocrystalline solids. The scale-bridging models enable the use of molecular dynamics in such studies despite its length scale limitations.

Using two molecular dynamics-based computational techniques and thermal resistance models, this work systematically investigates nanoscale thermal transport processes in $LiCoO_2$ considering its monocrystal and polycrystal forms (insets of **Figure 2.1**a, b). The study of monocrystalline $LiCoO_2$ reveals the anisotropy and temperature dependence of its thermal conductivities with a discussion on the intrinsic size effects. The study of polycrystalline $LiCoO_2$ quantifies how grain size impacts on the thermal conductivity in the nanocrystalline regime. The grain boundary as an important structural component of polycrystalline $LiCoO_2$ is also studied to understand its thermal resistance for different grain orientations. All these results are integrated in two thermal resistance models for verification. Calibrated against molecular dynamics simulation results, both models provide consistent quantitative predictions of the thermal conductivity of polycrystalline $LiCoO_2$ in the full range of grain size variance.

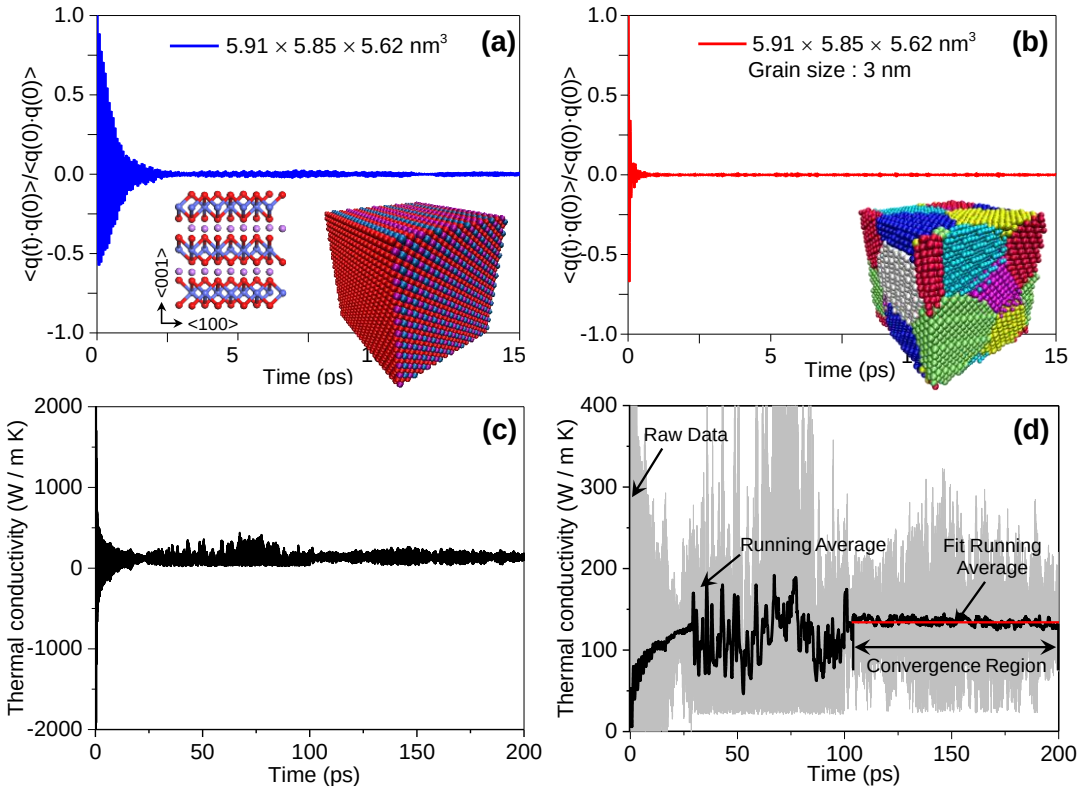

Figure 2.1. Representative normalized HCACF profiles of (a) a monocrystalline $LiCoO_2$ model with the box size of 5.91 × 5.85 × 5.62 nm^3 and (b) a polycrystalline $LiCoO_2$ model with the box size of 5.91 × 5.85 × 5.62 nm^3. Both HCACF profiles are along the *x*-direction or [100] for the monocrystal at 300 K. Only the first 15 ps is shown despite the total correlation time of 0.2 ns. Inset of (a) shows a side view along [010] and a 3D view of the monocrystal model. Inset of (b) shows a 3D view of the polycrystal model. (c) Raw results of the thermal conductivity by integrating the HCACF in (a), which does not converge. (d) Running average of the raw data leads to converging thermal conductivity.

2.3 Models and Methods

2.3.1 3D Voronoi Tessellation

Polycrystalline $LiCoO_2$ models were constructed by using the 3D Voronoi tessellation method [18, 19], which has been widely used for polycrystal modeling. Given a unit cell size for the polycrystal and a target number of grains in the unit cell, grains were randomly generated using the $LiCoO_2$ crystal structure as the structural seed. For instance,

to obtain the polycrystalline $LiCoO_2$ structure with an average grain size of about 3 nm, a simulation box of 5.91 × 5.85 × 5.62 nm^3 was first divided into 8 equal cuboids and a Voronoi point was randomly generated within each of these cuboids. Then, grains boundaries were formed as planes normal to the lines linking neighboring Voronoi points. The polyhedrons bounded by these planar grain boundaries were considered as grains of the polycrystalline material. Each grain was then filled by the $LiCoO_2$ single-crystal structure at random orientations. The polycrystalline model was made fully periodical to make lattice orientation and structure both continuous across all boundaries of the simulation box. Local atomic structures at grain boundaries were further fine-tuned to fix atoms that were too close to each other (with a distance < 0.1 nm) and also to keep charges neutral [10]. The $LiCoO_2$ model formed through these steps can be found in the inset of **Figure 2.1**b.

2.3.2 Molecular Dynamics (MD)

The $LiCoO_2$ ionic crystal was modelled by interatomic interaction along with a core-shell model to obtain reasonable dielectric constants [20, 21]. The interatomic interaction energy for $LiCoO_2$ considers three terms to account for the repulsive, attractive and long-range Coulomb's forces:

$$U_{ij}\left(r_{ij}\right) = A_{ij}\exp\left(-\frac{r_{ij}}{\rho_{ij}}\right) - \frac{C_{ij}}{r_{ij}^6} + \frac{Q_i Q_j}{r_{ij}} \tag{2.1}$$

Here, r_{ij} is the distance between two interacting atoms, Q_i and Q_j are charges on these atoms, and A_{ij}, ρ_{ij} and C_{ij} are parameters of the potential model. The interatomic interaction is complemented by a dipolar core-shell model applied on all cobalt and oxygen ions. Each

of these ions is described by a massless shell with a fractional charge *Y* and an atomic core with the rest of charge *Q*-*Y*. The core and shell are linked by a spring with the spring constant of k_{cs}. The contribution of each core-shell pair to the total energy is described by:

$$E_{cs}(s_i) = \frac{1}{2} k_{cs} s_i^2 \tag{2.2}$$

where s_i denotes the core-shell distance for atom *i*. For atoms represented by the core-shell model, the repulsive and attractive terms of Eq. (2.1) only act on the shells, while the Coulomb's term act on both cores and shells. Note that the Coulomb's interaction between core and shell of the same atom is excluded. Therefore, the total potential energy of the system takes the form of:

$$U_{total} = \sum_{i<j} U_{ij} + \sum_{i \in \mathrm{Co,O}} E_{cs} \tag{2.3}$$

All molecular dynamics simulations were performed using LAMMPS [22] with a time step of 1.0 fs. The short-range terms were truncated at 12 Å. The long-range Coulomb's interaction was calculated by the particle–particle particle-mesh (PPPM) method with a root mean square accuracy of 10^{-6}. Periodic boundary conditions were applied along all directions. Using the force field, MD calculations predict that $LiCoO_2$ has the elastic moduli of 325.03 GPa, 302.09 GPa and 256.86 GPa along the three primary directions, which agree well with DFT calculations [23-25] and experimental data [26].

2.3.3 Equilibrium Molecular Dynamics (EMD)

Based on the fluctuation-dissipation theorem, the Green-Kubo method is an effective MD-based approach to calculate thermal conductivities of bulk materials. According to the Green-Kubo theory, the thermal conductivity tensor is proportional to a

time integral of the heat current autocorrelation function (HCACF). For example, the thermal conductivity along the i-th ($i = x, y, z$) direction can be computed by: [27]

$$\kappa_i = \frac{1}{Vk_B T^2}\int_0^\infty \langle J_i(0) J_i(t)\rangle dt \tag{2.4}$$

where T is the temperature, k_B is the Boltzmann constant, V is the domain volume, $J_i(t)$ is the time-dependent heat current along the i-th direction, and $\langle\cdot\rangle$ represents the ensemble average. The heat flux is given by: [28]

$$\mathbf{J} = \sum_i E_i \mathbf{v}_i + \sum_{i>j} \left[\mathbf{F}_{ij}\cdot\left(\mathbf{v}_i + \mathbf{v}_j\right)\right]\mathbf{r} \tag{2.5}$$

where $\mathbf{v}_i$ is the velocity of atom i, $\mathbf{F}_{ij}$ is the force on atom i exerted by its neighboring atom j, and $\mathbf{r}_{ij}$ is the relative position vector. Here, the total energy associated with the i-th atom, E_i, is expressed by

$$E_i = \frac{1}{2} m_i \mathbf{v}_i^2 + \frac{1}{2}\sum_{i\neq j} U_{ij} \tag{2.6}$$

where m_i is the atomic mass, and U_{ij} is the potential function defined in Eq. (2.1). To prepare a structure for EMD simulation, the system was first equilibrated in NPT at 300 K and 0 atm for 2 ns. The system was then simulated in NVE for 6.5 ns, with the first 2.5 ns to achieve the steady state and the rest 4 ns for thermal conductivity calculations. To calculate thermal conductivities, a long correlation time of 0.2 ns was used in which 20000 samples of the ensemble average were obtained. Each production run of 4 ns contained 20 calculations of the integral of HCACF. Results from these calculations were averaged to reduce uncertainties.

2.3.4 Non-Equilibrium Molecular Dynamics (RNEMD)

RNEMD[29] was used in this study to calculate: (1) interfacial thermal conductance across grain boundaries; and (2) thermal conductivity of a bulk material. The interfacial thermal conductance, *G*, was calculated by

$$G = \frac{J}{\Delta T} \tag{2.7}$$

where *J* is the steady-state heat flux and *T* is the temperature drop across the grain boundary. The thermal conductivity of a bulk material along the heat flux direction (e.g. the *z*-direction) was calculated by

$$\kappa(L) = \frac{J}{dT / dz} \tag{2.8}$$

where dT / dz is the temperature gradient and *J* is the heat flux. The calculated κ is shown as a function of *L*, i.e. model length along the heat flux direction, because NEMD results are known to have prominent length effects [30]. The simulation box was divided into multiple slabs along the heat flux direction. Heat flow was generated by exchanging atomic kinetic energy between the hottest atom in heat sink and the coldest atom in heat source at specified intervals. A virtual elastic collision model was employed to maintain momentum and energy conservation during velocity swapping. At the steady state, heat flux was calculated by

$$J = \frac{\Delta E}{2tA} \tag{2.9}$$

where *A* is the cross-sectional area, ΔE is the average energy exchange per swap, *t* is the time interval between swaps, and the factor of "2" accounts for the two thermal transport paths form heat source to heat sink. To prepare a structure for RNEMD simulation, the

systems were first optimized by conjugate gradient, then equilibrated in NPT at 300 K and 0 atm for 0.5 ns. To relax atomic structures at grain boundaries, relevant systems were heated up in NPT from 300 K to 500 K in 0.5 ns, equilibrated at 500 K and 0 atm for 0.5 ns, cooled down to 300 K in 0.5 ns, and then equilibrated at 300 K and 0 atm for 0.5 ns. Finally, the systems were simulated in NVE for 4 ns. The first 2 ns was to reach the steady state, and the latter 2 ns was the production run.

2.4 Results and Discussion

2.4.1 Heat Current Autocorrelation

Reliable thermal conductivity calculations via EMD require convergence of the system to the steady state, which can be characterized by the normalized heat current autocorrelation function (HCACF). **Figure 2.1**a, b plots the normalized HCACF for two examples of the monocrystalline and polycrystalline $LiCoO_2$, respectively. In both plots, the normalized HCACF decays rapidly within the first couple of picoseconds. The speed of convergence is similar in the other EMD cases performed in this study. Therefore, the correlation time of 0.2 ns is sufficient for accurate thermal conductivity calculations. Compared with the monocrystalline $LiCoO_2$, the polycrystalline $LiCoO_2$ shows faster convergence in the HCACF. This can be explained by the fact that the convergence time of HCACF is proportional to the phonon mean free path or phonon relaxation time.[30] In the polycrystalline structure, phonons are dispersed across grain boundaries making the phonon mean free path restricted by the grain size. This lowers the phonon mean free path leading to faster convergence in the polycrystalline $LiCoO_2$.

An important characteristic of the HCACF of both monocrystalline and polycrystalline $LiCoO_2$ is the unmonotonous decay in the converging regime. Previous EMD studies on other materials have demonstrated two different kinds of decay in the HCACF. Some materials including silicon [9, 31] and argon [10, 32] show monotonous decay in the positive quadrant, while some others including quartz [33] show large oscillations between the positive and the negative as the absolute value decays. The $LiCoO_2$ falls into the second category. The large oscillations during convergence are due to the optical phonons [33] and even after convergence, there exist small oscillations or noises in the HCACF. Such oscillations make direct integration unsuitable for thermal conductivity calculations. Alternatively, McGaughey et al. proposed an approach that uses the running average to calculate thermal conductivities. [33] **Figure 2.1**c plots the thermal conductivity calculated by Eq. (2.4) using the autocorrelation data shown in **Figure 2.1**a. Due to oscillations present in the autocorrelation data, the predicted thermal conductivity does not converge with time. The raw data was then treated by the running average at intervals of 200 fs. **Figure 2.1**d shows the raw data in grey and the treated data in black. Apparently the treated data has much less oscillations with a flat segment indicating convergence. An average in the convergence region gives a more accurate prediction of the thermal conductivity. This approach was applied to all EMD-based thermal conductivity calculations in this study for both monocrystalline and polycrystalline $LiCoO_2$.

2.4.2 Thermal Conductivities of Monocrystalline $LiCoO_2$

This section studies the effects of three parameters (i.e. size, direction and temperature) on the thermal conductivity of monocrystalline $LiCoO_2$. Most of the results

will be generated by EMD, and they will be verified against RNEMD calculations. Thermal conductivities calculated by the Green-Kubo approach are known to have size effects. In small unit cells, phonons of longer wavelengths are prohibited which offsets thermal conductivity predictions. This effect will become insignificant when the unit cell is sufficiently large to include all important phonon modes.

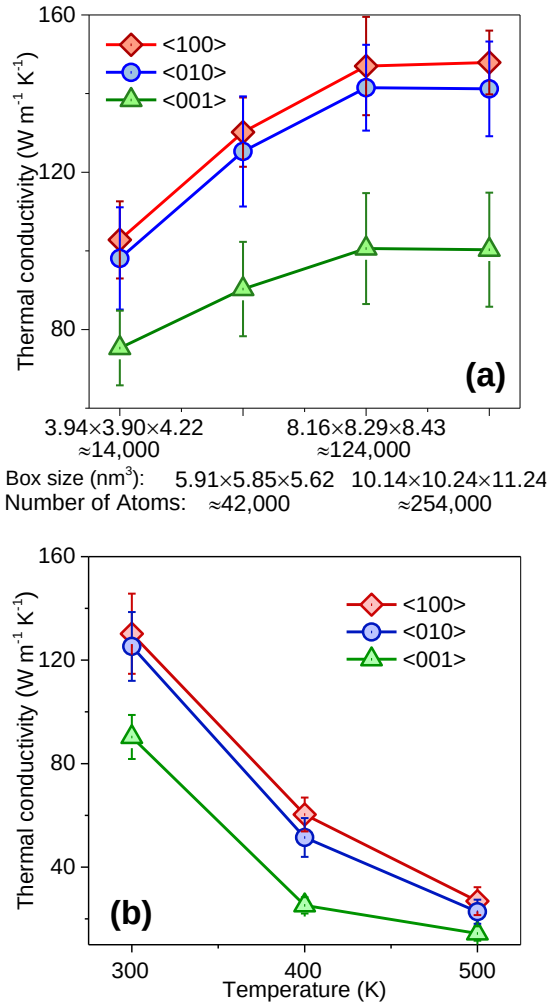

Figure 2.2. (a) Thermal conductivity of monocrystalline $LiCoO_2$ at 300 K along [100], [010] and [001] for four unit structures of increasing sizes. (b) Thermal conductivity of monocrystalline $LiCoO_2$ at different temperatures for the unit structure of 5.91 × 5.85 × 5.62 nm^3. Each data point is an average of the conductivities calculated from 20 independent simulations, with errors bars showing the standard deviation.

To understand this effect, four monocrystalline $LiCoO_2$ models of different sizes were simulated, including 3.94 × 3.90 × 4.22 nm^3, 5.91 × 5.85 × 5.62 nm^3, 8.16 × 8.29 × 8.43 nm^3 and 10.14 × 10.24 × 11.24 nm^3 which correspond to 14 × 8 × 3, 21 × 12 × 4, 29 × 17 × 6 and 36 × 21 × 8 repetitive unit cells in the simulation box. The three axes of the simulation box are aligned with the principle directions of the $LiCoO_2$ crystal, e.g. the *x*-axis along [100]. **Figure 2.2**a plots thermal conductivities of the four $LiCoO_2$ unit structures along all the three primary directions. Each data point is an average of the conductivities calculated from 20 independent simulations, with errors bars showing standard deviation. The thermal conductivity is found to increase with size along all directions with the tendency to converge. The convergence is caused by involvement of more phonon modes in larger simulation structures.

From **Figure 2.2**a, the thermal conductivity converges with the simulation box of 8.16 × 8.29 × 8.43 nm^3 since the calculation with a larger simulation box yields similar results. The converged thermal conductivity, $\boldsymbol{\kappa_0}$, is 147.02 ± 12.5 W m^{-1} K^{-1}, 141.52 ± 10.9 W m^{-1} K^{-1} and 100.62 ± 14.1 W m^{-1} K^{-1} along the three directions of $LiCoO_2$. Using the phonon kinetic theory, the phonon mean free path, λ, can be estimated by

$$\kappa_0 = \frac{1}{3} C v \lambda \tag{2.10}$$

where C is the specific heat and v is the velocity of phonons which can be estimated by the sound velocity in the material.[34] Based on previous experiments,[35] sound velocities of $LiCoO_2$ along the longitudinal and transverse directions are 6961 m/s and 4088 m/s, respectively. An average gives v = 5045.67 m/s. The specific heat was calculated to be C = 70.52 J K^{-1} mol^{-1} at 300 K using the density functional theory [24]. Based on these results

and the mean values of $\boldsymbol{\kappa_0}$, Eq. (2.10) gives the phonon mean free path of 55.11 nm, 53.04 nm and 37.71 nm along the three direction at 300 K.

Based on the results, the thermal conductivity of monocrystalline $LiCoO_2$ is anisotropic with the ranking of [100] > [010] > [001]. This is consistent with the lattice structure of $LiCoO_2$. The $LiCoO_2$ solid is a layered structure composed of monovalent Li^+ layers and anionic Co and O layers alternating along the [001] direction (see inset of **Figure 2.1**a for detail). Phonons experience strong scattering as they transport through the alternating layers in such a "composite" layered structure, which lowers the thermal conductivity along [001]. By comparison, the atomic structure is relatively more consistent within the plane of layers, causing thermal conductivities along the two in-plane directions (i.e. [100] and [010]) comparable with each other and higher than that along [001]. In addition to the anisotropy, thermal conductivities of $LiCoO_2$ are also found to depend on temperature. As shown in **Figure 2.2**b, the thermal conductivity drops by about 60.33% from 300 °C to 400 °C, and decreases further by about 53.31% from 400 °C to 500 °C. In most single crystals, thermal conduction at elevated temperatures is increasingly influenced by the phonon-phonon Umklapp scattering, which lowers the thermal conductivity [36, 37].

The EMD results were further verified by RNEMD for monocrystalline $LiCoO_2$ at 300 K. Due to the setup of RNEMD, it can only calculate the thermal conductivity along one direction at a time, and this verification considers [001]. Another important characteristic of RNEMD is that its results have strong dependency on model length along the direction of interest. One reason is the constraints imposed by the finite model size on

phonons of longer wavelengths, similar to that in EMD. Another reason unique to RNEMD is caused by the varying temperature within the model leading to enhanced phonon scattering. The latter explains why for most materials, RNEMD has much more significant size effects than EMD.

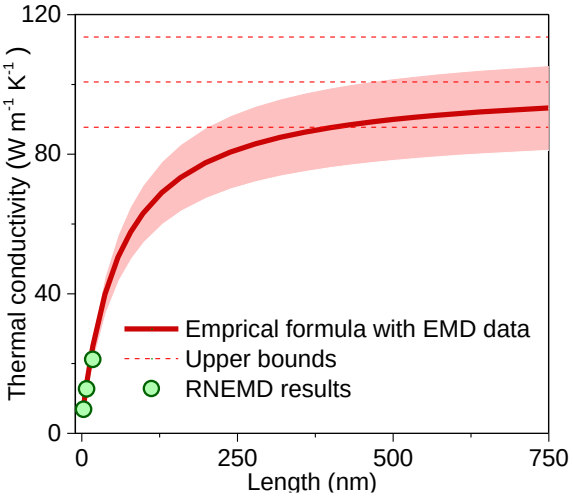

Figure 2.3. Size effects associated with the thermal conductivity of monocrystalline $LiCoO_2$ along the [001] direction. The curve plots the empirical equation Eq. (2.11) using $\boldsymbol{\kappa}_0$ and λ from converged EMD calculations. The shared area is bounded by two similar curves of Eq. (2.11) considering the standard deviation of $\boldsymbol{\kappa}_0$. The three dotted lines are the upper limit of these three curves. Green circles are RNEMD simulation results with different lengths along [001].

Based on many previous studies, the length effect of RNEMD is well characterized by the empirical equation proposed by Schelling *et al.* [30] which takes the form of

$$\frac{1}{\kappa(L)} = \frac{1}{\kappa_0}\left(\frac{\lambda}{L}+1\right) \tag{2.11}$$

where $\boldsymbol{\kappa}$ is the length-dependent thermal conductivity, L is the model length along the direction of interest, $\boldsymbol{\kappa_0} = \boldsymbol{\kappa}_{L\to\infty}$ is the thermal conductivity at the infinite length or when the length effect does not play a role, and λ is the phonon mean free path. The verification

was done by comparing length-dependent RNEMD results with the κ-L relationship predicted by Eq. (2.10) using $\boldsymbol{\kappa_0}$ and λ from the EMD calculations. Quantitatively, along the direction of interest, i.e. [001], EMD gives $\boldsymbol{\kappa_0}$ = 100.62 W m^{-1} K^{-1} and λ = 37.71 nm. With these two numbers, Eq. (2.11) is plotted in **Figure 2.3** which shows excellent agreement with the RNEMD results. Note that the plot of Eq. (2.11) in **Figure 2.3** also considers the uncertainties associated with $\boldsymbol{\kappa_0}$. The thick red line shows the prediction made with the mean value of $\boldsymbol{\kappa_0}$, while the red shaded area shows the variance bounded by predictions made considering the standard deviation of $\boldsymbol{\kappa_0}$. The RNEMD results are shown as green circles for the model length of 9.84 nm, 19.68 nm and 39.35 nm along the [001] direction. In the RNEMD simulation, transverse dimensions along [100] and [010] were set as 3.38 nm and 3.41 nm, respectively, which were large enough to not affect thermal conductivity calculations along [001]. Due to the prominent size effects associated with RNEMD, thermal conductivities predicted with the given lengths are from 6.69 W m^{-1} K^{-1} to 21.01 W m^{-1} K^{-1}, far below $\boldsymbol{\kappa_0}$. However, the agreement shown in **Figure 2.3** suggest excellent consistency between the two approaches.

2.4.3 Grain Boundary Thermal Conductance

RNEMD was employed to study thermal transport across grain boundaries in polycrystalline $LiCoO_2$. A typical simulation model is shown in **Figure 2.4**a which contains two grains. The two grains were assumed to have the same size, *d*, which was varied among 5 nm, 10 nm and 20 nm. One grain was rotated with respect to the other to represent different grain orientations in polycrystals. The rotation can be characterized by two parameters, i.e. the rotation direction and the rotation or tilt angle. This study considers

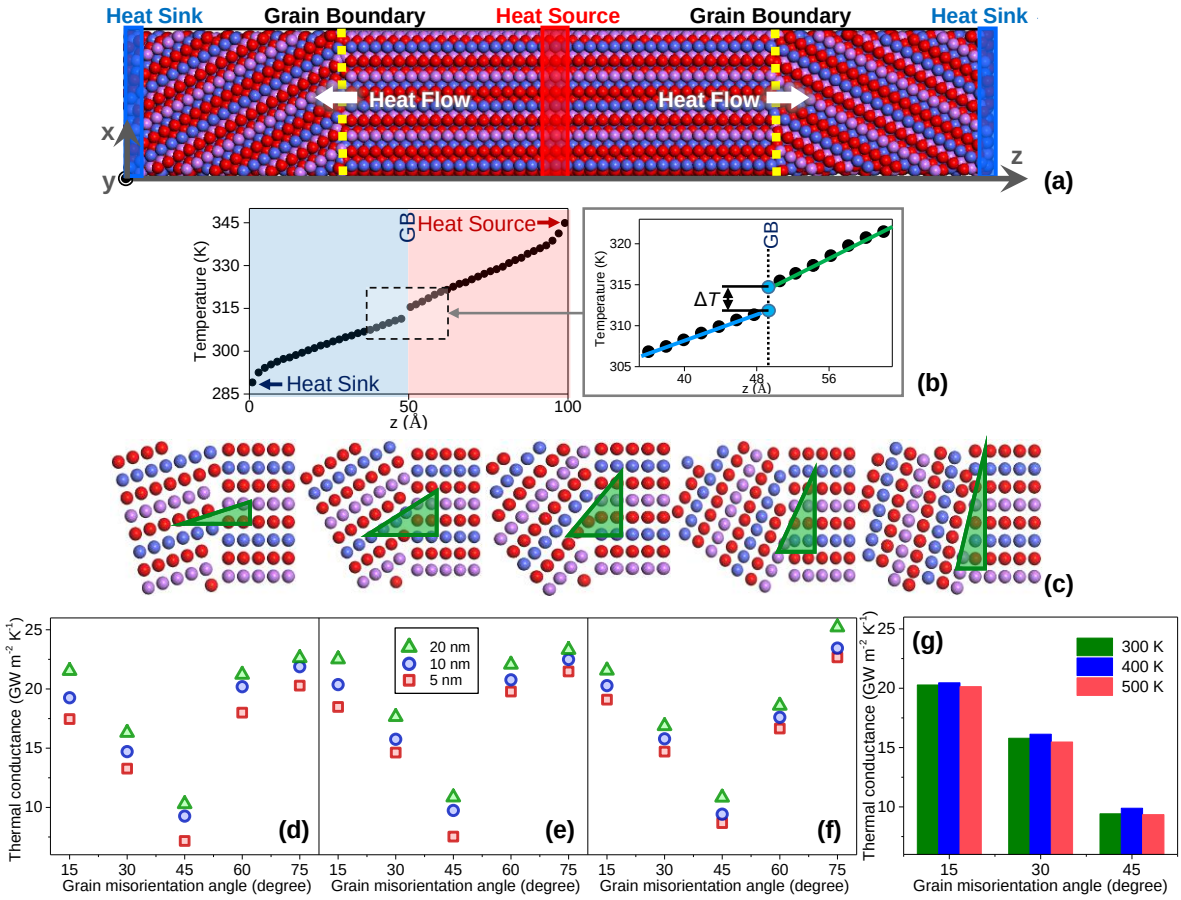

Figure 2.4. (a) A representative model for grain boundary thermal conductance calculations (blue spheres: cobalt; red spheres: oxygen; pink spheres: lithium). (b) Left: temperature profile of the computational system from the RNEMD simulation. Right: A temperature jump is identified across the grain boundary. (c) Five grain boundaries with different tilt angle including 15º, 30º, 45º, 60º and 75º about the *y*-axis. (d) Grain boundary thermal conductance versus the tilt angle and grain size for different tilt orientations about the (d) *x*-axis, (e) *y*-axis and (f) *z*-axis. (g) Effect of temperature on the interfacial thermal conductance for three tilt angles about the *z*-axis.

five tilt angles including 15°, 30°, 45°, 60° and 75° (**Figure 2.4**c) about the three primary axes. For each grain boundary, the RNEMD simulation leads to a temperature profile as illustrated in **Figure 2.4**b. The temperature profile is almost linear in each of the grains except for the nonlinear regions near the heat source and the heat sink. At the grain

boundary, a temperature "jump", ΔT, is identified which is correlated with the grain boundary thermal conductance.

The resulting thermal conductance is plotted in **Figure 2.4**d-f for tilts about the *x*, *y* and *z*-axis, respectively. Interestingly, the tilt direction does not show significant impact on the grain boundary thermal conductance. Instead, the tilt angle plays the most important role. As the tilt angle increases from 0° to 90°, the grain boundary thermal conductance first decreases almost linearly and then increases, attaining its minimum when the tilt angle equals to 45°. Use the data for d = 20 nm as an example. The grain boundary thermal conductance is 21.53 GW $m^{-2} K^{-1}$ when the tilt is at 15° about the *x*-axis, and it drops by 50% to 10.28 GW $m^{-2} K^{-1}$ when the tilt is at 45°. Indeed, among all tilt angles under investigation, 45° leads to the most defects at the grain boundary, and gives the most different lattice structures along the direction of heat current between the two grains. Both factors cause significant phonon scattering and drastically increase thermal resistance. In addition to the tilt angle, the grain size is also found to influence the grain boundary thermal conductance, due to the same reasons that cause the size effects of RNEMD as shown in **Figure 2.4**. Overall, the grain boundary thermal conductance of $LiCoO_2$ is 7.16 ~ 25.21 GW $m^{-2} K^{-1}$ considering all cases investigated in this study.

Further, effect of temperature is explored by using a representative microstructure with the grain size of 10 nm, three selected tile angles about the z-axis including 15°, 30° and 45°, and three temperatures including 300 K, 400 K and 500 K. As shown in **Figure 2.4**g, temperature does not show obvious impact on the interfacial thermal conductance, in agreement with previous theoretical studies [38-40].

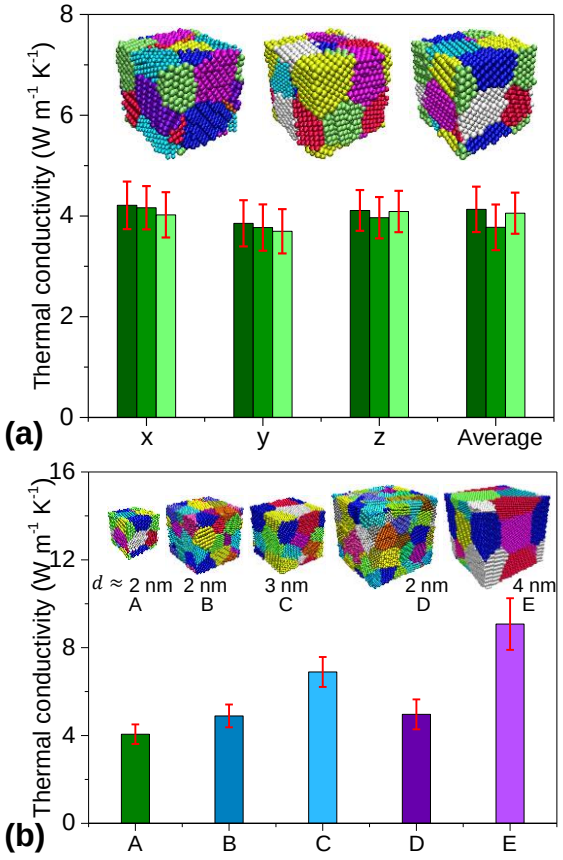

Figure 2.5. (a) Thermal conductivities of three polycrystalline $LiCoO_2$ models at 300 K. All three models shown in the insets have 8 grains randomly generated in a box of 3.94 × 3.90 × 4.22 nm^3. (b) Average thermal conductivity of polycrystalline $LiCoO_2$, $\bar{\kappa}$, for five models of different box sizes and numbers of grains. Insets show the five unit structures. Their grain sizes are 2.01 nm, 1.93 nm, 2.90 nm, 2.07 nm and 4.15 nm, respectively

2.4.4 Thermal Conductivities of Polycrystalline $LiCoO_2$

Thermal conductivities were calculated for polycrystalline $LiCoO_2$ using unit structures randomly generated by 3D Voronoi Tessellation. Due to the randomness in unit structure sampling, it is important to understand how much variation the predicted thermal conductivity has due to the structural randomness. For this purpose, three simulation boxes were generated with the same box size of 3.94 × 3.90 × 4.22 nm^3 and the same number of grains (eight). Their thermal conductivities are shown in **Figure 2.5**a. Although 8 is not a

large number of grains, the predicted thermal conductivities already show some isotropy due to the averaging effects caused by randomly oriented grains. The largest conductivity is only about 8-9% higher than the lowest for the same model. The isotropy is expected to be more apparent when more grains are present in the model. Due to the demonstrated isotropy, thermal conductivity averaged from the three directions, $\bar{\kappa}$, will be considered in following discussion. Importantly, $\bar{\kappa}$ shows very small sample variance as the unit structure changes. For the three unit structures under investigation, $\bar{\kappa}$ is found as 4.06, 3.97 and 3.94 W m^{-1} K^{-1}, respectively, with differences below 3%. The sample variance is also expected to decrease with the number of grains.

Figure 2.5b shows $\bar{\kappa}$ of five representative unit structures of $LiCoO_2$ with different box sizes and grain sizes. Model A has 8 grains in the box of 3.94 × 3.90 × 4.22 nm^3. Model B has 27 grains and model C has 8 grains, both in the box of 5.91 × 5.85 × 5.62 nm^3. Model D has 64 grains and model E has 8 grains, both in the box of 8.16 × 8.29 × 8.43 nm^3. The grain sizes, *d*, of these five unit structures are 2.01 nm, 1.93 nm, 2.90 nm, 2.07 nm and 4.15 nm, respectively. There are two important findings:

(1) Models A, B and D have comparable grain sizes of approximately 2 nm, and their thermal conductivities are 4.06, 4.89 and 4.96 W m^{-1} K^{-1}, respectively. On one hand, these results are very close, suggesting the important role of grain size. On the other hand, the increasing trend matches well with the size effect revealed in **Figure 2.2**a for monocrystalline $LiCoO_2$. Indeed, as the number of grains increases from 8 (A) to 27 (B) and finally to 64 (D), the simulation box size increases. This allows phonons

of longer wavelengths to participate in heat transfer, leading to higher thermal conductivities.

(2) Models A, C and E feature increasing grain sizes, and their thermal conductivities are 4.06, 6.89 and 9.08 W m^{-1} K^{-1}, respectively. The results, again, show the important role of grain size – the larger grain size, the higher thermal conductivity. The grain size effect will be elucidated in the next section using two thermal resistance models.

It deserves mentioning that the grains in any polycrystal have a distribution in size. As the present study mainly focuses on the effect of average grain size on the thermal conductivity of $LiCoO_2$, some studies in the literature have revealed that the grain size distribution also plays a role. In general, polycrystals with fine grains may have higher thermal conductivities when the grain size is more widely distributed; and such an effect is reduced as the average grain size increases. Using polycrystalline h-BN as an example [41], when the average grain size is about 1 nm, the thermal conductivity with non-uniform grains is about 15% higher than that with uniform grains. The difference drops below 1% when the average grain size exceeds 200 nm. Similar trend is expected for other polycrystals including $LiCoO_2$. With fine grains, the grain boundaries dominate in thermal resistance and heat may be conducted along paths that connect larger grains to reduce thermal resistance. The effect is eliminated when the grain size is sufficiently large so that the intra-grain thermal resistance dominates.

2.4.5 Thermal Resistance Models

Polycrystalline and monocrystalline $LiCoO_2$ are shown to have thermal conductivities that are 1-2 orders of magnitude different. The discrepancy is caused by the

many grain boundaries in polycrystals that resist thermal conduction. This section discusses two thermal resistance models that integrate thermal conductivities of the polycrystal and monocrystal along with the thermal conductance of grain boundaries. The purposes are two folds. First, the model involves all results presented in previous sections for the monocrystal, polycrystal and grain boundaries. It will therefore serve as a verification of computational results of this study. Second, the polycrystals considered in the EMD calculations are limited to having nanoscale grains but realistic polycrystalline $LiCoO_2$ usually have larger grains. This issue can be solved by the thermal resistance models as they work for polycrystals of any grain sizes.

Simplifying the polycrystal as a linear set of grains with equal lengths connected with grain boundaries, thermal resistance model [15] gives

$$\frac{d}{\kappa_{poly}} = \frac{d}{\kappa_{grain}} + \frac{1}{G_{gb}} \tag{2.12}$$

where $\boldsymbol{\kappa_{poly}}$ and $\boldsymbol{\kappa_{grain}}$ are thermal conductivities of the polycrystal and the grain, respectively, G_{GB} is the grain boundary thermal conductance, and d is the grain size. It is important to note that $\boldsymbol{\kappa_{grain}}$ is not $\boldsymbol{\kappa_0}$ which is the thermal conductivity of the monocrystal. Due to the finite size of grains, $\boldsymbol{\kappa_{grain}}$ has a size effect which can be approximately described by Eq. (2.11). Due to randomly oriented grains in the polycrystal, $\boldsymbol{\kappa_0}$ in the equation is approximated by $\overline{\boldsymbol{\kappa_0}}$, which is an average of thermal conductivities along the three directions for monocrystalline $LiCoO_2$. Based on the converged values from the EMD simulation, $\overline{\boldsymbol{\kappa_0}}$ = 129.72 W m^{-1} K^{-1}. Similarly, $\boldsymbol{\lambda}$ is approximated by $\bar{\boldsymbol{\lambda}}$ which is 48.62 nm. Use model E in **Figure 2.5** which has 8 grains in a box of 8.16 × 8.29 × 8.43

nm^3 as an example. Eq. (2.11) gives $\boldsymbol{\kappa_{grain}}$ = 10.16 W m^{-1} K^{-1} with L = d = 4.15 nm. Subsequently, Eq. (2.12) gives G_{gb} = 20.43 GW m^{-2} K^{-1} given that the average thermal conductivity of the polycrystal is $\boldsymbol{\kappa_{poly}}$ = 9.08 W m^{-1} K^{-1} based on the EMD results. The result of grain boundary thermal conductance is well within the range of 7.16 ~ 25.21 GW m^{-2} K^{-1} predicted by RNEMD, which verifies the results of this study.

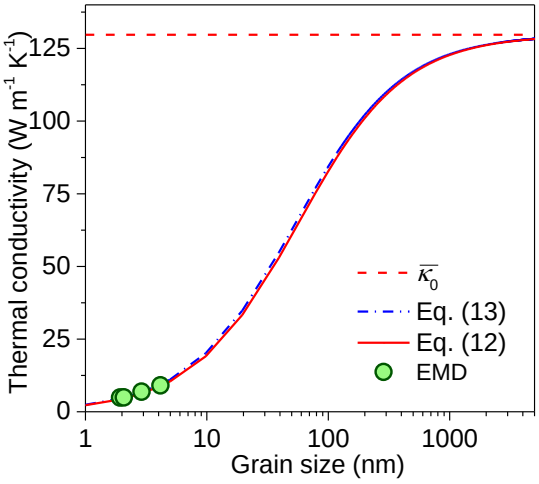

Figure 2.6. Average thermal conductivity, $\bar{\boldsymbol{\kappa}}$, of polycrystalline $LiCoO_2$ versus grain size. The red line plots Eq. (2.12) with the size effects described by Eq. (2.11). The blue dash-dotted line plots Eq. (2.13), which is fitted using the EMD results (green circles). Both models predict the thermal conductivity of polycrystalline $LiCoO_2$ and converge to $\boldsymbol{\bar{\kappa}_0}$, the average thermal conductivity of monocrystalline $LiCoO_2$ (red dashed line).

A more recent model [17] expresses κ_{grain} as $Cv\lambda_{grain}/3$ following Eq. (2.10) and uses the Matthiessen's rule [42] of $\lambda_{grain}^{-1} = \lambda_0^{-1} + \lambda_{gb}^{-1}$ where λ_{grain} and λ_{gb} are phonon mean free path of the grain and the additional phonon mean free path caused by grain boundaries. Assuming λ_{gb} scales with d^{α}, the model takes the form of

$$\kappa_{poly} = \frac{\kappa_0 \Big/ \left(1+\lambda d^{-\alpha}\right)}{1+\kappa_0 \Big/ \left[\left(1+\lambda d^{-\alpha}\right) G_{gb} d\right]} \tag{2.13}$$

where α is a fitting parameter. The fitting is based on EMD results of the thermal conductivity for polycrystals of various grain sizes. For each polycrystal model, $\boldsymbol{\kappa_{poly}}$ is calculated by averaging thermal conductivities along the three directions and d is the corresponding grain size. $\boldsymbol{\kappa_0}$ and $\boldsymbol{\lambda}$ are approximated by $\overline{\boldsymbol{\kappa_0}}$ and $\bar{\boldsymbol{\lambda}}$. G_{gb} is approximated as 16 GW m^{-2} K^{-1}, which is right in the middle of the range calculated by RNEMD. The fitting gives α = 0.9961 for $LiCoO_2$ with a correlation factor of 0.95. The equation with this α is plotted in **Figure 2.6** as the blue dash-dotted line, while the EMD data used for fitting is shown by green circles. As the grain size increases, the predicted $\boldsymbol{\kappa_{poly}}$ approaches $\overline{\boldsymbol{\kappa_0}}$. Similar prediction can also be made by the first model using Eq. (2.12) together with Eq. (2.11) and the same G_{gb} = 16 GW m^{-2} K^{-1}. The resulting $\boldsymbol{\kappa_{poly}}$ is plotted in **Figure 2.6** as the red solid line. Both models give excellent agreement with each other.

A recent experimental work measured the thermal conductivity of polycrystalline $LiCoO_2$ as 5.4 W m^{-1} K^{-1} [26]. The cross-sectional high-resolution transmission electron microscopy (HRTEM) image [26] shows that the average grain size is below 10 nm. Assuming a grain size of 5 nm, our model shown in Eq. (2.13) predicts the thermal conductivity of 10.45 W m^{-1} K^{-1}. The difference is attributable to imperfections present in the sample due to the relatively low annealing temperature of 500 °C [26].

2.5 Conclusions

To summarize, this work uses the MD simulation in combination with thermal resistance models to understand thermal transport in monocrystalline and polycrystalline $LiCoO_2$ and across its grain boundaries. The monocrystalline $LiCoO_2$ shows anisotropic thermal conductivities of 147.02 ± 12.5 W m^{-1} K^{-1}, 141.52 ± 10.9 W m^{-1} K^{-1} and 100.62 ±

14.1 W m^{-1} K^{-1} along the three primary lattice directions, with the lowest along the direction where the lithium layers and the cobalt oxide layers alternate. The thermal conductivities is dependent on temperature, decreasing by about 60.33% from 300 °C to 400 °C and by about 53.31% from 400 °C to 500 °C. Additionally, strong size effects are identified which can be well characterized by Eq. (2.11) indicating a $1/\kappa - 1/L$ correlation. For polycrystalline $LiCoO_2$, the thermal conductivity becomes more isotropic and the dominant factor among others is the grain size. As the grain size varies from 2 nm to 4 nm, the thermal conductivity is increased from about 4.06 W m^{-1} K^{-1} to 9.08 W m^{-1} K^{-1}. The revealed grain size dependence is fundamentally due to two reasons, i.e. size effects of intra-grain thermal conductivities and thermal resistance of grain boundaries. In studying the grain boundary thermal resistance, one of the two grains forming the grain boundary is rotated to sample different relative orientations as seen in realistic grain boundaries. The axis about which the grain is rotated does not show significant influence. Rather, the tilt angle plays a dominant role, making the grain boundary thermal conductance vary in a wide range of 7.16 ~ 25.21 GW m^{-2} K^{-1}. All of these results contribute to the calibration of two thermal resistance models, i.e. Eq. (2.12) and Eq. (2.13). The two models use the same approach to include the contribution made by grain boundaries, but they treat size effects of intra-grain thermal conductivities differently. The first uses the size effects as revealed by Eq. (2.11), while the second uses the phonon kinetic theory with $\lambda_{grain}^{-1} = \lambda_0^{-1} + d^{-\alpha}$. Both models show consistent $\kappa_{poly} - d$ relationship. They collectively provide useful insights into the grain size effect within and beyond the nanocrystalline regime and may contribute to materials design for improved thermal management of batteries.

2.6 Acknowledgment

This work is financially supported by CAREER Award No. CBET-1751610 from the National Science Foundation. The authors would like to thank Dr. Zheyong Fan of Aalto University for fruitful discussion.

REFERENCES

[1] Armand, M., and Tarascon, J. M., 2008, "Building better batteries," Nature, 451, p. 652.

[2] Shao-Horn, Y., Croguennec, L., Delmas, C., Nelson, E. C., and O'Keefe, M. A., 2003, "Atomic resolution of lithium ions in LiCoO2," Nat. Mater., 2, p. 464.

[3] Zhou, Y., Xiong, S., Zhang, X., Volz, S., and Hu, M., 2018, "Thermal transport crossover from crystalline to partial-crystalline partial-liquid state," Nat. Commun., 9(1), p. 4712.

[4] Koo, B., Goli, P., Sumant, A. V., dos Santos Claro, P. C., Rajh, T., Johnson, C. S., Balandin, A. A., and Shevchenko, E. V., 2014, "Toward Lithium Ion Batteries with Enhanced Thermal Conductivity," ACS Nano, 8(7), pp. 7202-7207.

[5] Wu, J., Yang, S., Cai, W., Bi, Z., Shang, G., and Yao, J., 2017, "Multi-characterization of LiCoO2 cathode films using advanced AFM-based techniques with high resolution," Sci. Rep., 7(1), p. 11164.

[6] B. Bates, J., Dudney, N., J. Neudecker, B., X. Hart, F., P. Jun, H., and Hackney, S. A., 2000, Preferred Orientation of Polycrystalline LiCoO2 Films.

[7] Bodapati, A., Schelling, P. K., Phillpot, S. R., and Keblinski, P., 2006, "Vibrations and thermal transport in nanocrystalline silicon," Phys. Rev. B, 74(24), p. 245207.

[8] Bodapati, A., Keblinski, P., Schelling, P. K., and Phillpot, S. R., 2006, "Crossover in thermal transport mechanism in nanocrystalline silicon," Appl. Phys. Lett., 88(14), p. 141908.

[9] Ju, S., and Liang, X., 2012, "Thermal conductivity of nanocrystalline silicon by direct molecular dynamics simulation," J. Appl. Phys., 112(6), p. 064305.

[10] Ju, S., and Liang, X., 2010, "Investigation of argon nanocrystalline thermal conductivity by molecular dynamics simulation," J. Appl. Phys., 108(10), p. 104307.

[11] Mortazavi, B., Pötschke, M., and Cuniberti, G., 2014, "Multiscale modeling of thermal conductivity of polycrystalline graphene sheets," Nanoscale, 6(6), pp. 3344-3352.

[12] Feng, B., Li, Z., and Zhang, X., 2009, "Role of phonon in the thermal and electrical transports in metallic nanofilms," J. Appl. Phys., 105(10), p. 104315.

[13] Meyers, M. A., Mishra, A., and Benson, D. J., 2006, "Mechanical properties of nanocrystalline materials," Prog. Mater Sci., 51(4), pp. 427-556.

[14] Nan, C.-W., and Birringer, R., 1998, "Determining the Kapitza resistance and the thermal conductivity of polycrystals: A simple model," Phys. Rev. B, 57(14), pp. 8264-8268.

[15] Yang, H.-S., Bai, G. R., Thompson, L. J., and Eastman, J. A., 2002, "Interfacial thermal resistance in nanocrystalline yttria-stabilized zirconia," Acta Mater., 50(9), pp. 2309-2317.

[16] Maldovan, M., 2011, "Micro to nano scale thermal energy conduction in semiconductor thin films," J. Appl. Phys., 110(3), p. 034308.

[17] Dong, H., Wen, B., and Melnik, R., 2014, "Relative importance of grain boundaries and size effects in thermal conductivity of nanocrystalline materials," Sci. Rep., 4, p. 7037.

[18] Fritzen, F., Böhlke, T., and Schnack, E., 2009, "Periodic three-dimensional mesh generation for crystalline aggregates based on Voronoi tessellations," Comput. Mech., 43(5), pp. 701-713.

[19] Schiøtz, J., Di Tolla, F. D., and Jacobsen, K. W., 1998, "Softening of nanocrystalline metals at very small grain sizes," Nature, 391, p. 561.

[20] Hart, F. X., and Bates, J. B., 1998, "Lattice model calculation of the strain energy density and other properties of crystalline LiCoO2," J. Appl. Phys., 83(12), pp. 7560-7566.

[21] Lewis, G. V., and Catlow, C. R. A., 1985, "Potential models for ionic oxides," J. Phys. C: Solid State Phys., 18(6), pp. 1149-1161.

[22] Plimpton, S., 1995, "Fast Parallel Algorithms for Short-Range Molecular Dynamics," J. Comput. Phys., 117(1), pp. 1-19.

[23] Qi, Y., Hector, L. G., James, C., and Kim, K. J., 2014, "Lithium Concentration Dependent Elastic Properties of Battery Electrode Materials from First Principles Calculations," Journal of The Electrochemical Society, 161(11), pp. F3010-F3018.

[24] Wu, L., Lee, W. H., and Zhang, J., 2014, "First Principles Study on the Electrochemical, Thermal and Mechanical Properties of LiCoO2 for Thin Film Rechargeable Battery," Mater. Today:. Proc., 1(1), pp. 82-93.

[25] Wu, L., and Zhang, J., 2015, "Ab initio study of anisotropic mechanical properties of LiCoO2 during lithium intercalation and deintercalation process," Journal of Applied Physics, 118(22), p. 225101.

[26] Cho, J., Losego, M. D., Zhang, H. G., Kim, H., Zuo, J., Petrov, I., Cahill, D. G., and Braun, P. V., 2014, "Electrochemically tunable thermal conductivity of lithium cobalt oxide," Nat. Commun., 5, p. 4035.

[27] Green, M. S., 1954, "Markoff Random Processes and the Statistical Mechanics of Time-Dependent Phenomena. II. Irreversible Processes in Fluids," J. Chem. Phys, 22(3), pp. 398-413.

[28] Zwanzig, R., 1965, "Time-Correlation Functions and Transport Coefficients in Statistical Mechanics," Annu. Rev. Phys. Chem., 16(1), pp. 67-102.

[29] Müller-Plathe, F., 1997, "A simple nonequilibrium molecular dynamics method for calculating the thermal conductivity," J. Chem. Phys, 106(14), pp. 6082-6085.

[30] Schelling, P. K., Phillpot, S. R., and Keblinski, P., 2002, "Comparison of atomic-level simulation methods for computing thermal conductivity," Phys. Rev. B, 65(14), p. 144306.

[31] Wang, Z., and Ruan, X., 2017, "On the domain size effect of thermal conductivities from equilibrium and nonequilibrium molecular dynamics simulations," J. Appl. Phys., 121(4), p. 044301.

[32] McGaughey, A. J. H., and Kaviany, M., 2004, "Thermal conductivity decomposition and analysis using molecular dynamics simulations. Part I. Lennard-Jones argon," Int. J. Heat Mass Transfer, 47(8), pp. 1783-1798.

[33] McGaughey, A. J. H., and Kaviany, M., 2004, "Thermal conductivity decomposition and analysis using molecular dynamics simulations: Part II. Complex silica structures," Int. J. Heat Mass Transfer, 47(8), pp. 1799-1816.

[34] Ledbetter, H. M., 1980, "Sound velocities and elastic-constant averaging for polycrystalline copper," J. Phys. D: Appl. Phys., 13(10), pp. 1879-1884.

[35] Cheng, E. J., Taylor, N. J., Wolfenstine, J., and Sakamoto, J., 2017, "Elastic properties of lithium cobalt oxide (LiCoO2)," J. Asian Ceram. Soc., 5(2), pp. 113-117.

[36] Taube, A., Judek, J., Łapińska, A., and Zdrojek, M., 2015, "Temperature-Dependent Thermal Properties of Supported MoS2 Monolayers," ACS Applied Materials & Interfaces, 7(9), pp. 5061-5065.

[37] Langenberg, E., Ferreiro-Vila, E., Leborán, V., Fumega, A. O., Pardo, V., and Rivadulla, F., 2016, "Analysis of the temperature dependence of the thermal conductivity of insulating single crystal oxides," APL Materials, 4(10), p. 104815.

[38] Duda, J. C., Beechem, T. E., Smoyer, J. L., Norris, P. M., and Hopkins, P. E., 2010, "Role of dispersion on phononic thermal boundary conductance," Journal of Applied Physics, 108(7), p. 073515.

[39] Monachon, C., Weber, L., and Dames, C., 2016, "Thermal Boundary Conductance: A Materials Science Perspective," Annual Review of Materials Research, 46(1), pp. 433-463.

[40] Swartz, E. T., and Pohl, R. O., 1989, "Thermal boundary resistance," Reviews of Modern Physics, 61(3), pp. 605-668.

[41] Mortazavi, B., Pereira, L. F. C., Jiang, J.-W., and Rabczuk, T., 2015, "Modelling heat conduction in polycrystalline hexagonal boron-nitride films," Scientific Reports, 5, p. 13228.

[42] Wang, Z., Alaniz, J. E., Jang, W., Garay, J. E., and Dames, C., 2011, "Thermal Conductivity of Nanocrystalline Silicon: Importance of Grain Size and Frequency-Dependent Mean Free Paths," Nano Lett., 11(6), pp. 2206-2213.

CHAPTER 3

IMPROVING THERMAL CONDUCTION ACROSS CATHODE/ELECTROLYTE INTERFACES IN SOLID-STATE LITHIUM-ION BATTERIES BY HIERARCHICAL HYDROGEN BOND NETWORK

3.1 Abstract

Effective thermal management is an important issue to ensure safety and performance of lithium-ion batteries. Fast heat removal is highly desired but has been obstructed by the high thermal resistance across cathode/electrolyte interface. In this study, self-assembled monolayers (SAMs) are used as the vibrational mediator to tune interfacial thermal conductance between an electrode, lithium cobalt oxide (LCO), and a solid state electrolyte, polyethylene oxide (PEO). Embedded at the LCO/PEO interface, SAMs are specially designed to form hierarchical H-bond network with PEO. Molecular dynamics simulations demonstrate that all SAM-decorated interfaces show enhanced thermal conductance and dominated by H-bonds types. The incorporation of poly(acrylic acid) (PAA) SAM drastically enhances interfacial thermal conductance by approximately 211.69%, largely due to the formation of a strong H-bond, -COOH⋯:O, between PAA and PEO. Even with weaker H-bonds such as -OH⋯:O, it still outperforms the pristine interface as well as interfaces decorated with non-H-bonded SAMs, e.g. PE. Such improvement is attributed to the unique hierarchical H-bond network at the interface, which removes discontinuities in temperature field, straighten SAM chains, make

He, J., Zhang, L., and Liu, L., 2020, "Improving thermal conduction across cathode/electrolyte interfaces in solid-state lithium-ion batteries by hierarchical hydrogen bond network," Materials & Design, 194, pp.10892.

materials strongly adhere, and couple the vibrational modes of materials. The study is expected to guide surface engineering for more effective thermal management in lithium-ion batteries.

3.2 Introduction

Solid-state lithium-ion batteries have been widely employed for applications including consumer electronics and electric vehicles for their high energy density, specific capacity and credible life [1, 2]. Many novel materials have been developed in recent years for the cathode, anode and electrolyte of solid-state lithium-ion batteries to achieve high electrochemical performance. Despite the progress, applications and deployment of solid-state lithium-ion batteries are also influenced by other issues such as the thermal management [3]. As batteries are in operation, heat builds up and if not dissipated efficiently, it may cause overheating leading to lower electrochemical performance and even thermal runway [4-8]. To address this issue, several methods have been proposed including overdesigning, less operation and reducing interfacial impedance by thermal treatment to keep the battery temperature below the design limit. While being effective, these approaches inevitably reduce the efficiency or increase the cost of batteries.

An alternative and arguably more fundamental approach is to enhance the intrinsic thermal conductivity of lithium-ion batteries, making heat removal more efficient [9]. Previous studies in lithium-ion batteries have discovered that the actual bottleneck obstructing heat transfer in lithium-ion batteries is the interfaces between the material components [10-12]. Indeed, a recent experiment [13] in lithium-ion batteries has shown that, with thermal resistance of about 840 $\mu K\ m^2\ W^{-1}$, interface contributes over 88% to the

overall thermal resistance of lithium-ion batteries. Hence, it becomes imperative to enhance thermal conduce across materials interfaces to make heat transfer in solid-state lithium-ion batteries more efficient.

Material interfaces are thermally resistant because significant scattering takes place while phonons transport from one material into another. The interfacial phonon scattering has been shown to strongly correlate with the mismatch between the phonon states of two materials as well as the interfacial strength. As such, many approaches have been developed to reduce phonon scattering and improve interfacial heat transfer, including enhancing the interfacial adhesion [14-16], increasing stiffness [17, 18], strengthening interfacial interactions [10, 19], matching phonon modes [20-22] and functionalizing surfaces [23, 24].

This study aims to reduce thermal resistance across the cathode/electrolyte interface by incorporating a hierarchical network of H-bonds enabled by polymeric self-assembled monolayers (SAMs). Organizing molecular assemblies into large ordered domains on surfaces, SAMs have attracted extensive attention due to its wide applications in many fields such as wetting and adhesion [25-27], nanofabrication [28], biocompatibility and molecular recognition [29], nanostructure deposition [30], and interface engineering [31-33]. The interfacial modification represents a unique combination of two novel concepts that have been previously shown to enhance interfacial thermal transport across various materials interfaces: (1) adding a polymeric monolayer between the two materials forming an interface and (2) designing interfaces to carry H-bonds. On one hand, self-assembled monolayer (SAM) has been widely investigated to improve interfacial thermal conduction between metals [20, 21] and across graphene/polymer interfaces [34]. In particular, the interfacial

thermal conductance has been shown to largely depend on the strength of the chemical bonds associated with the SAM [20, 35]. For instance, at the interface between quartz and gold, the SAM with SH-C_{11}-Si≡ increases thermal conductance by 80%, much more than other SAMs with weaker bonds at the interface. On the other hand, incorporating H-bonds has drastically enhanced thermal conduction in several materials systems including crystalline polymer nanofibers [36], protein β-sheets [37, 38], polymer blends [39], graphene/polymer interface [34] and solid/liquid interfaces [35, 40]. The H-bond is a strong secondary chemical bond formed between a hydrogen atom bound to a more electronegative atom or group (H-bond donor) and a nearby atom that serves as the H-bond acceptor. One of its unique advantages is that it has higher strength than the van der Waals interaction [41]. By functionalizing graphene with hydroxyl groups at the graphene/PMMA interface, H-bonds form and enable new thermal transport pathways, leading to a significant increase of 273% for the interfacial thermal conductance.

By combining the unique features of both SAMs and the H-bonding, this work probes the use of H-bonded SAMs for improved interfacial thermal transport across cathode/electrolyte interfaces. The cathode material under investigation is lithium cobalt oxide ($LiCoO_2$ or LCO) [42] and the solid electrolyte material is poly(ethylene oxide) (PEO). Both are widely used in commercial solid-state lithium-ion batteries for portable devices. Molecular dynamics simulation shows that specially designed H-bonded SAMs can enhance the interfacial thermal conductance by over 200%. The level of enhancement depends strongly on the type and density of H-bonds carried by different SAMs. For example, the LCO-PAA/PEO interface which features the primary H-bond of -COOH⋯:O

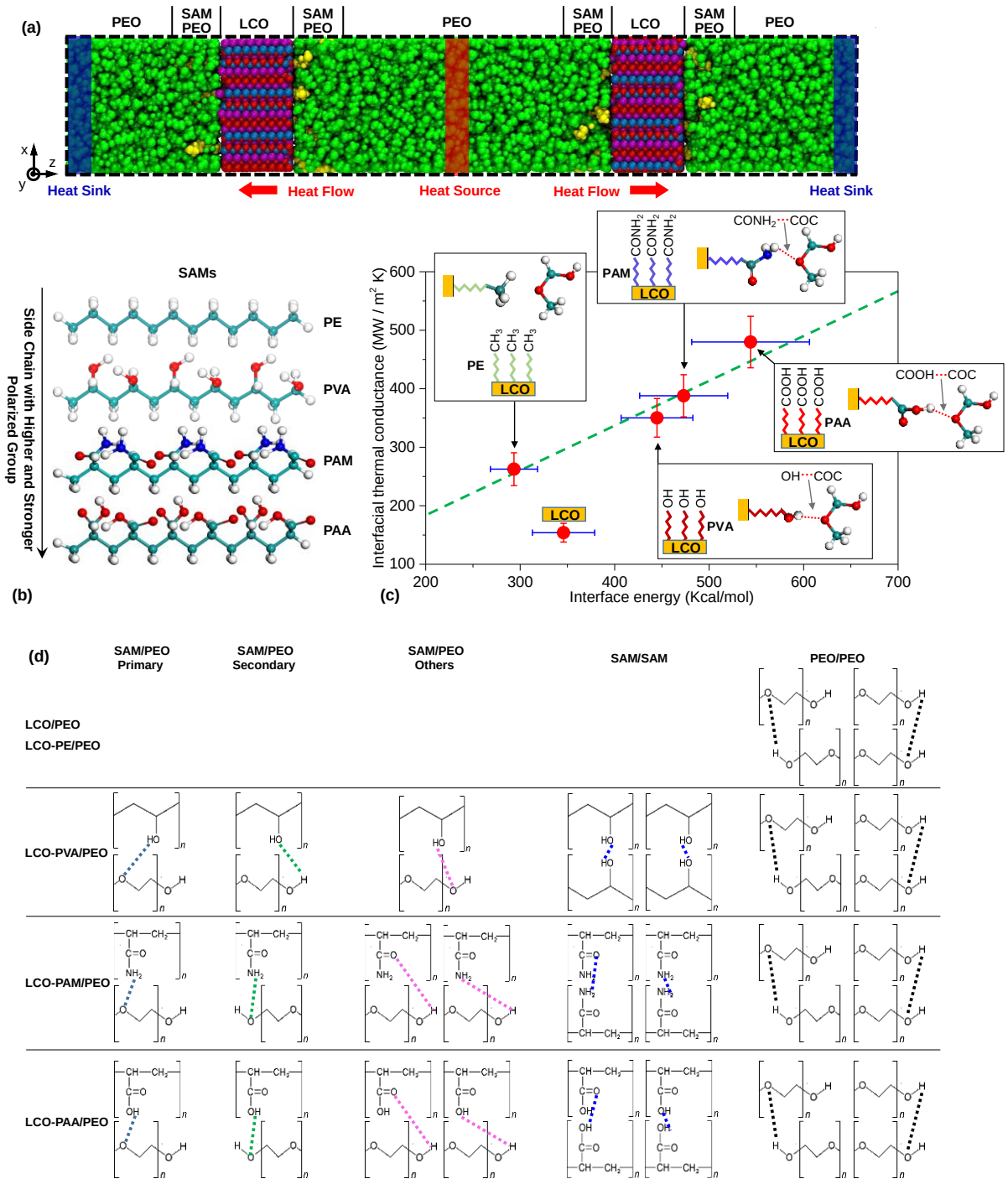

Figure 3.1. (a) A full-atom model for calculating the interfacial thermal conductance between PEO and SAM-decorated LCO by using the reverse non-equilibrium molecular dynamics simulation. (b) Four polymers are considered as the decorative SAM: PE, PVA, PAM and PAA. (c) Interfacial thermal conductance and interfacial energy of adhesion across the pristine and four SAM-decorated LCO/PEO interfaces. Insets show schematics

of the interfaces including the primary H-bond between PEO and the SAM. (d) A summary of all types of H-bonds (dashed lines) that may form in the materials systems under investigation. Rows show different materials systems including LCO/PEO, LCO-PE/PEO, LCO-PVA/PEO, LCO-PAM/PEO, and LCO-PAA/PEO. Columns show different groups of H-bonds in these systems including primary, secondary and other H-bonds between the SAM and PEO, H-bonds within the SAM, and H-bonds within PEO.

drastically enhances the interfacial thermal conductance by 211.69%, while the LCO-PVA/PEO interface which has a different type of primary H-bond, -OH···:O, shows a relatively lower enhancement of 127.36%. Both are higher than the enhancement of 70.57% given by the PE SAM which carries no H-bonding.

3.3 Models and Methods

3.3.1 Cathode/Electrolyte Interface Models

Figure 3.1a shows an atomistic model with four symmetric cathode/electrolyte (LCO/PEO) interfaces. The computational system has a size of 42.161 Å × 34.136 Å × 258.512 Å. Four kinds of polymeric SAMs were used to functionalize the LCO surface including polyethylene (PE, $[C_2H_4]_n$), polyvinyl alcohol (PVA, $[C_2H_4O]_n$), polyacrylamide (PAM, $[C_3H_5NO]_n$) and polyacrylic acid (PAA, $[C_3H_4O_2]_n$), as illustrated in **Figure 3.1**b. The four SAMs have almost the same length for backbone consisting six repeat units, and they have distinct side chains. The PE has $–CH_3$ side chains which do not form H-bonds with PEO. The other three all form H-bonds with PEO, but the formed H-bonds have different numbers and strengths. The primary H-bonds formed at these interfaces are illustrated in the inset images of **Figure 3.1**c. For the LCO-PVA/PEO interface, the primary H-bond forms between the O atom in PEO and the –OH group of PVA. Similar H-bonds form between the $–CONH_2$ group in PAM and the –COOH group in PAA. A

complete description of all H-bonds that may form in these interfaces can be found in **Figure 3.1d**. The initial structure of PEO was generated by the self-avoiding random walk approach with 60 repeat units per chain. Both LCO and SAM polymers were generated by our in-house code. Periodic boundary conditions were applied along all three directions. All material constituents including LCO, PEO and SAMs, were first fully equilibrated before being merged in VMD [43] to generate the LCO/PEO interface model. In each simulation system, the cross section is large enough to eliminate effects of the lateral size on interfacial thermal transport [18, 44-46]. According to two previous studies on the graphene/PMMA interface and the α-Fe_2O_3 crystal, the lateral dimension of 35 Å is sufficient to yield converging thermal conductivity along the length direction which includes the contribution by all dominant phonon modes [44, 46].

3.3.2 Molecular Dynamics

MD simulation was performed using LAMMPS [47]. The LCO ionic crystal was modelled by Buckingham potential [48, 49]. PEO and SAMs were described by the OPLSAA force field [50, 51], which has been widely used to model polymers and their interfaces [52, 53]. The non-bonded interaction between LCO and polymers was modelled by the universal force field (UFF) with potential parameters optimized to effectively characterize interfacial adhesion [54, 55]. Initial molecular configurations were first minimized by conjugate gradient algorithm, and then equilibrated and annealed to eliminate residual stresses with a time step of 1 fs. During annealing, the system was heated up from 300 K to 500 K in 500 ps. The system was then relaxed at 500 K for 500 ps, cooled down to 300 K in 500 ps, and

relaxed again at 300 K for 500 ps. The equilibrated structures were used in the subsequent simulation and analysis.

3.3.3 Interfacial Thermal Conductance

Interfacial thermal conductance was calculated based on the reverse non-equilibrium molecular dynamics (RNEMD) simulation. Using $G = J/\Delta T$, thermal conductance across the LCO/PEO interface can be calculated with the heat flux (J) and interfacial temperature drop (ΔT). The system setup can be found in **Figure 3.1**a and **Figure B.1**a. The model was divided into 126 slabs along the direction of intended heat flow (i.e. the z-direction). The heat flow was generated by swapping the atomic kinematic energy of the coolest atoms in the "heat source" slab (red) and that of the hottest atoms in the "heat sink" slab (blue). Virtual elastic collision model was used to maintain momentum and energy conservation during velocity swapping. At steady state, the heat flux was calculated by $J = \Delta E/(2tA)$, where ΔE is the average energy exchange per swap, t is the time interval between swaps, A is the cross-sectional area, and the coefficient "2" accounts for the two symmetric conduction paths in the system. As shown in **Figure B.1**b, a temperature profile was obtained by evaluating the average temperature of all slabs. From the temperature profile, the temperature drop across the interface (ΔT) was evaluated. J together with ΔT gives G. In addition to giving G, the computational model also gives the thermal conductivity of PEO, which can be calculated by using $K = J/(\mathrm{d}T/\mathrm{d}z)$ where $\mathrm{d}T/\mathrm{d}z$ is the temperature gradient in PEO (found by the red lines in **Figure B.1**a). To verify the RNEMD calculation, G was also calculated by using non-equilibrium molecular dynamics (NEMD). The computational system for NEMD is shown in **Figure B.1**d. Temperature of

the heat source was fixed at 320 K, while temperature of the heat sink was adjusted to make the interface temperature at approximately 300 K for all SAMs. Production runs of the RNEMD and NEMD simulation were 4 ns and 8 ns each with a time step of 1 fs.

3.3.4 Temperature Field and Atomic Number Density

NEMD was also employed to evaluate temperature and density distributions in the simulation box. For the calculation of temperature field, temperature of heat source and heat sink were fixed at 450 K and 250 K, respectively. Each model was first equally divided into 80 × 600 cells within the *y*-*z* plane. Atomic positions and velocities were collected during an interval of 4 ns after the steady state is reached. The temperature associated with all atoms inside a cell was averaged to find the cell temperature. The cell density was evaluated by counting all atoms in a cell. Cells not occupied by any atoms were given a temperature of zero.

3.3.5 Interfacial Energy of Adhesion

The interfacial energy of adhesion (W) was calculated to give its correlation with interfacial thermal conductance for different SAM-decorated interfaces. The calculation uses $W = (E_{LCO-SAM} + E_{PEO} - E_{all})/4$. Here, $E_{LCO-SAM}$ is the energy associated with the two SAM-decorated LCO blocks in the system as shown in **Figure 3.1**a, E_{PEO} is the energy of the three PEO blocks, and E_{all} is the energy of the entire system. All of these energy terms were evaluated based on equilibrium MD simulation at 300 K with a time step of 0.5 fs, based on the full model (**Figure 3.1**a) and partial models. The denominator of 4 accounts for the four interfaces included in the model.

3.3.6 Vibrational Density of States (VDOS)

The VDOS analysis describes the atomic vibrational modes of materials, which can further be used to quantify the vibrational mismatch between two materials forming an interface. The VDOS was obtained by Fourier transform of the velocity autocorrelation function averaged over all atoms. It is defined as a function of frequency in the form of $\mathrm{VDOS}(f) = \int_0^{+\infty} e^{-i2\pi f\tau} C_v(\tau) d\tau$, where f is the frequency and τ is the autocorrelation time. $C_v(\tau)$ is the normalized velocity autocorrelation function defined by $C_v(\tau) = \frac{\langle \vec{v}(\tau)\cdot\vec{v}(0)\rangle}{\langle \vec{v}(0)\cdot\vec{v}(0)\rangle}$ where $\vec{v}(\tau)$ denotes the atomic velocity at the time of τ and $\langle\cdot\rangle$ represents an average over the entire system. To account for statistical randomness, the VDOS was evaluated by averaging twenty simulations that start from different initial velocities. Each simulation runs with a duration of 6.4 ns and a time step of 0.5 fs.

3.3.7 Cumulative Correlation Factor

To quantify the match or correlation between the vibrational modes of two materials forming an interface, a cumulative correlation factor (M) was defined as a function of the cutoff frequency, f_c. As an integration in the frequency domain from 0 to f_c, the cumulative correlation factor describes the vibrational match between two materials up to a specified cutoff frequency of f_c. The equation is $M(f_c) = \frac{\int_0^{f_c} \mathrm{VDOS_A}(f)\cdot\mathrm{VDOS_B}(f)df}{\int_0^{\infty} \mathrm{VDOS_A}(f)df \cdot \int_0^{\infty} \mathrm{VDOS_B}(f)df}$, where $\mathrm{VDOS_A}(f)$ and $\mathrm{VDOS_B}(f)$ are VDOS of the two materials, respectively. A lower M value indicates a lower match or a higher mismatch in the vibrational modes up to the frequency of f_c. When the cutoff frequency is greater or

equal to the maximum frequency of all vibrational modes, the M factor is the same as the widely used correlation factor [56].

3.4 Results and Discussions

3.4.1 Validation

The pristine LCO/PEO interface was simulated to validate MD calculations against experimental and computational results from literatures. First, the mass density of PEO was found to be about 1.18 g cm^{-3} at equilibrium, well within the range of 1.13-1.21 g cm^{-3} from the polymer database [57]. Secondly, the thermal conductivity of PEO was calculated to be 0.332 ± 0.015 W m^{-1} K^{-1}, which agrees well with the experimental results ranging from 0.20 to 0.37 W m^{-1} K^{-1} [58]. Thirdly, the thermal conductivity of LCO was calculated to be about 21.25 W m^{-1} K^{-1}, in good agreement with our previous EMD simulation results [59]. Lastly, thermal conductance across the pristine LCO/PEO interface calculated by the RNEMD method was found almost the same as that obtained by the NEMD method, with a minor difference of 8.45%.

3.4.2 H-Bond Dependent Interfacial Thermal Conductance

Figure 3.1c (vertical axis) plots the interfacial thermal conductance computed for various LCO/PEO interfaces, with error bars showing the standard deviation. Corresponding temperature profiles can be found in **Figure B.2**. The pristine LCO/PEO interface is shown to have an interfacial thermal conductance of 153.95 MW m^{-2} K^{-1}, lower than any SAM-functionalized interfaces. Among the four interfaces with SAMs, interfacial heat transfer is enhanced more by incorporating SAM molecules with stronger polarization.

Ranking from the highest enhancement to the lowest is PAA, PAM, PVA and PE. Compared with the pristine interface, interfaces with these SAMs show interfacial thermal conductance enhanced by 211.69%, 151.99%, 127.36%, and 70.57%, respectively (i.e. from 153.95 MW m^{-2} K^{-1} to 479.84, 387.94, 350.02 and 262.59 MW m^{-2} K^{-1}). Note that the PE SAM does not form any H-bonds with PEO. The enhancement of 70.57% is solely due to the penetration of PE chains into the matrix, forming a thicker interface layer that bridges the distinct vibrational modes of LCO and PEO [34]. By comparison, the PAA, PAM and PVA SAMs all form hierarchical H-bond network at the interface as illustrated in **Figure 3.1**a. Carried by SAMs that penetrate into the PEO, the massive number of H-bonds drastically enhances the structural integrity of the interface, leading to enhanced thermal conductance.

3.4.3 Temperature Field

The interfacial decoration with SAMs alleviates spatial discontinuities in the temperature field, thereby improving interfacial heat transfer. **Figure 3.2** plots the full temperature field computed for systems without and with different SAMs, where the same temperature difference is applied between the heat source and the heat sink. The pristine LCO/PEO system shows an obvious discontinuity (black ribbons in **Figure 3.2**a) at the interface where no atoms exist due to the steric repulsion. By comparison, the discontinuity is partially removed in systems with SAMs. As shown in **Figure 3.2**b-e, the black ribbons are relatively thinner and broken into pieces at the sites where SAMs exist. The partial removal of discontinuity implies that the incorporation of SAMs leads to new thermal transport pathways at the interface for more efficient heat transfer.

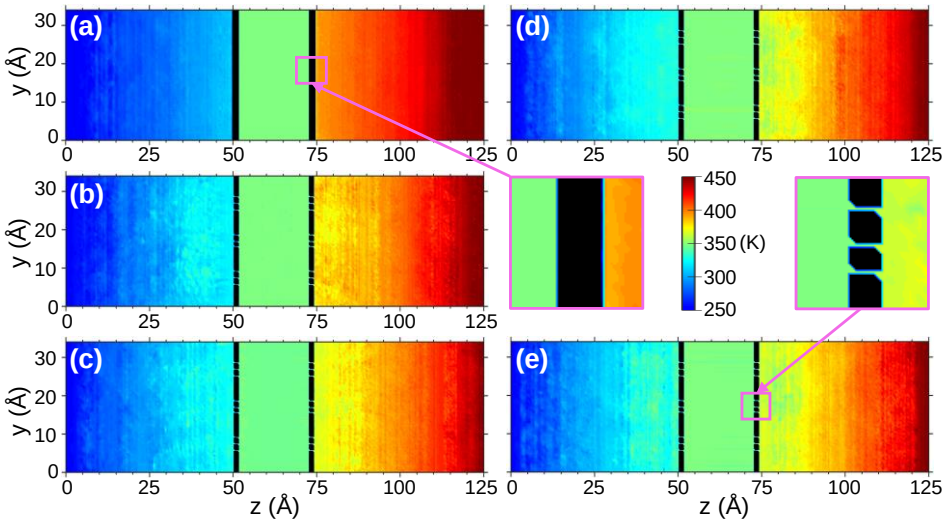

Figure 3.2. Temperature contours of five simulation systems: (a) LCO/PEO, (b) LCO-PE/PEO, (c) LCO-PVA/PEO, (d) LCO-PAM/PEO and (e) LCO-PAA/PEO. The black belts are areas of effectively zero temperature as they are not occupied by atoms.

Moreover, SAMs also blend with PEO to form thick interfaces with high thermal conductivities. **Figure B.3** shows line plots of the temperature profiles for systems under investigation. Overall, the pristine LCO/PEO interface shows a higher temperature drop than the other systems with SAMs, indicating inefficient interfacial heat transfer, echoing the results shown in **Figure 3.1**c. More importantly, in **Figure B.3**, the SAM/PEO blending region is shown to have lower temperature gradients and therefore higher thermal conductivities than the region with PEO only. Despite the fact that PEO has similar thermal conductivities as the polymers used as SAMs in this study, two reasons make the blending region have higher thermal conductivities. On the one hand, H-bonds form between PEO and the SAMs including PVA, PAM and PAA. Similar to a previous study [60], H-bonds form thermal bridges between polymer chains and improve heat transfer in the polymer blends. On the other hand, the SAMs are relatively extended in the blending region. Studies

have shown that extended polymer chains have drastically improved thermal conductivities along the chain direction than their amorphous counterparts [39, 61]. As a result of both reasons combined, heat is conducted more efficiently in the blending region.

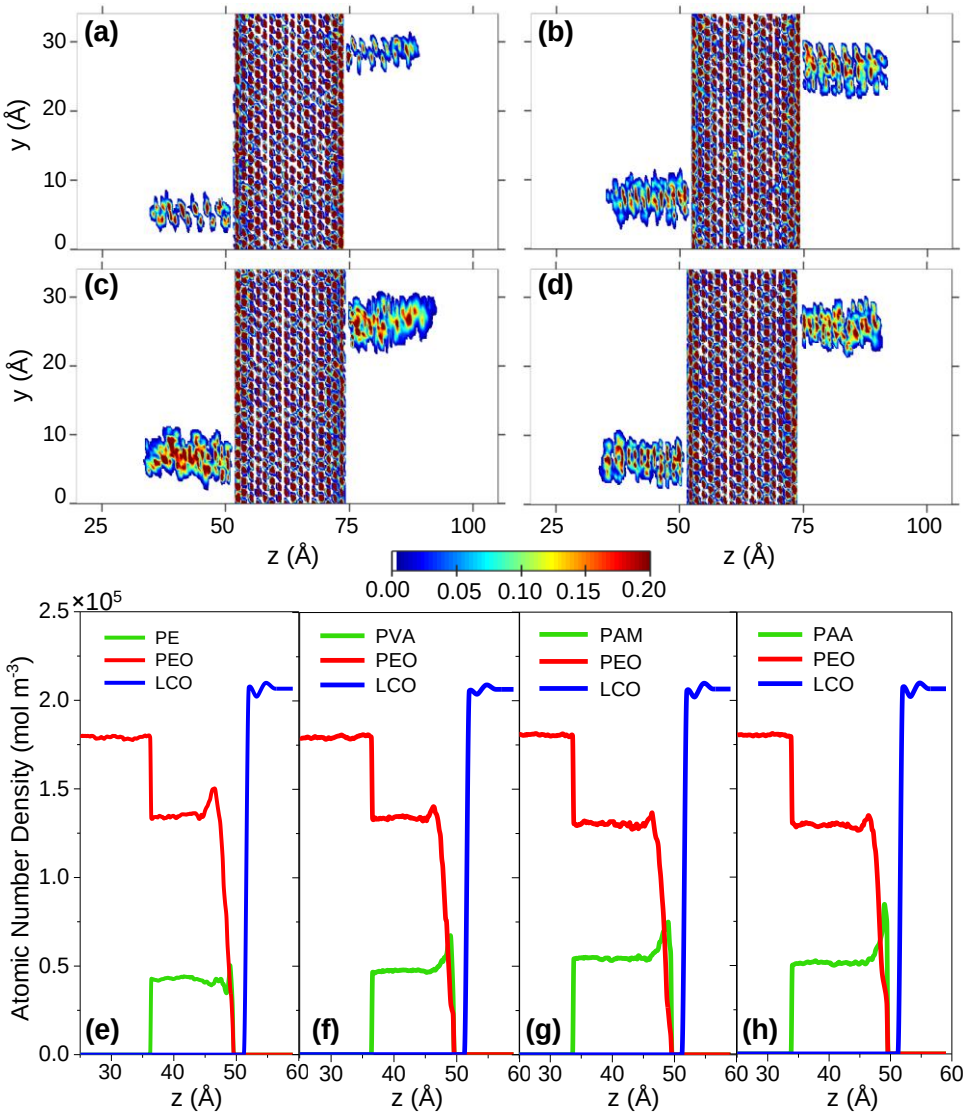

Figure 3.3. Atomic number density distributions of LCO and SAMs for (a) LCO-PE/PEO, (b) LCO-PVA/PEO, (c) LCO-PAM/PEO and (d) LCO-PAA/PEO. One polymer chain is selected at each side of an interface as the representative. (e-h) Line plots of the atomic number density for the four systems.

3.4.4 Stand-up Chain Morphology and Atomic Distribution

To verify that SAMs stand up in the blending zone, **Figure 3.3**a-d plots the atomic number density distributions associated with LCO and the SAMs. One SAM chain is selected on each side of the LCO block. In contact with polymers, LCO shows slightly irregular density distribution at the left and right edges, mostly due to the surface energy. The functional SAMs including PE, PVA, PAM and PAA show stand-up configurations. The configuration is in part due to the steric repulsion between the SAM chains which forces the chains to be relatively straight. Moreover, H-bonds formed with the surrounding PEO further reinforce such configurations so that larger chain surfaces can be exposed to PEO for more H-bonds and lower system energy. The extended chain morphology of SAMs facilitates interfacial thermal conduction as it forces heat to be conducted along chain where thermal conduction is effective. Finally, the functional polymer chains show different widths due to their distinct side chains.

To further understand atomic distributions at the interface, **Figure 3.3**e-h plots the atomic number density profiles of LCO, SAM and PEO for the four systems with SAMs, respectively. The irregular surface density distribution identified for LCO in **Figure 3.3**a-d is shown more clearly here as two peaks near the interface. Due to the high stiffness of LCO, the peaks of LCO (blue lines) which are caused interfacial forces are shown to be very close for the four systems. By comparison, much more significant differences are found in the peaks of SAMs (green lines). PAA shows the highest peak density, followed by PAM, PVA, and PE. Within about 5 Å from the peak, the SAM density drops and reaches a plateau in all four systems. The difference in peak density of SAMs is in part due

to the different average densities of these polymers with distinct side chains. It is also in part attributable to the different interactions between the SAMs and LCO. Finally, the different peaks in SAMs also disturb the distribution of PEO (red lines) in the SAM/PEO blending region, especially near LCO. Outside of the blending region, interfacial effects are minimal and the four systems show almost the same density for PEO.

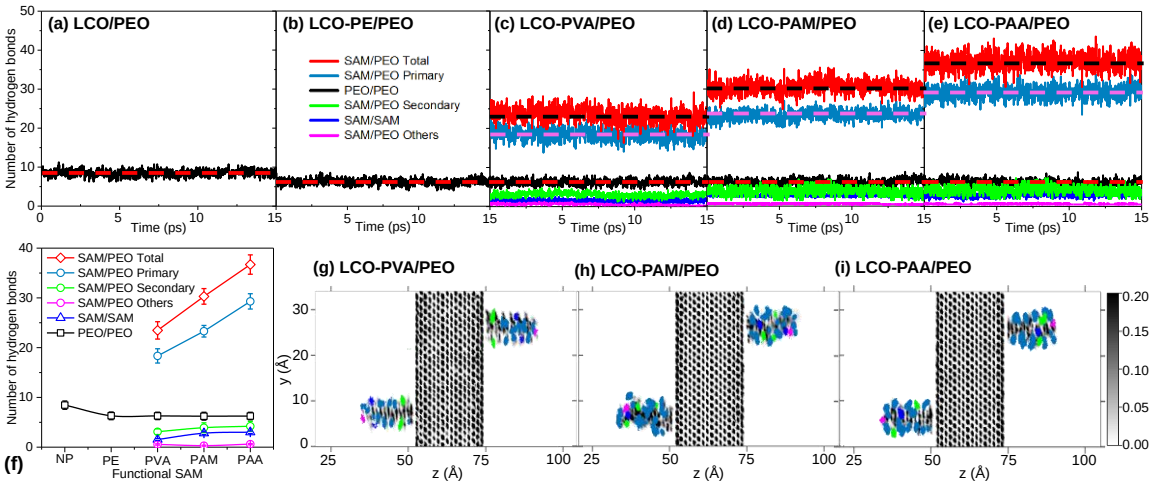

Figure 3.4. Number of H-bonds versus time for (a) LCO/PEO, (b) LCO-PE/PEO, (c) LCO-PVA/PEO, (d) LCO-PAM/PEO and (e) LCO-PAA/PEO. H-bonds of different types are separately shown in the plots. Dashed lines indicate the averages. (f) Summary of the average number of H-bonds for the five systems. (g-i) Cloud maps of H-bond distributions. The grey cloud serves as the background showing the atomic distributions of LCO and SAMs. The colored clouds are H-bond distributions. Each dot in the cloud represents a H-bond forming in the position at a time instant. Colors match that used in (f): primary (steel blue), secondary (green) and other (pink) H-bonds between SAM and PEO; and H-bonds within or between SAM chains (blue).

3.4.5 Hierarchical Hydrogen Bonding Network

As discussed above, the unique H-bond network enabled by SAMs partly removes discontinuity in the temperature field and straightens functional polymer chains, both enhancing interfacial heat transfer. Despite sharing the same enhancement mechanism, the three SAM-functionalized interfaces with H-bonds show different levels of enhancement

varying from 127.36% to 211.69% compared with the pristine LCO/PEO interface (**Figure 3.1**c). Due to the crucial role of H-bonds, the different enhancement must be related with the H-bonds formed at the interface. To better understand H-bond formation, **Figure 3.4**a-e plots the number of H-bonds versus time in all five systems at the steady state. A widely used geometric criterion is used to identify the H-bond. As shown in **Figure B.4**, a H-bond is established if: (1) the distance between the H-bond donor (D) and acceptor (A) is not longer than 3.0 Å; and (2) the angle between H-donor and H-acceptor is not larger than 20˚. Note that neither the pristine LCO/PEO system nor the LCO-PE/PEO system gives zero H-bonds in the plot, because PEO chains by themselves can form H-bonds (**Figure 3.1d**). Between the two systems, the pristine LCO/PEO has more H-bonds (8.45 ± 0.83 versus 6.30 ± 0.77) because more PEO is available in the system due to the lack of SAMs.

In the other three systems that have interfacial H-bonds (**Figure 3.4**c-e), PAA gives the most H-bonds at the interface, followed by PAM and then PVA. The number of H-bonds formed within PEO is almost the same comparing the three systems. Note that all of these systems form multiple kinds of H-bonds. For example, the LCO-PAA/PEO system has -COOH⋯:O as the primary H-bond among the others including: (1) three other kinds formed between PAA and PEO, (2) two kinds formed within PAA, and (3) two kinds formed within PEO (see **Figure 3.1**d for a complete list). The LCO-PAM/PEO system has –$CONH_2$⋯:O as the primary H-bond and seven others. The LCO-PVA/PEO interface has -OH⋯:O as the primary H-bond and six others. As shown in **Figure 3.4**f, the primary H-bond accounts for about 80% of the total number of H-bonds formed at the interface.

To further illustrate how H-bonds form hierarchically in the extended chains of SAMs, **Figure 3.4**g-i depicts H-bond distributions over 16,000 frames of MD simulation for each of the systems. With reference to **Figure 3.4**f, four colors are used to show the primary (steel blue), secondary (green) and other (pink) H-bonds formed between SAM and PEO, and the H-bonds formed within SAM (royal blue), respectively. The H-bonds within PEO are not included as they do not participate in interfacial heat transfer directly. In all cases, H-bonds are well distributed along the SAM chains. The extended chain configuration allows larger exposure of SAM chains to PEO, leading to more H-bonds and making the SAM structure energetically more favorable. Between SAM and PEO, the primary H-bonds dominate with some secondary and other H-bonds scattered in between. In addition, H-bonds also form between neighboring SAM chains, although neighboring SAM chains have an average distance of 13.8 Å in the present setup. The unique H-bond structure displayed in these plots along with the steric repulsion makes the SAM chains highly extended.

3.4.6 Interfacial Energy of Adhesion

Previous studies in interfacial heat transfer have revealed a strong correlation between interfacial thermal conductance and interfacial energy of adhesion for a wide range of materials [15, 62-64], with some exceptions [35]. To better understand the correlation for LCO/PEO interfaces, **Figure 3.1**c plots the interfacial energy of adhesion in conjunction with the interfacial thermal conductance. The two quantities are found to be highly correlated for the four SAM-functionalized interfaces, showing an almost linear relationship (green dashed line in **Figure 3.1**c). However, the pristine LCO/PEO interface

is found to be an exception. Its adhesion energy is 17.89% higher than that of the PE-functionalized interface, while its interfacial thermal conductance is 41.37% lower. The result underlines the importance of structural similarity for the correlation rule to apply. Different from the interfaces with SAMs penetrating into the matrix, the pristine LCO/PEO interface features a bare flat interface leading to fundamentally different thermal transport mechanisms. The correlation rule breaks down as the thermal transport mechanism changes.

The H-bond plays a fundamental role in determining the interfacial energy of adhesion in the systems under investigation. Among the four interfaces with SAMs, the LCO-PE/PEO interface which has no H-bonds has the lowest energy of adhesion of 293.40 kcal/mol and the lowest interfacial thermal conductance of 262.59 MW m^{-2} K^{-1}. With hierarchical H-bonds, the LCO-PAA/PEO interface shows the highest energy of adhesion of 543.89 kcal/mol and the highest interfacial thermal conductance of 479.85 MW m^{-2} K^{-1}. From a chemistry point of view, the COOH···:O H-bond has a strength of 8.92 kcal/mol, followed by CONH···:O (7.40 kcal/mol) and OH···:O (5.0 kcal/mol). The higher bonding energy leads to a higher probability of forming a chemical bond. Hence, the LCO-PAA/PEO system, which has COOH···:O as the primary H-bond, shows the most H-bonds formed at the interface (**Figure 3.4**). The larger number of H-bonds and the higher bonding strength per H-bond collectively cause the higher energy of adhesion at the PAA-decorated interface. The PAM and PVA-decorated interfaces have lower interfacial energy of adhesion and accordingly, lower interfacial thermal conductance.

3.4.7 Vibrational Spectra Coupling

SAM polymers enhance interfacial heat transfer as a vibrational mediator that modulate the vibrational coupling between LCO and PEO. According to the acoustic mismatch model and the diffusive mismatch model [46], interfacial thermal conductance is strongly correlated with the vibrational spectra coupling between two materials forming an interface [39, 65]. The interfacial thermal conductance is usually higher when the two materials match more in their vibration modes [66]. **Figure 3.5**a-e plots the VDOS of all components forming the five interfaces under investigation.

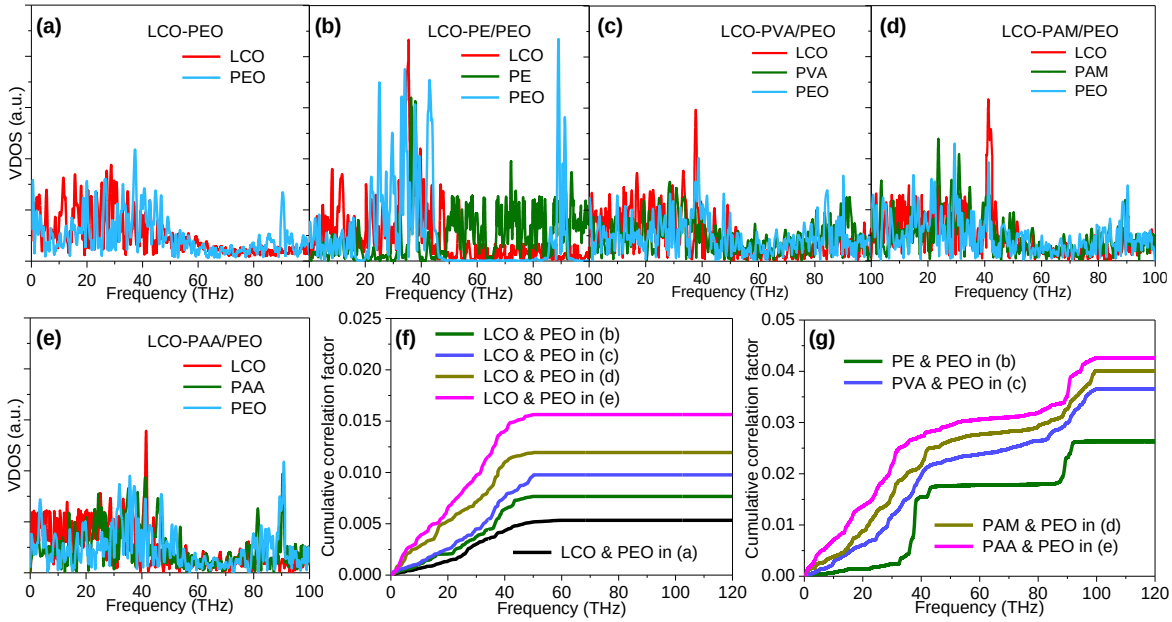

Figure 3.5. Vibrational density of states (VDOS) of different components in (a) LCO/PEO, (b) LCO-PE/PEO, (c) LCO-PVA/PEO, (d) LCO-PAM/PEO and (e) LCO-PAA/PEO. (f) The cumulative correlation factor between LCO and PEO in the five systems. (g) The cumulative correlation factor between SAM and PEO in the four SAM-decorated systems.

Without SAM decoration, the pristine LCO/PEO interface shows poor vibrational coupling as shown in **Figure 3.5**f, which plots a LCO-PEO cumulative correlation factor.

The poor coupling echoes the mismatch demonstrated in **Figure 3.5**a, where PEO shows peaks around 37.45 THz and 90.67 THz while LCO shows peaks from 0 to 33 THz. By incorporating SAMs, vibrational match at the interface is drastically improved (**Figure 3.5**b-e). For example, at the LCO-PAA/PEO interface (**Figure 3.5**e), overlap of major peaks are identified at 41.36 and 90.97 THz. The improved vibrational match with SAMs is also evidenced in **Figure 3.5**f, where SAM-decorated interfaces all show higher correlation than the pristine interface and the LCO-PAA/PEO interface with a strong H-bond network gives the highest interfacial correlation. Similar ranking are also found in the coupling between SAMs and PEO as plotted in **Figure 3.5**g.

Interestingly, we note that even the same pair of materials, i.e. LCO and PEO, show different vibrational correlation factors in the presence of different SAMs (**Figure 3.5**f). Vibrational energy transport is in essence wave transport underpinned by atomic vibrations. The process is highly sensitive to many factors. Materials composition is one of the most important factors, but structural and chemical environment is also critical. In this study, all systems under investigation have LCO and PEO in full or partial contact, where SAMs constitute the environment that influences materials behavior. With different SAMs, different types of H-bonds form in the systems and they influence wave transport and atomic vibrations. This is how the influence of SAMs on LCO/PEO correlation occurs.

3.5 Conclusions

Dictated by molecular design, the interface between LCO and PEO exhibits drastically different thermal conductance which has strong implications for heat removal and thermal management. H-bonded interfaces including LCO-PAA/PEO, LCO-

PAM/PEO and LEO-PVA/PEO show enhancement of 211.69%, 151.99% and 127.36%, respectively, over the pristine interface. By comparison, LCO-PE/PEO which is a non-H-bonded interface enhances thermal conduction by 70.57% only. Apparently, the unique hierarchical H-bond network carried by SAMs is a primary contributor to the significantly enhanced interfacial thermal conduction. The contribution strongly depends on the type, location and density of H-bonds. As revealed in the plot of H-bond clouds, multiple types of H-bonds coexist in each of the systems under investigation. The primary H-bond, which usually accounts for about 80% of all H-bonds at the interface, largely determines the interfacial energy of adhesion and interfacial thermal conductance. For example, the LCO-PAA/PEO interface which features a strong primary H-bond, -COOH⋯:O, has the interfacial thermal conductance 211.69% and the interfacial energy 57.24% more than the pristine interface. The two physical quantities show a linear relationship for the four SAM-decorated interfaces, while the pristine interface which has fundamentally different thermal transport mechanisms disobeys the rule. All SAM-decorated interfaces are shown to have: (1) alleviated discontinuities in the temperature field, (2) stand-up configurations with extended chains, and (3) enhanced coupling of vibrational modes. They synergistically improve interfacial thermal transport, in which H-bonds play a positive role. The H-bond-governed interfacial thermal transport has been previously shown to depend on the density of SAMs [34, 60], and is envisioned to be influenced by the length of SAMs as well which will be a topic of future investigation. The results are expected to improve fundamental understanding and applications of H-bonded interface engineering for improved thermal management of multi-material systems including the lithium-ion batteries.

3.6 Acknowledgments

This work is financially supported by CAREER Award No. CBET-1751610 from the National Science Foundation. The authors would like to thank Dr. Zheyong Fan of Aalto University for fruitful discussion. This research made use of the resources of the High Performance Computing Center at Idaho National Laboratory, which is supported by the Office of Nuclear Energy of the U.S. Department of Energy and the Nuclear Science User Facilities under Contract No. DE-AC07-05ID14517

REFERENCES

[1] Bates, J. B., Dudney, N. J., Neudecker, B., Ueda, A., and Evans, C. D., 2000, "Thin-film lithium and lithium-ion batteries," Solid State Ionics, 135(1), pp. 33-45.

[2] Wang, H., Cao, X., Liu, W., and Sun, X., 2019, "Research Progress of the Solid State Lithium-Sulfur Batteries," Front. Energy Res., 7(112).

[3] Qiu, Z., Zhang, Y., Xia, S., and Dong, P., 2015, "Research Progress on Interface Properties of Inorganic Solid State Lithium Ion Batteries," Acta Chimica Sinica -Chinese Edition-, 73, pp. 992-1001.

[4] Liang, J.-Y., Zeng, X.-X., Zhang, X.-D., Wang, P.-F., Ma, J.-Y., Yin, Y.-X., Wu, X.-W., Guo, Y.-G., and Wan, L.-J., 2018, "Mitigating Interfacial Potential Drop of Cathode–Solid Electrolyte via Ionic Conductor Layer To Enhance Interface Dynamics for Solid Batteries," J. Am. Chem. Soc., 140(22), pp. 6767-6770.

[5] Inoue, T., and Mukai, K., 2017, "Are All-Solid-State Lithium-Ion Batteries Really Safe?–Verification by Differential Scanning Calorimetry with an All-Inclusive Microcell," ACS Appl. Mater. Interfaces, 9(2), pp. 1507-1515.

[6] Li, B., Parekh, M. H., Adams, R. A., Adams, T. E., Love, C. T., Pol, V. G., and Tomar, V., 2019, "Lithium-ion Battery Thermal Safety by Early Internal Detection, Prediction and Prevention," Sci. Rep., 9(1), p. 13255.

[7] Bandhauer, T. M., Garimella, S., and Fuller, T. F., 2011, "A Critical Review of Thermal Issues in Lithium-Ion Batteries," J. Electrochem. Soc., 158(3), pp. R1-R25.

[8] Chung, H., and Kang, B., 2017, "Mechanical and Thermal Failure Induced by Contact between a Li1.5Al0.5Ge1.5(PO4)3 Solid Electrolyte and Li Metal in an All Solid-State Li Cell," Chem. Mater., 29(20), pp. 8611-8619.

[9] Goodenough, J. B., and Park, K.-S., 2013, "The Li-Ion Rechargeable Battery: A Perspective," J. Am. Chem. Soc., 135(4), pp. 1167-1176.

[10] O'Brien, P. J., Shenogin, S., Liu, J., Chow, P. K., Laurencin, D., Mutin, P. H., Yamaguchi, M., Keblinski, P., and Ramanath, G., 2012, "Bonding-induced thermal conductance enhancement at inorganic heterointerfaces using nanomolecular monolayers," Nat. Mater., 12, p. 118.

[11] Kaur, S., Raravikar, N., Helms, B. A., Prasher, R., and Ogletree, D. F., 2014, "Enhanced thermal transport at covalently functionalized carbon nanotube array interfaces," Nat. Commun., 5, p. 3082.

[12] Reifenberg, J. P., Chang, K., Panzer, M. A., Kim, S., Rowlette, J. A., Asheghi, M., Wong, H. P., and Goodson, K. E., 2010, "Thermal Boundary Resistance Measurements for Phase-Change Memory Devices," IEEE Electron Device Lett., 31(1), pp. 56-58.

[13] Vishwakarma, V., Waghela, C., Wei, Z., Prasher, R., Nagpure, S. C., Li, J., Liu, F., Daniel, C., and Jain, A., 2015, "Heat transfer enhancement in a lithium-ion cell through improved material-level thermal transport," J. Power Sources, 300, pp. 123-131.

[14] Liu, T., Yue, S.-Y., Ratnasingham, S., Degousée, T., Varsini, P., Briscoe, J., McLachlan, M. A., Hu, M., and Fenwick, O., 2019, "Unusual Thermal Boundary Resistance in Halide Perovskites: A Way To Tune Ultralow Thermal Conductivity for Thermoelectrics," ACS Appl. Mater. Interfaces, 11(50), pp. 47507-47515.

[15] Zheng, K., Sun, F., Tian, X., Zhu, J., Ma, Y., Tang, D., and Wang, F., 2015, "Tuning the Interfacial Thermal Conductance between Polystyrene and Sapphire by Controlling the Interfacial Adhesion," ACS Appl. Mater. Interfaces, 7(42), pp. 23644-23649.

[16] Xu, H., Zhang, X., Hu, G., Weng, L., and Liu, L., 2020, "High thermal conductivity EP adhesive based on the GO/EP interface optimized by TDI," Polym. Adv. Technol., 31(6), pp. 1356-1364.

[17] Hu, M., Keblinski, P., and Schelling, P. K., 2009, "Kapitza conductance of silicon--amorphous polyethylene interfaces by molecular dynamics simulations," Phys. Rev. B, 79(10), p. 104305.

[18] Shen, M., Evans, W. J., Cahill, D., and Keblinski, P., 2011, "Bonding and pressure-tunable interfacial thermal conductance," Phys. Rev. B, 84(19), p. 195432.

[19] Zhang, Y., Han, H., Wang, N., Zhang, P., Fu, Y., Murugesan, M., Edwards, M., Jeppson, K., Volz, S., and Liu, J., 2015, "Improved Heat Spreading Performance of Functionalized Graphene in Microelectronic Device Application," Adv. Funct. Mater., 25(28), pp. 4430-4435.

[20] Losego, M. D., Grady, M. E., Sottos, N. R., Cahill, D. G., and Braun, P. V., 2012, "Effects of chemical bonding on heat transport across interfaces," Nat. Mater., 11, p. 502.

[21] Majumdar, S., Sierra-Suarez, J. A., Schiffres, S. N., Ong, W.-L., Higgs, C. F., McGaughey, A. J. H., and Malen, J. A., 2015, "Vibrational Mismatch of Metal Leads Controls Thermal Conductance of Self-Assembled Monolayer Junctions," Nano Lett., 15(5), pp. 2985-2991.

[22] Hu, M., Goicochea, J. V., Michel, B., and Poulikakos, D., 2010, "Water Nanoconfinement Induced Thermal Enhancement at Hydrophilic Quartz Interfaces," Nano Lett., 10(1), pp. 279-285.

[23] Wang, M., Hu, N., Zhou, L., and Yan, C., 2015, "Enhanced interfacial thermal transport across graphene–polymer interfaces by grafting polymer chains," Carbon, 85, pp. 414-421.

[24] Wang, Y., Zhan, H. F., Xiang, Y., Yang, C., Wang, C. M., and Zhang, Y. Y., 2015, "Effect of Covalent Functionalization on Thermal Transport across Graphene–Polymer Interfaces," The Journal of Physical Chemistry C, 119(22), pp. 12731-12738.

[25] Mosnáček, J., Popelka, A., Osicka, J., Filip, J., Ilcikova, M., Kollar, J., Yousaf, A. B., Bertok, T., Tkac, J., and Kasak, P., 2018, "Modulation of wettability, gradient and adhesion on self-assembled monolayer by counterion exchange and pH," J. Colloid Interface Sci., 512, pp. 511-521.

[26] Schoeppner, R., Ferguson, C., Pethö, L., Guerra-Nuñez, C., Taylor, A. A., Polyakov, M., Putz, B., Breguet, J.-M., Utke, I., and Michler, J., 2020, "Interfacial adhesion of alumina thin films over the full compositional range of ternary fcc alloy films: A combinatorial nanoindentation study," Materials & Design, 193, p. 108802.

[27] Chu, K., Wang, X.-h., Li, Y.-b., Huang, D.-j., Geng, Z.-r., Zhao, X.-l., Liu, H., and Zhang, H., 2018, "Thermal properties of graphene/metal composites with aligned graphene," Materials & Design, 140, pp. 85-94.

[28] Qiu, X., Ivasyshyn, V., Qiu, L., Enache, M., Dong, J., Rousseva, S., Portale, G., Stöhr, M., Hummelen, J. C., and Chiechi, R. C., 2020, "Thiol-free self-assembled oligoethylene glycols enable robust air-stable molecular electronics," Nat. Mater., 19(3), pp. 330-337.

[29] Minamiki, T., Ichikawa, Y., and Kurita, R., 2020, "Systematic Investigation of Molecular Recognition Ability in FET-Based Chemical Sensors Functionalized with a Mixed Self-Assembled Monolayer System," ACS Appl. Mater. Interfaces, 12(13), pp. 15903-15910.

[30] Lan, W.-C., Huang, T.-S., Cho, Y.-C., Huang, Y.-T., Walinski, C., Chiang, P.-C., Ruslin, M., Pai, F.-T., Huang, C.-C., and Huang, M.-S., 2020, "The Potential of a Nanostructured Titanium Oxide Layer with Self-Assembled Monolayers for Biomedical Applications: Surface Properties and Biomechanical Behaviors," Applied Sciences, 10, p. 590.

[31] Gärtner, M., 2018, "Understanding the Properties of Tailor-Made Self-Assembled Monolayers with Embedded Dipole Moments for Interface Engineering," J. Phys. Chem., v. 122(no. 50), pp. pp. 28757-28774-22018 v.28122 no.28750.

[32] Singh, M., Kaur, N., and Comini, E., 2020, "The role of self-assembled monolayers in electronic devices," J. Mater. Chem. C, 8(12), pp. 3938-3955.

[33] Wang, X., Liu, X., Yuan, H., Liu, H., Liu, C., Li, T., Yan, C., Yan, X., Shen, C., and Guo, Z., 2018, "Non-covalently functionalized graphene strengthened poly(vinyl alcohol)," Materials & Design, 139, pp. 372-379.

[34] Zhang, L., and Liu, L., 2017, "Polymeric Self-Assembled Monolayers Anomalously Improve Thermal Transport across Graphene/Polymer Interfaces," ACS Applied Materials & Interfaces, 9(34), pp. 28949-28958.

[35] Zhang, T., Gans-Forrest, A. R., Lee, E., Zhang, X., Qu, C., Pang, Y., Sun, F., and Luo, T., 2016, "Role of Hydrogen Bonds in Thermal Transport across Hard/Soft Material Interfaces," ACS Applied Materials & Interfaces, 8(48), pp. 33326-33334.

[36] Zhang, L., Ruesch, M., Zhang, X., Bai, Z., and Liu, L., 2015, "Tuning thermal conductivity of crystalline polymer nanofibers by interchain hydrogen bonding," RSC Adv., 5(107), pp. 87981-87986.

[37] Zhang, L., Bai, Z., Ban, H., and Liu, L., 2015, "Effects of the amino acid sequence on thermal conduction through β-sheet crystals of natural silk protein," PCCP, 17(43), pp. 29007-29013.

[38] Zhang, L., Chen, T., Ban, H., and Liu, L., 2014, "Hydrogen bonding-assisted thermal conduction in β-sheet crystals of spider silk protein," Nanoscale, 6(14), pp. 7786-7791.

[39] Xu, Y., Wang, X., Zhou, J., Song, B., Jiang, Z., Lee, E. M. Y., Huberman, S., Gleason, K. K., and Chen, G., 2018, "Molecular engineered conjugated polymer with high thermal conductivity," Sci. Adv., 4(3), p. eaar3031.

[40] Wei, X., Zhang, T., and Luo, T., 2017, "Thermal Energy Transport across Hard–Soft Interfaces," ACS Energy Lett., 2(10), pp. 2283-2292.

[41] Lai, J.-C., Li, L., Wang, D.-P., Zhang, M.-H., Mo, S.-R., Wang, X., Zeng, K.-Y., Li, C.-H., Jiang, Q., You, X.-Z., and Zuo, J.-L., 2018, "A rigid and healable polymer cross-linked by weak but abundant Zn(II)-carboxylate interactions," Nat. Commun., 9(1), p. 2725.

[42] Mizushima, K., Jones, P. C., Wiseman, P. J., and Goodenough, J. B., 1981, "LixCoO2 ($0<x\leqslant 1$): A new cathode material for batteries of high energy density," Solid State Ionics, 3-4, pp. 171-174.

[43] Humphrey, W., Dalke, A., and Schulten, K., 1996, "VMD: Visual molecular dynamics," J. Mol. Graph., 14(1), pp. 33-38.

[44] Kim, H., Abdala, A. A., and Macosko, C. W., 2010, "Graphene/Polymer Nanocomposites," Macromolecules, 43(16), pp. 6515-6530.

[45] Majumdar, S., Malen, J. A., and McGaughey, A. J. H., 2017, "Cooperative Molecular Behavior Enhances the Thermal Conductance of Binary Self-Assembled Monolayer Junctions," Nano Lett., 17(1), pp. 220-227.

[46] Severin, J., and Jund, P., 2017, "Thermal conductivity calculation in anisotropic crystals by molecular dynamics: Application to α−Fe2O3," J. Chem. Phys, 146(5), p. 054505.

[47] Plimpton, S., 1995, "Fast Parallel Algorithms for Short-Range Molecular Dynamics," Journal of Computational Physics, 117(1), pp. 1-19.

[48] Hart, F. X., and Bates, J. B., 1998, "Lattice model calculation of the strain energy density and other properties of crystalline LiCoO2," J. Appl. Phys., 83(12), pp. 7560-7566.

[49] Lewis, G. V., and Catlow, C. R. A., 1985, "Potential models for ionic oxides," J. Phys. C: Solid State Phys., 18(6), pp. 1149-1161.

[50] Jorgensen, W. L., Maxwell, D. S., and Tirado-Rives, J., 1996, "Development and Testing of the OPLS All-Atom Force Field on Conformational Energetics and Properties of Organic Liquids," J. Am. Chem. Soc., 118(45), pp. 11225-11236.

[51] Price, M. L. P., Ostrovsky, D., and Jorgensen, W. L., 2001, "Gas-phase and liquid-state properties of esters, nitriles, and nitro compounds with the OPLS-AA force field," J. Comput. Chem., 22(13), pp. 1340-1352.

[52] Godawat, R., Jamadagni, S. N., and Garde, S., 2009, "Characterizing hydrophobicity of interfaces by using cavity formation, solute binding, and water correlations," Proceedings of the National Academy of Sciences, 106(36), p. 15119.

[53] Kuang, S., and Gezelter, J. D., 2011, "Simulating Interfacial Thermal Conductance at Metal-Solvent Interfaces: The Role of Chemical Capping Agents," The Journal of Physical Chemistry C, 115(45), pp. 22475-22483.

[54] Sun, F., Zhang, T., Jobbins, M. M., Guo, Z., Zhang, X., Zheng, Z., Tang, D., Ptasinska, S., and Luo, T., 2014, "Molecular Bridge Enables Anomalous Enhancement in Thermal Transport across Hard-Soft Material Interfaces," Adv. Mater., 26(35), pp. 6093-6099.

[55] Rappe, A. K., Casewit, C. J., Colwell, K. S., Goddard, W. A., and Skiff, W. M., 1992, "UFF, a full periodic table force field for molecular mechanics and molecular dynamics simulations," J. Am. Chem. Soc., 114(25), pp. 10024-10035.

[56] Li, B., Lan, J., and Wang, L., 2005, "Interface Thermal Resistance between Dissimilar Anharmonic Lattices," Phys. Rev. Lett., 95(10), p. 104302.

[57] E. Mark, J., 2007, Physical Properties of Polymer Handbook.

[58] Lu, C., Chiang, S. W., Du, H., Li, J., Gan, L., Zhang, X., Chu, X., Yao, Y., Li, B., and Kang, F., 2017, "Thermal conductivity of electrospinning chain-aligned polyethylene oxide (PEO)," Polymer, 115, pp. 52-59.

[59] He, J., Zhang, L., and Liu, L., 2019, "Thermal transport in monocrystalline and polycrystalline lithium cobalt oxide," PCCP, 21(23), pp. 12192-12200.

[60] Zhang, L., and Liu, L., 2019, "Hierarchically hydrogen-bonded graphene/polymer interfaces with drastically enhanced interfacial thermal conductance," Nanoscale, 11(8), pp. 3656-3664.

[61] Xu, Y., Kraemer, D., Song, B., Jiang, Z., Zhou, J., Loomis, J., Wang, J., Li, M., Ghasemi, H., Huang, X., Li, X., and Chen, G., 2019, "Nanostructured polymer films with metal-like thermal conductivity," Nat. Commun., 10(1), p. 1771.

[62] Luo, T., and Lloyd, J. R., 2012, "Enhancement of Thermal Energy Transport Across Graphene/Graphite and Polymer Interfaces: A Molecular Dynamics Study," Adv. Funct. Mater., 22(12), pp. 2495-2502.

[63] Shenogina, N., Godawat, R., Keblinski, P., and Garde, S., 2009, "How Wetting and Adhesion Affect Thermal Conductance of a Range of Hydrophobic to Hydrophilic Aqueous Interfaces," Physical Review Letters, 102(15), p. 156101.

[64] Zhang, L., Bai, Z., and Liu, L., 2016, "Exceptional Thermal Conductance across Hydrogen-Bonded Graphene/Polymer Interfaces," Advanced Materials Interfaces, 3(13), p. 1600211.

[65] Liu, X., Gao, J., Zhang, G., and Zhang, Y.-W., 2018, "Design of phosphorene/graphene heterojunctions for high and tunable interfacial thermal conductance," Nanoscale, 10(42), pp. 19854-19862.

[66] Cahill, D. G., Braun, P. V., Chen, G., Clarke, D. R., Fan, S., Goodson, K. E., Keblinski, P., King, W. P., Mahan, G. D., Majumdar, A., Maris, H. J., Phillpot, S. R., Pop, E., and Shi, L., 2014, "Nanoscale thermal transport. II. 2003–2012," Appl. Phys. Rev., 1(1), p. 011305.

CHAPTER 4

HYDROGEN-BOND CONFIGURATION MODULATES ENERGY TRANSFER EFFICIENCY IN HELICAL PROTEIN NANOTUBES

4.1 Abstract

Energy transport in proteins is critical to a variety of physical, chemical, and biological processes in living organisms. While strenuous efforts have been made to study vibrational energy transport in proteins, thermal transport processes across the most fundamental building blocks of proteins, i.e. helices, are not well understood. This work studies energy transport in a group of "isomer" helices. The π-helix is shown to have the highest thermal conductivity, 110% higher than that of the α-helix and 207% higher than that of the 3_{10}-helix. The H-bond connectivity is found to govern thermal transport mechanisms including phonon spectral energy density, dispersion, mode-specific transport, group velocity, and relaxation time. The energy transport is strongly correlated with H-bond strength which is also modulated by the H-bond connectivity. These fundamental insights provide a novel perspective for understanding energy transfer in proteins and guiding a rational molecule-level design of novel materials with configurable H-bonds.

4.2 Introduction

Energy transport and atomic vibrations in biomacromolecules such as proteins are critical to a variety of physical, chemical and biological processes taking place in living

---

He, J., Zhang, L., and Liu, L., "Hydrogen-Bond Configuration Modulates Energy Transfer Efficiency in Helical Protein Nanotubes." Nanoscale, (Under Revision)

organisms, from structural construction, catalysis, to molecular recognition [1-5]. In principle, the vibrational energy flow is strongly associated with structural characteristics of proteins including the conformation, amino acid sequence, and intermolecular affinities [6-9]. Due to their polymeric nature, proteins generate intricate macromolecular structures as they attain their biological states in the process of folding. Secondary structures are formed as an information bridge that links the primary sequence with substructures to shape the protein systems. Representative protein secondary structures include the β-sheet, 3_{10}-helix, α-helix and π-helix. They are stable and energetically favorable, primarily due to many interlocking hydrogen bonds (H-bonds) that exist between carbonyl (C=O) and amide (N−H) groups (**Figure 4.1**g). Establishing the relationship between protein structures and energy transport pathways is an important area of fundamental interest to better understand protein reactivity and functionality. Further, the molecular insights gained from the study of nanoscale thermal transport in proteins may also inspire the design of new materials with novel structures and unprecedented properties.

Strenuous efforts have been made to probe energy transport in proteins and protein secondary structures such as the heme cooling cofactor [10], peptide helices [11], and the β-sheet [12, 13]. On one hand, evidences show that heat diffusion is integrated with allosteric communication pathways [14-16] which are closely related with the cellular and physiological functions of proteins [17-19]. On the other hand, studies demonstrate that heat spreads through multiple pathways including the covalent backbone as well as the relatively weak inter/intra-molecular interactions in protein secondary structures. As such, the energy transport processes may be modulated by tuning the inter/intra-molecular interactions [20],

where the H-bond is arguably one of the most important factors. Although being a secondary bond, the H-bond is critical in proteins as it largely controls their structural stability [21, 22], catalytic properties [23-25], chemical reactivity [26, 27], and energy transport [8]. Recent studies have reported that the H-bond significantly enhances thermal transport in the β-sheet of spider silk proteins [12] and a variety of polymer blends [28].

Despite the progress, vibrational energy transport in helical protein structures are underexplored. As biomolecular "nanowires", protein helices differ from any other nanowires in that they uniquely feature tortuous covalent backbones interlocked by H-bonds. Different H-bond connectivities lead to different types of helices in the protein database, which include the 3_{10}-helix, α-helix, and the π-helix. While the 3_{10}-helix widely exists in many biological channels and membrane proteins [29] (e.g. ABC-ATPase SufC as shown in **Figure 4.1**a), the α-helix is commonly found in globular proteins [30] (e.g. T4 Lysozyme as shown in **Figure 4.1**b) and the π-helix is usually identified near functional sites of proteins [31] (e.g. PGRP-SA as shown in **Figure 4.1**c). All composed of single amino acid chains, these helices are differentiated by the different atomic sites of forming H-bonds. For example, **Figure 4.1**d-f illustrates ribbon schematics of the 3_{10}-helix, α-helix and π-helix, respectively. In the 3_{10}-helix, H-bonds are established between the CO group of the *i*-th residue and the NH group of the (*i*+3)th residue. By comparison, H-bonds of the α-helix are formed between the *i*-th and the (*i*+4)th residues, while those of the π-helix are formed between the *i*-th and the (*i*+5)th residues. The different H-bond network leads to significantly different structural characteristics of the three helices including the number of amino acids per turn and the helical pitch. Understanding energy transport in such helical

structures may fundamentally reveal how the H-bond, together with the helical backbone, dictates vibrational energy flow in proteins.

This work investigates vibrational energy transfer and thermal transport mechanisms in the three key building blocks of proteins including the 3_{10}-, α-, and π-helices. To focus on the important effects of H-bond connectivity, three model helices are assumed which have the same amino acid sequence of poly-Glycine. The molecular structures of these helix "isomers" are shown in **Figure 4.1**h-i. These "isomer" helices feature different H-bond connectivities as illustrated in **Figure 4.1**d-f for the 3_{10}-, α-, and π-helices, respectively. Using the molecular dynamic (MD) simulation and vibrational energy transfer analysis, we demonstrate that the π-helix has the largest thermal conductivity, followed by the α-helix and then the 3_{10}-helix. Energy transfer mechanisms are explored via the analysis of phonon dispersion, spectral thermal conductivity, relaxation time, and group velocity. Results show that the different H-bond networks that form the "isomer" helices fundamentally change the behavior of both low-frequency acoustic and semi-optical phonons. The energy transport properties of the three types of helices are strongly correlated with the different strengths of intramolecular H-bonds as revealed by quantum-chemical analyses based on the density functional theory (DFT) calculations. The results enrich our fundamental understanding of the energy transfer in protein structures and the critical role of interlocking H-bonds. The understanding may open new avenues to design novel biomacromolecules with extraordinary energy transfer properties for a wide range of applications.

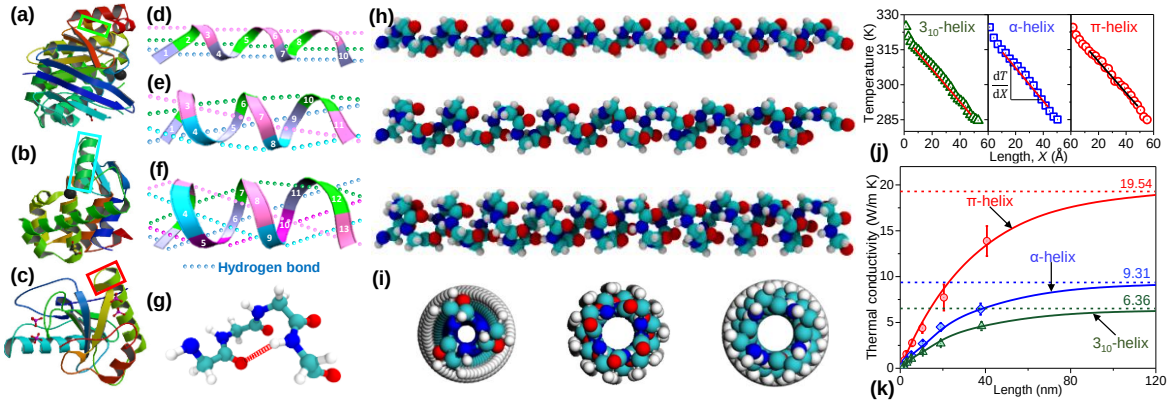

Figure 4.1. Helix segments in example proteins: [32-34] (a) ABC-ATPase SufC with the 3_{10}-helix (in green box), (b) T4 Lysozyme with the α-helix (in cyan box), and (c) PGRP-SA with the π-helix (in red box). Different types of helices are interlocked by different H-bond networks: (d) the 3_{10}-helix has H-bonds connecting residues *i* and *i* + 3; (e) the α-helix has H-bonds connecting residues *i* and *i* + 4; and (f) the π-helix has H-bonds connecting residues *i* and *i* + 5. (g) Illustration of a H-bond between the carbonyl (C=O) and amide (N−H) groups. Three isomer helices with the same amino acid sequence of poly-Glycine but different H-bond connectivities to form three types of helices: (h) side and (i) cross-sectional views. (j) Temperature profiles of the helices in NEMD simulation. (k) Thermal conductivity of the 3_{10}-, α- and π-helices with varying lengths. Curves are fitted against an empirical equation of the length-dependent thermal conductivity. Dashed lines show thermal conductivities in the diffusive limit.

4.3 Models and Methods

4.3.1 Models

Three "isomer" helices were created with the same amino acid sequence of poly-Glycine, where Glycine has a composition of –HN–HC$_\alpha$H–C=O–. The three helices include a 3_{10}-helix, a α-helix and a π-helix. They feature different atomic sites to form H-bonds (**Figure 4.1**d-f): the 3_{10}-helix has H-bonds formed between the CO group at the *i*-th residue and the NH group at the (*i*+3)th residue; the α-helix has H-bonds between the *i*-th and (*i*+4)th residues; and the π-helix has H-bonds between the *i*-th and (*i*+5)th residues. The different sites of H-bonding vary the structural properties of helices. The 3_{10}-helix has

3 amino acids per turn, a helical pitch of 0.60 nm per turn, and a rise per helical residue of 0.20 nm. The α-helix has 3.6 residues per turn, a helical pitch of 0.54 nm per turn, and a rise per helical residue of 0.15 nm. The π-helix has 4.4 residues per turn, a helical pitch of 0.48 nm per turn, and a rise per helical residue of 0.12 nm.

4.3.2 Molecular Dynamics

MD simulation was conducted with LAMMPS [35]. Interatomic interactions were described by the CHARMM22 force field [36] that is widely used for peptide and protein simulations. The particle-particle particle-mesh method (PPPM) was used to describe long range Coulomb interactions with a root mean square accuracy of 10^{-6}. Time step was set to be 0.25 fs, small enough to capture most vibrational modes. Periodic boundary conditions were imposed to the helices along all directions. Large spaces were left along transverse directions to prevent the model from interacting with its periodic images. Angular momentum was zeroed out at every step to eliminate potential rigid-body rotations. Initial molecular structures were optimized at 300 K to ensure the formation of H-bonds at selected sites leading to the 3_{10}-helix, α-helix and π-helix. The structures were then equilibrated at 300 K for 20 ns under the NVT ensemble. Identification of the H-bond was based on a geometric rule: (1) distance between the donor (D) atom and the acceptor (A) atom is < 3.5 Å; and (2) the angle of D-H-A is < 30°.

4.3.3 Thermal Conductivity Calculation

Nonequilibrium molecular dynamics (NEMD) simulations were performed to calculate thermal conductivities. The NEMD simulation setup is shown in **Figure C.1**a-c

for the 3_{10}-, α- and π-helices, respectively. Each simulation system was divided into *N* slabs along the length direction. Atoms in the two end slabs were fixed to avoid an entropic state of helical chains. Thermal gradient was established by imposing Langevin thermostats of 325 K and 285 K in two slabs next to the fixed slabs, respectively, leading to a system temperature difference of $\Delta T = 40°C$. The system was equilibrated for 20 ns under the NVE ensemble, leading to a smooth thermal gradient between the heat source and heat sink slabs. Production runs were then performed for a duration of 10 ns. At every time step, the energy needed to keep ΔT a constant was evaluated and denoted by ΔE. Heat flow in the system, *J*, was calculated by $J = \Delta E/(A\Delta t)$, where Δt is the time step, and *A* is the effective cross sectional area of the helices as shown in **Figure C.1**d-f. Outside and inside radii of the helical tubes were determined by spatially and temporally averaging atomic positions during 2000 steps of MD calculations at equilibrium. The cross-sectional area, *A*, is calculated to be 20.36 $Å^2$, 22.82 $Å^2$ and 26.26 $Å^2$ for the 3_{10}-, α-, and π-helices, respectively. The thermal conductivity, *k*, was calculated by $k = J/(dT/dX)$. Here, dT/dX is the thermal gradient which is obtained by fitting a linear region of the temperature profile as shown in **Figure 4.1**j.

4.3.4 Phonon Spectral Energy Density

The PSED analysis was performed to obtain phonon properties including the dispersion curve, group velocity, relaxation time, and the mode-based thermal conductivity. The approach has been verified and applied for various materials systems [37-42]. The PSED analysis uses atomic velocities from the MD simulation which naturally includes anharmonic effects, phonon-phonon scattering, and Normal and Umklapp scattering. To

calculate PSED, the smallest atomic group that represents a helical structure is defined as the unit cell, and each helix model has multiple unit cells along the length direction. The unit cell has the length of 13.37 Å, 12.08 Å and 10.38 Å, respectively, for the 3_{10}-, α- and π-helix. Based on lattice dynamic and Parseval's theorem [43, 44], atomic trajectories in the real space are mapped to normal vibration modes in the frequency space, $q\binom{\boldsymbol{\kappa}}{\nu};t\big)$. Here, $\boldsymbol{\kappa}$ is the wave vector, ν labels the polarization branch, and t is time. The PSED is a weighted average of the contributions made by all atoms to the amplitude of normal modes, i.e. $\Phi(\boldsymbol{\kappa},\omega)=\frac{1}{2\pi\tau_0 N_T}\sum_\alpha\sum_j^{N_A} m_j\left|\int_0^{\tau_0}\sum_l^{N_T}\dot{u}_\alpha\left(\begin{smallmatrix}l\\j\end{smallmatrix};t\right)\times\exp\left[i\boldsymbol{\kappa}\cdot\boldsymbol{r}_0\binom{l}{0}-i\omega t\right]dt\right|^2$. Here, $\Phi(\boldsymbol{\kappa},\omega)$ is the PSED as a function of $\boldsymbol{\kappa}$ and the angular frequency ω, τ_0 is the simulation time, N_T is the total number of unit cells, N_A is the total number of atoms in an unit cell, m_j is mass of the *j*-th atom, $\dot{u}_\alpha\left(\begin{smallmatrix}l\\j\end{smallmatrix};t\right)$ denotes the velocity of the *j*-th atom in the *l*-th unit cell along the α-th direction at simulation time *t*, $\boldsymbol{r}_0\binom{l}{0}$ is the equilibrium position of the *l*-th unit cell. For one-dimensional helices, the wave vector is limited to $\kappa_x=2\pi n_x/a_x N_T$, where a_x is the unit cell length along the *x*-direction, and n_x is an integer ranging from 0 to N_T-1. Then, κ_x is mapped into $N_x/2$ points ranging from 0 to $2\pi/a_x$, which correspond to the first Brillouin zone in the real space from Γ to K point. Atomic velocities were collected from MD simulations of τ_0 = 1 ns under the NVE ensemble at 298 K.

4.3.5 Dispersion Curves

Based on the PSED profile, phono dispersion can be obtained by identifying peaks of the degenerate branches and connecting the peaks into continuous curves along the wave

vector direction. The dispersion curves correlate phonon frequency ($f = \omega/2\pi$, in the unit of THz) with the reduced wave vector ($\xi = \kappa_x/(2\pi/a_x)$, dimensionless). Dispersion curves in this work were obtained at a resolution of 0.001 THz × 0.01.

4.3.6 Mode-based Thermal Conductivity

By solving the Boltzmann transport equation [45] with phonon relaxation time approximation [46], the overall thermal conductivity is $k_x = \sum_{\boldsymbol{\kappa}} \sum_{\nu} \widetilde{k_x}(\boldsymbol{\kappa}, \nu)$, where $\widetilde{k_x}(\boldsymbol{\kappa}, \nu)$ is the thermal conductivity contributed by each phonon mode that belongs to a phonon branch, ν, with a wave number of κ_x. The mode-based thermal conductivity has an expression of $\widetilde{k_x}(\boldsymbol{\kappa}, \nu) = c_{ph} v_{g,x}^2(\boldsymbol{\kappa}, \nu)\tau(\boldsymbol{\kappa}, \nu)$, where c_{ph} is the volumetric phonon specific heat, $v_{g,x}(\boldsymbol{\kappa}, \nu)$ is the group velocity, and $\tau(\boldsymbol{\kappa}, \nu)$ is the phonon relaxation time. In classical systems, $c_{ph} = k_B/V$, where k_B is Boltzmann constant and *V* is the system volume. The group velocity $v_{g,x}(\boldsymbol{\kappa}, \nu) = \partial\omega/\partial\kappa_x$, which can be calculated based on the PSED result by using numerical differentiation.

4.3.7 Relaxation Time

PSED can be reconstructed into a different form which is in terms of the phonon relaxation time, i.e. $\Phi(\boldsymbol{\kappa}, f) = \sum_{\nu}^{3n} C(\boldsymbol{\kappa}, \nu)/(\left[4\pi\tau(\boldsymbol{\kappa}, \nu)\left(f - f_0(\boldsymbol{\kappa}, \nu)\right)\right]^2 + 1)$, where *f* is the phonon frequency, $C(\boldsymbol{\kappa}, \nu)$ is a mode-dependent constant, and $f_0(\boldsymbol{\kappa}, \nu)$ is the frequency at which PSED reaches a localized peak. At each $\boldsymbol{\kappa}$, the PSED data is converted into a single-variable data series in terms of f. The data series has $3n$ local peaks where n is the number of atoms and $3n$ is the number of phonon branches in the system. The data series is fitted using multiple Lorentzian functions, $\Phi = I/(1 + [(f - f_c)/\gamma]^2)$,

near local peaks. Here, I is the peak magnitude, f_c is the frequency at the peak, and γ is the half-width at the half-peak. The reconstructed PSED function can be described as a superposition of the Lorentzian functions identified for all phonon branches at a given wave vector. Finally, relaxation time associated with all phonon modes, $\tau(\boldsymbol{\kappa}, \nu)$, can be determined based on the parameters of the Lorentzian functions.

4.3.8 DFT Calculation

Quantum-chemical calculations were conducted to quantitatively study the H-bonds using Gaussian [47]. The calculations were based on the hybrid B3LYP exchange-correlation functional with Grimme's DFT-GD3(BJ) empirical dispersion correction. The B3LYP-GD3(BJ) theory has been widely used for studying H-bonds [48]. The ma-TZVPP basis set was employed. It is the "minimally augmented" version of the def2-TZVPP basis set [49, 50], for which *s* and *p* type diffuse basis functions are added to non-H atoms. Using this theory, equilibrium geometries of the 3_{10}-, α- and π-helices were obtained by geometric optimization. Frequency calculations were performed to confirm structural stabilization. Wave functions were output for subsequent calculations of the H-bond chemistry.

4.3.9 Quantum-Chemical H-bond Calculation

Based on the wave functions calculated by DFT, strength of the H-bond was quantified using two numeric indices: (1) the core-valence bifurcation index (CVBI), and (2) the H-bond energy evaluated at the bond critical point. On the one hand, the CVBI is a widely used approach based on the electron localization function (ELF) theory [51, 52]. The ELF takes the form of $\eta(r) = 1/\{1 + [D(r)/D_0(r)]^2\}$, where $D(r)$ is the Pauli kinetic energy density and $D_0(r)$ is the Thomas-Fermi kinetic energy density. For a H-bond

taking the general form of D−H···A, bifurcation points of the ELF are first identified through a topological analysis, based on which the (3,−1) critical points are located. The CVBI is calculated by CVBI = ELF(C−V, D) − ELF(DH···A) [53, 54], where ELF(C−V, D) is the core-valence bifurcation value at donor (D), and ELF(DH···A) stands for the valence-valence bifurcation value at the H-bond. The CVBI is a numeric indicator of the strength of the H-bond; the lower CVBI, the stronger H-bond. A negative CVBI suggests that the H-bond has a covalence characteristic, whereas a positive CVBI means that the H-bond has an electrostatic nature. On the other hand, the H-bond strength can be evaluated directly based on the electron density at the bond critical point, i.e. the (3,−1) critical point associated with DH···A, on the basis of the quantum theory of atoms in molecules (QTAIM). The equation takes the form of $E_{\mathrm{HB}} = A\rho_{\mathrm{BCP}} + B$, where E_{HB} is the H-bond energy, ρ_{BCP} is the electron density at the bond critical point, and A and B are parameters depending on the H-bond type and the level of quantum chemical calculation [55-58]. In this work, A = –223.08 and B = 0.7423 were adopted [59], which were optimized and proven to effectively characterize the H-bond strength in biologically important substances. The calculation was performed by using the MULTIWFN program at the same level of theory [60].

4.4 Results and Discussion

4.4.1 Thermal Conductivity

Vibrational energy transport in “isomer” protein helices is first studied by quantifying and comparing how fast energy is conducted in these structures. **Figure 4.1**k plots the thermal conductivity calculated by MD simulation for the 3_{10}-, α- and π-helices

with various lengths including 2 nm, 3 nm, 5 nm, 10 nm, 20 nm, and 40 nm. Since helical segments in proteins are usually short with only a few nanometers in length, vibrational energy carriers, i.e. phonons, are not relaxed and their transport is constrained by and sensitive to the geometry. As shown in **Figure 4.1**k, the thermal conductivity (k_x) of the helices increases nonlinearly with the length (L), conforming to the ballistic-diffusive empirical formula, $k_x = k_{x,\infty}\left(1 - e^{-L/L_c}\right)$, where $k_{x,\infty}$ is the thermal conductivity in the diffusive limit and L_c denotes a characteristic length of the ballistic-to-diffusive transition. Another ballistic-diffusive characteristic is demonstrated in **Figure C.2**, which shows that $1/k_x$ and $1/L$ are almost linearly correlated except when the helix length is extremely short. By fitting computational results of k_x with the empirical formula, thermal conductivity in the diffusive limit ($k_{x,\infty}$) is predicted to be 6.36 W m^{-1} K^{-1} for the 3_{10}-helix, 9.31 W m^{-1} K^{-1} for the α-helix, and 19.54 W m^{-1} K^{-1} for the π-helix. Among the three helical "isomers", the π-helix is the most thermally conductive, followed by the α-helix (52.35% lower $k_{x,\infty}$) and 3_{10}-helix (67.45% lower $k_{x,\infty}$). The phonon mean free path that corresponds to fully diffusive phonon transport is approximated by $L_{0.99}$, namely, the length at which thermal conductivity $k_x = 0.99k_{x,\infty}$. Based on the empirical formula with predicted $k_{x,\infty}$, the phonon mean free path is approximated as 139.39 nm, 148.10 nm and 160.02 nm for the 3_{10}-, α- and π-helices, respectively. The π-helix, which has the higher thermal conductivity, is also found to have longer phonon mean free path. The empirical equation is important because nearly all helix segments in proteins are short in length so they are in the ballistic-to-diffusive transition regime.

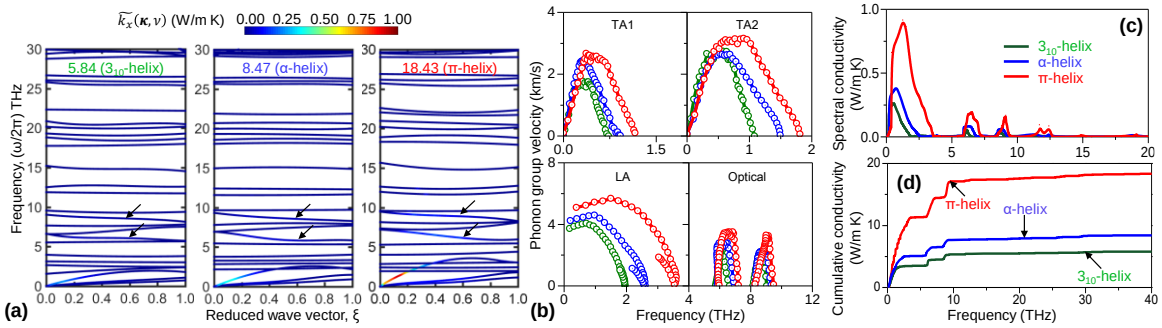

Figure 4.2. (a) Phonon dispersion curves of three isomer helices in the first Brillouin zone. Colors show mode-by-mode contributions to the thermal conductivity, i.e. $\widetilde{k_x}(\boldsymbol{\kappa},\nu)$. Arrows indicate two semi-optical branches with significant $\widetilde{k_x}(\boldsymbol{\kappa},\nu)$. (b) Frequency-dependent group velocities for three acoustic branches and two selected optical branches of the 3_{10}-helix (green), α-helix (blue), and π-helix (red). (c) Spectral thermal conductivity and (d) cumulative thermal conductivity of the three isomer helices.

4.4.2 Phonon Vibrational Spectra

Effects of H-bond connectivity on phonon vibrational spectra can be found in the phonon dispersion curves plotted for the three isomer helices (**Figure 4.2**a). The calculations are thermodynamically stable as no imaginary frequency is found in the curves. Only the regime with frequency < 30 THz is displayed. Phonons with higher frequencies are associated with localized interactions so they have low group velocities and short relaxation times [37, 38, 61, 62]. Each helix shows three lowest-lying phonon branches including two transverse acoustic branches (TA1 and TA2) and one longitudinal acoustic branch (LA). The two TA branches show almost linear dispersion, whereas the LA branch is nearly quadratic. Among the three acoustic branches, the LA branch has the largest slope, followed by the TA1 branch and then the TA2 branch. Although most optical phonon branches are relatively flat indicating negligible contributions to energy transport, all three

helices show some optical branches that have significant slopes especially in the frequency range of 5-10 THz.

The group velocity for three acoustic branches and two selected optical branches are plotted in **Figure 4.2**b. The two chosen optical branches (indicated by arrows in **Figure 4.2**a) contribute significantly to energy transport as discussed in the following section using the mode-based thermal conductivity analysis. All branches except LA show bell-shaped group velocity curves that peak approximately in the middle. By comparison, the LA branch uniquely features an unsymmetrical curve with curve branching at the high frequency end. Comparing the curves, it is readily seen that the LA branch has the highest group velocity followed by the TA2 and TA1 branches, echoing the findings relating to the slope of dispersion curves. The two optical branches show similar group velocities as the TA1 and TA2 branches.

Importantly, the three isomer helices show critical differences as a result of their different H-bond connectivities. On the one hand, the π-helix exhibits the highest group velocity in all shown branches, followed by the α- and 3_{10}-helices. These results agree well with the ranking of the isomers in terms of their overall thermal conductivities. On the other hand, an interesting "redshift" is identified among the isomers. For example, the frequency at which the LA branch's group velocity peaks is found to redshift from 1.50 THz for the π-helix to 0.97 THz for the α-helix, and then further redshift to 0.71 THz for the 3_{10}-helix. The same trend persists in the other acoustic and optical phonon modes of importance to the energy transport processes.

4.4.3 Mode-Specific Contribution to Energy Transport

Based on the PSED analysis (**Figure C.3**), **Figure 4.2**a uses the line color to plot the contribution to energy transport made by phonons of particular wave vector and frequency, i.e. $\widetilde{k_x}(\boldsymbol{\kappa}, \nu)$. It is apparent that the LA branch, especially when ξ = 0.05 ~ 0.4, makes the most prominent contribution to energy transport. The TA1 and TA2 branches in similar frequency ranges also contribute significantly. Summing up $\widetilde{k_x}(\boldsymbol{\kappa}, \nu)$ for the three branches, the LA branch is found to contribute about 38-40% thermal conductivity for all of the three helices, followed by the TA2 and TA1 branches which contribute about 13% and about 5-7%, respectively. The three acoustic branches together account for 57.70%, 58.21% and 59.99% of the overall thermal conductivity for the 3_{10}-, α- and π-helices, respectively. Therefore, heat is mainly carried by acoustic phonons in biomolecular helices.

In addition to acoustic phonons, some optical branches especially the two indicated by arrows in **Figure 4.2**a also make important contributions as determined by their values of $\widetilde{k_x}(\boldsymbol{\kappa}, \nu)$. According to the mode-based thermal conductivity results shown in **Figure 4.2**c, semi-optical branches in the range of 5-10 THz contribute 31.32%, 30.35% and 31.24% to the overall thermal conductivity for the 3_{10}-, α- and π-helices, respectively. **Figure 4.2**d further shows that, for all helix isomers, the cumulative thermal conductivity increases significantly only in the frequency ranges of acoustic phonons and low-frequency semi-optical phonons. The cumulative thermal conductivity curve almost plateaus after 30 THz. Therefore, acoustic phonons and semi-optical phonons with low frequencies make the most important contributions to energy transfer in biomolecular helices. They together account for about 90% of the overall thermal conductivity of the helix isomers under investigation.

The mode-based analysis also provides a means to verify the thermal conductivities calculated by MD simulation shown in **Figure 4.1**k. Using the mode-based thermal conductivity results, the overall thermal conductivity can be calculated via $k_x = \sum_{\boldsymbol{\kappa}} \sum_{\nu} \widetilde{k_x}(\boldsymbol{\kappa}, \nu)$ which sums up the contributions made by all phonon branches. By using this approach, the overall thermal conductivity is found to be 5.84 W m^{-1} K^{-1} for the 3_{10}-helix, 8.47 W m^{-1} K^{-1} for the α-helix, and 18.43 W m^{-1} K^{-1} for the π-helix. These results are in good agreement with the conductivities calculated using MD directly. Both show profound effects of the H-bond configuration on energy transport.

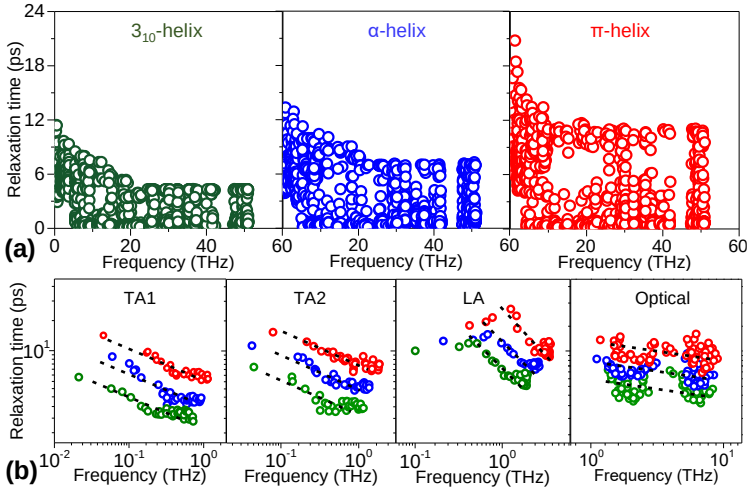

Figure 4.3. (a) Frequency-dependent relaxation time of three isomer helices. (b) Relaxation time for three acoustic branches and two selected optical branches of the 3_{10}-helix (green), α-helix (blue), and π-helix (red). Back dashed lines are fitted against a relationship of $\tau \propto f^{-\alpha}$.

4.4.4 Phonon Relaxation Time

The different H-bond connectivity in helices also influences phonon-phonon scattering. **Figure 4.3**a plots full-mode relaxation time (τ) within the first Brillouin zone as a function of phonon frequency (f) for the 3_{10}-, α- and π-helices. On the one hand,

relaxation time is in general shortened with increasing f in the low-frequency range where phonons carry most of the heat. The largest τ in this regime is about 10.93 ps for the 3_{10}-helix, 13.98 ps for the α-helix, and 20.20 ps for the π-helix. On the other hand, at higher frequencies, τ is well below a threshold that is frequency-independent. The threshold is about 4.45 ps, 7.04 ps and 11.06 ps for the 3_{10}-, α-, π-helices, respectively. In both frequency regimes, the isomer helices show different upper bounds of τ as a result of their different H-bond networks. The π-helix is shown to have the longest τ, indicating the weakest phonon scattering. By contrast, the 3_{10}-helix is found to have the shortest τ and the strongest phonon scattering, mainly due to its slender helical structure with more frequent H-bonds along the backbone.

Figure 4.3b further plots τ for selected phonon branches that contribute the most to energy transport, including three acoustic branches and two semi-optical branches indicated by arrows in **Figure 4.2**a. All of these branches are in the low-frequency regime, and an approximately linear relationship is found between $\log(\tau)$ and $\log(f)$. Among the five branches, the acoustic branches are found to have the most significant frequency dependence of τ. As f increases, τ in these three branches descends quickly and almost monotonically indicating increasing phonon scattering. For all three isomer helices, the rate of descendance is the highest in LA with $\tau \propto f^{-1.77}$, very close to the well-known Klemens scaling relationship [63]. The descendance is slower in the other two acoustic branches, with $\tau \propto f^{-0.66}$ for TA1 and $\tau \propto f^{-0.73}$ for TA2. Compared with the acoustic branches, the two semi-optical branches show much slower descendance with approximately $\tau \propto f^{-0.19}$.

Interestingly, in the vicinity of Brillouin zone center, the $\tau - f$ data points for the LA branch show a tendency to diverge from the relationship of $\tau \propto f^{-1.77}$. When phonons are populated at small wave vectors, it has been previously discovered for a single polymer chain that Umklapp scattering is "frozen out" and Normal scattering dominates phonon interactions in the LA branch [64]. Hence, near the Brillouin zone center, LA phonon scattering is fundamentally different from that in the other regions governed by a mixture of Umklapp and Normal scattering. Since the predominant Normal scattering is known to usually have high relaxation rates, τ of the LA branch drops at low $\boldsymbol{\kappa}$ and low f, leading to the downwards divergence as shown in **Figure 4.3**b.

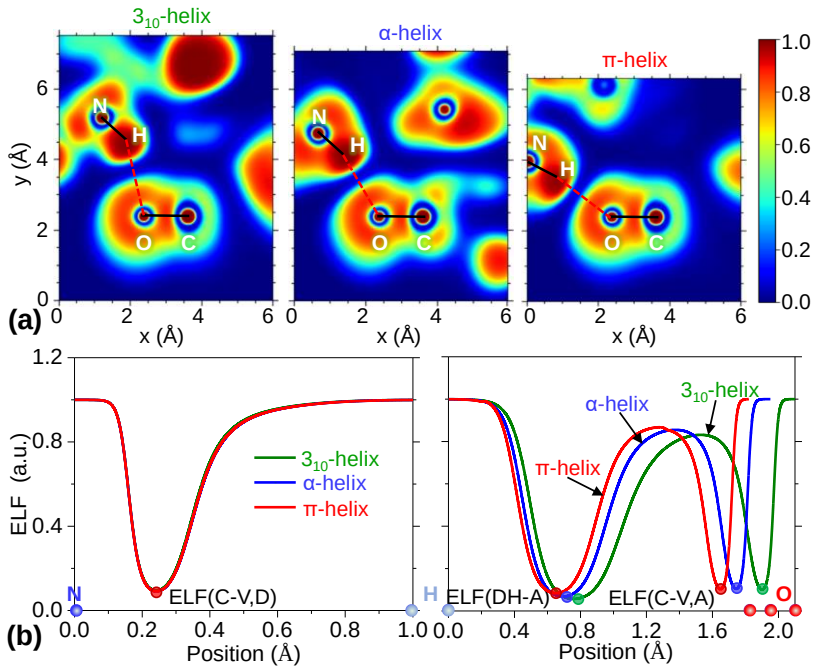

Figure 4.4. (a) Normalized electron density for the three isomer helices in the vicinity of four atoms forming the H-bond. (b) The electron localization function (ELF) distributions along the N−H covalent bond and the H···O H-bond. Local minimum of these curves define ELF(C−V, D), ELF(DH···A), and ELF(C−V, A). Spheres on the horizontal axis indicate atomic locations.

4.4.5 H-bonding Strength

Given the structure-governed thermal transport mechanisms discovered above, the H-bonding as a structural linker of helices is important to the energy transport processes. For quantitative understanding, the H-bonding is analyzed using two DFT-based methods, namely, the core-valence bifurcation index (CVBI) and the H-bond energy. Provided by equilibrium MD simulations, the initial structures of helices were intercepted into minimum sizes that each contains a H-bond (with four residues for the 3_{10}-helix, five for the α-helix, and six for the π-helix), as shown in **Figure C.4**. The structures were geometrically optimized by DFT, feeding wave functions into subsequent H-bond analyses.

Figure 4.4a plots normalized electron density ranging from 0 to 1 for the three helices in the vicinity of four atoms forming the H-bond which include N (donor), H, O (acceptor), and C. Due to the different H-bond connectivities, geometry of the H-bond varies in the isomer helices despite the same type of H-bond in nature. Two important measures of a H-bond, i.e. the H-bond length (H···O) and the H-bond angle (N−H···O) are found to be 2.12Å and 21.36°, 1.96 Å and 17.33°, and 1.83 Å and 15.69° for the 3_{10}-, α-, π-helices, respectively. **Figure 4.4**b further plots the ELF distributions along the N−H covalent bond and the H···O H-bond, respectively, for the three helices. Their (3,−1) critical points are identified as the local minimum. Interestingly, while both ELF(C−V, D) and ELF(C−V, A) are close among the helices (variations < 4.32% and < 3.54%, respectively), ELF(D−H, A) as one of the most important quantities of H-bonding is found to vary significantly, i.e. 0.057 for the 3_{10}-helix, 0.0681 for the α-helix and 0.0839 for the π-helix. Based on the ELF values, CVBI is calculated to be 0.0378, 0.0226 and 0.0071 for

the 3_{10}-, α-, π-helices, respectively. On the one hand, the positive CVBIs indicate that the H-bonds in all helices under investigation are primarily of the electrostatic nature. On the other hand, the π-helix is found to have the lowest CVBI, suggesting the strongest H-bond among the three isomers.

Further, the H-bond energy is evaluated based on the QTAIM theory using the electron density at the H-bond critical point (ρ_{BCP}). ρ_{BCP} is found to increase from 0.0176 to 0.0235 and 0.0341 for the 3_{10}-, α- and π-helices, respectively. The H-bond energy is the strongest in the π-helix with -6.86 Kcal mol^{-1}, followed by the α-helix with -4.50 Kcal mol^{-1} and the 3_{10}-helix with -3.18 Kcal mol^{-1}. The results of H-bond energy agree well with the CVBI results. Importantly, the isomer helices demonstrate different H-bond strengths despite the same type of H-bond in nature, which contribute directly to the differences in energy transport mechanisms and the overall thermal conductivities as revealed in previous sections.

4.5 Conclusions

To summarize, this work provides a novel perspective on vibrational energy transport in proteins by studying three isomer helices. The isomers are specially designed to have the same simplest all-Glycine amino acid sequence interlocked by different H-bond networks representing three important types of helices that widely exist in proteins as building blocks. This design allows for an in-depth analysis of the role of H-bond connectivity on the thermal conductivity and associated phonon transport mechanisms, while neglecting other factors including the amino acid sequence and side chains. The MD simulation predicts that the π-helix has the highest thermal conductivity of 19.54 W m^{-1} K^{-}

[1] in the diffusive limit, which is 109.88% higher than that of the α-helix and 207.23% higher than that of the 3_{10}-helix. The thermal conductivities are highly length-dependent in the ballistic-to-diffusive transition regime, with a phonon mean free path of about 140-160 nm. The important contributions made by the H-bond to energy transport is underpinned by transport mechanisms including phonon spectral energy density, dispersion, mode-specific transport, group velocity, and relaxation time. The three acoustic branches together account for about 57.7-60% of the overall thermal conductivity, in which the LA branch contributes about two thirds. Additionally, semi-optical branches in the 5-10 THz range also contribute about 30.3-31.3%. The different H-bond connectivities cause an increase in group velocities and a blueshift in key frequencies defining the group velocity from the 3_{10}-helix to the π-helix. The unique H-bond connectivity in the π-helix also raises the phonon relaxation time indicating lower phonon scattering. Particularly, the LA branch diverges from the relationship of $\tau \propto f^{-1.77}$ at small wave vectors indicating predominant Normal scattering. Finally, calculations based on DFT and QTAIM reveal that the π-helix has the strongest H-bonds among the isomers, despite the fact that all these H-bonds are of the same type. The stronger H-bonds in the π-helix, together with the unique helical structure enabled by its H-bond connectivity, reduce scattering and increase group velocities of low-frequency acoustic and semi-optical phonons, drastically enhancing energy transport. The insights provided by this study not only enrich the fundamental understanding of energy transport in proteins, but may also stimulate a rational design of helical molecular structures with configurable H-bond networks to enable new energy transport mechanisms and desired thermal properties.

4.6 Acknowledgments

This work is financially supported by CAREER Award No. CBET-1751610 from the National Science Foundation. This research made use Idaho National Laboratory computing resources which are supported by the Office of Nuclear Energy of the U.S. Department of Energy and the Nuclear Science User Facilities under Contract No. DE-AC07-05ID14517

REFERENCES

[1] Kukura, P., McCamant, D. W., Yoon, S., Wandschneider, D. B., and Mathies, R. A., 2005, "Structural Observation of the Primary Isomerization in Vision with Femtosecond-Stimulated Raman," Science, 310(5750), p. 1006.

[2] Champion, P. M., 2005, "Following the Flow of Energy in Biomolecules," Science, 310(5750), p. 980.

[3] Engel, G. S., Calhoun, T. R., Read, E. L., Ahn, T.-K., Mančal, T., Cheng, Y.-C., Blankenship, R. E., and Fleming, G. R., 2007, "Evidence for wavelike energy transfer through quantum coherence in photosynthetic systems," Nature, 446(7137), pp. 782-786.

[4] Miller, R. J. D., 1991, "Vibrational Energy Relaxation and Structural Dynamics of Heme Proteins," Annu. Rev. Phys. Chem., 42(1), pp. 581-614.

[5] Mülhaupt, R., 2013, "Green Polymer Chemistry and Bio-based Plastics: Dreams and Reality," Macromol. Chem. Phys., 214(2), pp. 159-174.

[6] Leitner, D. M., 2008, "Energy Flow in Proteins," Annu. Rev. Phys. Chem., 59(1), pp. 233-259.

[7] Gather, M. C., and Yun, S. H., 2014, "Bio-optimized energy transfer in densely packed fluorescent protein enables near-maximal luminescence and solid-state lasers," Nat. Commun., 5(1), p. 5722.

[8] Davydov, A. S., 1977, "Solitons and energy transfer along protein molecules," J. Theor. Biol., 66(2), pp. 379-387.

[9] Li, G., Magana, D., and Dyer, R. B., 2014, "Anisotropic energy flow and allosteric ligand binding in albumin," Nat. Commun., 5(1), p. 3100.

[10] Sagnella, D. E., and Straub, J. E., 2001, "Directed Energy “Funneling" Mechanism for Heme Cooling Following Ligand Photolysis or Direct Excitation in Solvated Carbonmonoxy Myoglobin," J. Phys. Chem. B, 105(29), pp. 7057-7063.

[11] Backus, E. H. G., Nguyen, P. H., Botan, V., Moretto, A., Crisma, M., Toniolo, C., Zerbe, O., Stock, G., and Hamm, P., 2008, "Structural Flexibility of a Helical Peptide Regulates Vibrational Energy Transport Properties," J. Phys. Chem. B, 112(48), pp. 15487-15492.

[12] Zhang, L., Chen, T., Ban, H., and Liu, L., 2014, "Hydrogen bonding-assisted thermal conduction in β-sheet crystals of spider silk protein," Nanoscale, 6(14), pp. 7786-7791.

[13] Zhang, L., Bai, Z., Ban, H., and Liu, L., 2015, "Effects of the amino acid sequence on thermal conduction through β-sheet crystals of natural silk protein," PCCP, 17(43), pp. 29007-29013.

[14] Lee, H. S., and Zhang, Y., 2012, "BSP-SLIM: A blind low-resolution ligand-protein docking approach using predicted protein structures," Proteins Struct. Funct. Bioinf., 80(1), pp. 93-110.

[15] Ota, N., and Agard, D. A., 2005, "Intramolecular Signaling Pathways Revealed by Modeling Anisotropic Thermal Diffusion," J. Mol. Biol., 351(2), pp. 345-354.

[16] Liu, J., Tawa, G. J., and Wallqvist, A., 2013, "Identifying Cytochrome P450 Functional Networks and Their Allosteric Regulatory Elements," PLoS ONE, 8(12), p. e81980.

[17] Seldeen, K., Deegan, B., Bhat, V., Mikles, D., McDonald, C., and Farooq, A., 2011, "Energetic Coupling Along an Allosteric Communication Channel Drives the Binding of Jun-Fos Heterodimeric Transcription Factor to DNA," The FEBS journal, 278, pp. 2090-2104.

[18] Laine, E., Auclair, C., and Tchertanov, L., 2012, "Allosteric Communication across the Native and Mutated KIT Receptor Tyrosine Kinase," PLoS Comput. Biol., 8(8), p. e1002661.

[19] Kong, H., Xia, K., Ren, N., Cui, Y., Liu, R., Li, Q., Lv, M., Shi, J., Yan, Q., Cui, Z., Fan, C., Zhu, Y., and Wang, L., 2018, "Serum protein corona-responsive autophagy tuning in cells," Nanoscale, 10(37), pp. 18055-18063.

[20] Ma, H., O'Donnel, E., and Tian, Z., 2018, "Tunable thermal conductivity of π-conjugated two-dimensional polymers," Nanoscale, 10(29), pp. 13924-13929.

[21] Pace, C., Scholtz, J. M., and Grimsley, G., 2014, "Forces Stabilizing Proteins," FEBS Lett., 588.

[22] Li, P., Chen, H., Schott, J. A., Li, B., Zheng, Y., Mahurin, S. M., Jiang, D.-e., Cui, G., Hu, X., Wang, Y., Li, L., and Dai, S., 2019, "Porous liquid zeolites: hydrogen bonding-stabilized H-ZSM-5 in branched ionic liquids," Nanoscale, 11(4), pp. 1515-1519.

[23] Ash, E. L., Sudmeier, J. L., De Fabo, E. C., and Bachovchin, W. W., 1997, "A Low-Barrier Hydrogen Bond in the Catalytic Triad of Serine Proteases? Theory Versus Experiment," Science, 278(5340), p. 1128.

[24] Miño, G., and Contreras, R., 2010, "Non-electrostatic components of short and strong hydrogen bonds induced by compression inside fullerenes," Chem. Phys. Lett., 486(4), pp. 119-122.

[25] Foster, W., Miyazawa, K., Fukuma, T., Kusumaatmaja, H., and Voïtchovsky, K., 2020, "Self-assembly of small molecules at hydrophobic interfaces using group effect," Nanoscale, 12(9), pp. 5452-5463.

[26] Seo, S., Lee, K., Min, M., Cho, Y., Kim, M., and Lee, H., 2017, "A molecular approach to an electrocatalytic hydrogen evolution reaction on single-layer graphene," Nanoscale, 9(11), pp. 3969-3979.

[27] Han, J., Shen, Y., and Feng, W., 2016, "Using multiple hydrogen bonding cross-linkers to access reversibly responsive three dimensional graphene oxide architecture," Nanoscale, 8(29), pp. 14139-14145.

[28] Huang, H., Hu, Y., Zhang, J., Sato, H., Zhang, H., Noda, I., and Ozaki, Y., 2005, "Miscibility and Hydrogen-Bonding Interactions in Biodegradable Polymer Blends of Poly(3-hydroxybutyrate) and a Partially Hydrolyzed Poly(vinyl alcohol)," J. Phys. Chem. B, 109(41), pp. 19175-19183.

[29] Vieira-Pires, R., and Morais-Cabral, J., 2010, "3(10) Helices in channels and other membrane proteins," J Gen Physiol, 136, pp. 585-592.

[30] Levitt, M., and Chothia, C., 1976, "Structural patterns in globular proteins," Nature, 261(5561), pp. 552-558.

[31] Cooley, R., Arp, D., and Karplus, P., 2010, "Evolutionary Origin of a Secondary Structure: α-Helices as Cryptic but Widespread Insertional Variations of α-Helices That Enhance Protein Functionality," J. Mol. Biol., 404, pp. 232-246.

[32] Berman, H., Henrick, K., and Nakamura, H., 2003, "Announcing the worldwide Protein Data Bank," Nat. Struct. Mol. Biol., 10(12), pp. 980-980.

[33] Berman, H., Henrick, K., Nakamura, H., and Markley, J. L., 2006, "The worldwide Protein Data Bank (wwPDB): ensuring a single, uniform archive of PDB data," Nucleic Acids Res., 35(suppl_1), pp. D301-D303.

[34] ww, P. D. B. c., 2018, "Protein Data Bank: the single global archive for 3D macromolecular structure data," Nucleic Acids Res., 47(D1), pp. D520-D528.

[35] Plimpton, S., 1995, "Fast Parallel Algorithms for Short-Range Molecular Dynamics," J. Comput. Phys., 117(1), pp. 1-19.

[36] MacKerell, A. D., Bashford, D., Bellott, M., Dunbrack, R. L., Evanseck, J. D., Field, M. J., Fischer, S., Gao, J., Guo, H., Ha, S., Joseph-McCarthy, D., Kuchnir, L., Kuczera, K., Lau, F. T. K., Mattos, C., Michnick, S., Ngo, T., Nguyen, D. T., Prodhom, B., Reiher, W. E., Roux, B., Schlenkrich, M., Smith, J. C., Stote, R., Straub, J., Watanabe, M., Wiórkiewicz-Kuczera, J., Yin, D., and Karplus, M., 1998, "All-Atom Empirical Potential for Molecular Modeling and Dynamics Studies of Proteins," J. Phys. Chem. B, 102(18), pp. 3586-3616.

[37] Goicochea, J., Madrid, M., and Amon, C., 2010, "Thermal Properties for Bulk Silicon Based on the Determination of Relaxation Times Using Molecular Dynamics," J. Heat Transfer, 132, p. 012401.

[38] Thomas, J. A., Turney, J. E., Iutzi, R. M., Amon, C. H., and McGaughey, A. J. H., 2010, "Predicting phonon dispersion relations and lifetimes from the spectral energy density," Phys. Rev. B, 81(8), p. 081411.

[39] de Koker, N., 2009, "Thermal Conductivity of MgO Periclase from Equilibrium First Principles Molecular Dynamics," Phys. Rev. Lett., 103(12), p. 125902.

[40] Shiomi, J., and Maruyama, S., 2006, "Non-Fourier heat conduction in a single-walled carbon nanotube: Classical molecular dynamics simulations," Phys. Rev. B, 73(20), p. 205420.

[41] McGaughey, A. J. H., and Kaviany, M., 2004, "Quantitative validation of the Boltzmann transport equation phonon thermal conductivity model under the single-mode relaxation time approximation," Phys. Rev. B, 69(9), p. 094303.

[42] Donadio, D., and Galli, G., 2009, "Atomistic Simulations of Heat Transport in Silicon Nanowires," Phys. Rev. Lett., 102(19), p. 195901.

[43] Dove, M. T., 1993, Introduction to Lattice Dynamics, Cambridge University Press, Cambridge.

[44] Rudin, W., 1987, Real and complex analysis, 3rd ed, McGraw-Hill, Inc.

[45] Turney, J. E., Landry, E. S., McGaughey, A. J. H., and Amon, C. H., 2009, "Predicting phonon properties and thermal conductivity from anharmonic lattice dynamics calculations and molecular dynamics simulations," Phys. Rev. B, 79(6), p. 064301.

[46] Srivastava, G., 2019, The Physics of Phonons.

[47] Frisch, M. J., Trucks, G. W., Schlegel, H. B., Scuseria, G. E., Robb, M. A., Cheeseman, J. R., Scalmani, G., Barone, V., Petersson, G. A., Nakatsuji, H., Li, X., Caricato, M., Marenich, A. V., Bloino, J., Janesko, B. G., Gomperts, R., Mennucci, B., Hratchian, H. P., Ortiz, J. V., Izmaylov, A. F., Sonnenberg, J. L., Williams, Ding, F., Lipparini, F., Egidi, F., Goings, J., Peng, B., Petrone, A., Henderson, T., Ranasinghe, D., Zakrzewski, V. G., Gao, J., Rega, N., Zheng, G., Liang, W., Hada, M., Ehara, M., Toyota, K., Fukuda, R., Hasegawa, J., Ishida, M., Nakajima, T., Honda, Y., Kitao, O., Nakai, H., Vreven, T., Throssell, K., Montgomery Jr., J. A., Peralta, J. E., Ogliaro, F., Bearpark, M. J., Heyd, J. J., Brothers, E. N., Kudin, K. N., Staroverov, V. N., Keith, T. A., Kobayashi, R., Normand, J., Raghavachari, K., Rendell, A. P., Burant, J. C., Iyengar, S. S., Tomasi, J., Cossi, M., Millam, J. M., Klene, M., Adamo, C., Cammi, R., Ochterski, J. W., Martin, R. L., Morokuma, K., Farkas, O., Foresman, J. B., and Fox, D. J., 2016, "Gaussian 16 Rev. C.01,"Wallingford, CT.

[48] Goerigk, L., and Grimme, S., 2011, "Efficient and Accurate Double-Hybrid-Meta-GGA Density Functionals—Evaluation with the Extended GMTKN30 Database for General Main Group Thermochemistry, Kinetics, and Noncovalent Interactions," J. Chem. Theory Comput., 7(2), pp. 291-309.

[49] Weigend, F., and Ahlrichs, R., 2005, "Balanced basis sets of split valence, triple zeta valence and quadruple zeta valence quality for H to Rn: Design and assessment of accuracy," PCCP, 7(18), pp. 3297-3305.

[50] Zheng, J., Xu, X., and Truhlar, D., 2011, "Minimally augmented Karlsruhe basis sets," Theor. Chem. Acc., 128, pp. 295-305.

[51] Becke, A. D., and Edgecombe, K. E., 1990, "A simple measure of electron localization in atomic and molecular systems," J. Chem. Phys, 92(9), pp. 5397-5403.

[52] Lu, T., and Chen, F., 2011, "Meaning and Functional Form of the Electron Localization Function," Acta Phys. Chim. Sin., 27, p. 2786.

[53] Fuster, F., and Silvi, B., 2000, "Does the topological approach characterize the hydrogen bond?," Theor. Chem. Acc., 104(1), pp. 13-21.

[54] Alikhani, M. E., Fuster, F., and Silvi, B., 2005, "What Can Tell the Topological Analysis of ELF on Hydrogen Bonding?," Struct. Chem., 16(3), pp. 203-210.

[55] Nikolaienko, T. Y., Bulavin, L. A., and Hovorun, D. M., 2012, "Bridging QTAIM with vibrational spectroscopy: the energy of intramolecular hydrogen bonds in DNA-related biomolecules," PCCP, 14(20), pp. 7441-7447.

[56] Brovarets, O. h., Yurenko, Y., and Hovorun, D., 2014, "The significant role of the intermolecular CH···O/N hydrogen bonds in governing the biologically important pairs of the DNA and RNA modified bases: A comprehensive theoretical investigation," J. Biomol. Struct. Dyn., 32, pp. 1-29.

[57] Ayoub, Ahmed T., Craddock, Travis J. A., Klobukowski, M., and Tuszynski, J., 2014, "Analysis of the Strength of Interfacial Hydrogen Bonds between Tubulin Dimers Using Quantum Theory of Atoms in Molecules," Biophys. J., 107(3), pp. 740-750.

[58] Emamian, S., Lu, T., Kruse, H., and Emamian, H., 2019, "Exploring Nature and Predicting Strength of Hydrogen Bonds: A Correlation Analysis Between Atoms-in-Molecules Descriptors, Binding Energies, and Energy Components of Symmetry-Adapted Perturbation Theory," J. Comput. Chem., 40(32), pp. 2868-2881.

[59] Afonin, A. V., Vashchenko, A. V., and Sigalov, M. V., 2016, "Estimating the energy of intramolecular hydrogen bonds from 1H NMR and QTAIM calculations," Org. Biomol. Chem., 14(47), pp. 11199-11211.

[60] Lu, T., and Chen, F., 2012, "Multiwfn: A multifunctional wavefunction analyzer," J. Comput. Chem., 33(5), pp. 580-592.

[61] Zhou, Y., Zhang, X., and Hu, M., 2015, "Quantitatively analyzing phonon spectral contribution of thermal conductivity based on nonequilibrium molecular dynamics simulations. I. From space Fourier transform," Phys. Rev. B, 92(19), p. 195204.

[62] Aiyiti, A., Hu, S., Wang, C., Xi, Q., Cheng, Z., Xia, M., Ma, Y., Wu, J., Guo, J., Wang, Q., Zhou, J., Chen, J., Xu, X., and Li, B., 2018, "Thermal conductivity of suspended few-layer MoS2," Nanoscale, 10(6), pp. 2727-2734.

[63] Klemens, P. G., and Simon, F. E., 1951, "The thermal conductivity of dielectric solids at low temperatures (Theoretical)," Proc R Soc Lond A, Math Phys Sci, 208(1092), pp. 108-133.

[64] Wang, X., Kaviany, M., and Huang, B., 2017, "Phonon coupling and transport in individual polyethylene chains: a comparison study with the bulk crystal," Nanoscale, 9(45), pp. 18022-18031.

CHAPTER 5

TUNING THERMAL TRANSPORT OF HELICAL PROTEIN NANOTUBES THROUGH SIDE-CHAIN MASS MODIFICATION

5.1 Abstract

Fibrous proteins have been widely used for various materials due to their biocompatibility, high flexibility and preeminent mechanical properties. With the development of bioelectronics technologies and cutting-edge flexible materials, biocompatible materials with higher or lower thermal conductivities are in high demand. Decoding thermal transport mechanisms of proteins may guide a rational design of biomaterials with desired functionality and tunable thermal properties. Here, using non-equilibrium molecular dynamics simulation, we investigate that side-chain mass plays an important role in thermal transport through the protein α-helix. α-helix with four representative residues, i.e. G, A, L and P, are shown to have distinct thermal conductivities due to their different side-chain masses. Results suggest that heavy side-chain mass hinders heat conduction. Phonon analysis further identifies side-chain mass as the major contributor to this phenomenon, which affects properties of low-frequency acoustic and semi-optical phonons. The understanding provides fundamental insights to guide the design and engineering of protein-based biomaterials for desired thermal properties.

He, J., Zhang, L., and Liu, L., "Tuning Thermal Transport of Helical Protein Nanotudes through Side-Chain Mass Modification." (To be submitted)

5.2 Introduction

Biopolymers are long-chain molecules comprised by repeating units, which widely exist in nature. In general, biopolymers can be divided into three types on the basis of their components: proteins, polysaccharides and nucleic acids. In addition to biomedical applications, biopolymers, particularly proteins, are extensively used for green applications, which reduce the production of substances detrimental to plants, animals, environment and humans [1]. Therefore, protein-based materials may be an excellent candidate to supersede engineering materials for thermal applications. Proteins, like molecular machines, cannot function without energy transport that propagates conformational changes and removes excess heat. For instance, consider a folding protein that undergoes a conformational transition to a lower energy state: on one hand, this conformational transition may be facilitated by local conformational rearrangement, which is directly associated with energy transport; and on the other hand, to obtain its lower energy state, excess energy needs to be efficiently removed. This fundamental process links the structural and dynamical features of proteins to their functioning in energy transport [2]. Therefore, studying thermal transport mechanisms and the influencing factors in biomolecules is an important step for understanding, and potentially controlling, protein dynamics and functioning [3].

The interplay between protein structures and functionality has been discussed for several decades. Particularly, energy transfer is also related to secondary structure motifs such as the α-helix and β-sheet, both of which are stabilized by H-bonds. For example, α-helix is the most abundant protein secondary structures, which widely exist in globular proteins. The α-helices often span the whole protein, giving rise to the speculation that they

actually transfer vibrational energy through the biomacromolecule. So far a large amount of efforts have been made for studying heat transfer in proteins and its relation to protein dynamics [4-9], such as peptide helices [10], β-sheets [6], heme cofactors [7], and functionalized materials [11, 12]. Results indicate that energy flow usually propagates through covalent backbone along the structures [8, 12], and also spreads through weaker interactions such as H-bonds [6, 11]. In addition, solvent can also play a fundamental role in energy diffusion [8], such as in the Ca^{2+} ATPase through proteins [4, 9], in PDZ-2 domain within surface proteins [13] and in hemoglobin between protein subunits [14]. But despite all of these results, it is still unclear that how heat is conducted in α-helix structures. In structural biology, the α-helices with different side-chain masses may have different mechanical properties. However, the effects of side-chain mass on thermal conduction in proteins have rarely been discussed. Exploring side-chain mass dependent thermal properties of proteins may improve the basic understanding of nanoscale thermal transport in protein-based biomaterials. Results cannot only further guide a rational design of protein-based biomaterials with desired thermal properties, but is also expected to be extensively used in many fields such as biomedical and sustainable materials industry in the future.

To better understand the effects of side-chain mass on thermal transport in the α-helix protein, it is essential to discuss the similarities and differences in thermal transport mechanisms between α-helix protein and other low-dimensional nanomaterials. Firstly, α-helix features numerous side chains, such as -H, $-CH_3$, $-CH_2CH(CH_3)_2$ and $–CH_2(C_6H_5)$ that are bonded with C_α atom of polypeptide chain backbone $(-N-C_\alpha-C-)$, which is analogous to carbon nanotubes modified by functional groups and single-stranded carbon

chain polymer modified by atomic mass. Secondly, the α-helix with different side chains is also similar to superlattice nanowires with alternating atoms along the lattice direction. Based on previous studies, carbon nanotubes modified by functional groups [15, 16] have reduced phonon mean free path, leading to lower thermal conductivities in comparison with pristine carbon nanotubes. Thermal conductivity of single-stranded carbon chain polymer modified by atomic mass [17] is lower than that of pristine polymer chain due to the redshift of phonon bands. Due to phonon scattering at interfaces [18], doped superlattice nanowires usually have lower thermal conductivities than pure nanowires. It is hypothesized that thermal conduction in the α-helix is analogous to these structures.

In this work, to explore thermal transport mechanisms modified by the side-chain mass, α-helices with four different side chains including G, A, L and P are discussed. Using molecular dynamic simulation combined with phonon dynamic analysis such as dispersion curves, mode-dependent thermal conductivity, relaxation time, group velocity and vibrational density of state, we will show in detail phonon properties and molecular mechanisms through which side-chain mass affects thermal conduction. This study may expand our understanding of how side-chain mass affects thermal conduction in the α-helix, and guide the design of protein-based materials that has many applications in the green and sustainable materials industry.

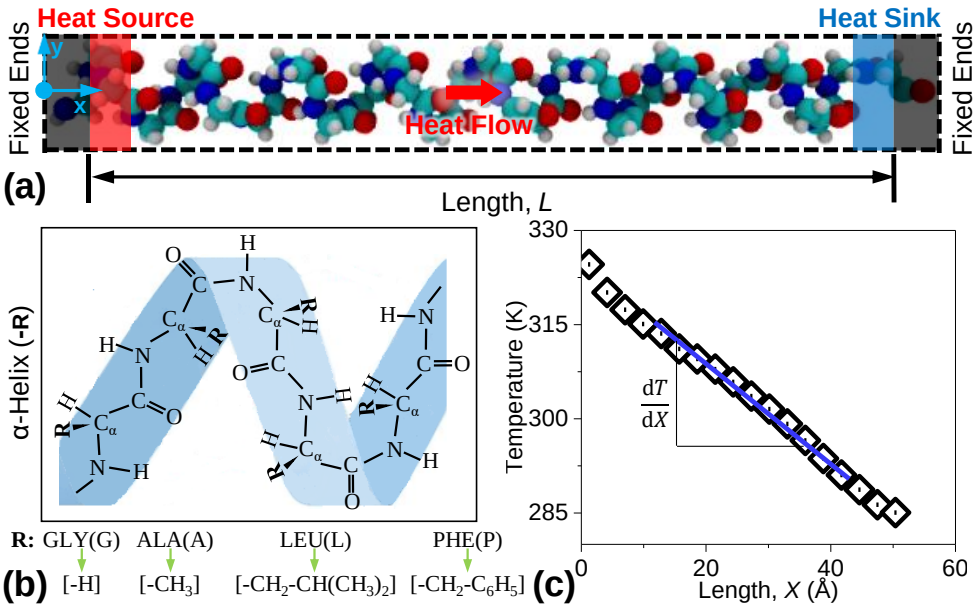

Figure 5.1. (a) Simulation setup for NEMD to calculate thermal conductivity of α-helix. Heat flux is produced by adding energies into heat source (red region) and subtracting the same amount from heat sink (blue region). *L* is the simulation length. Periodic boundary conditions are implemented on three directions. (b) α-helix protein feature repeats by R residue, where R denotes molecular configuration of G, A, L and P residue. (c) Temperature profile obtained from NEMD simulation.

5.3 Models and Methods

5.3.1 Models

In this study, α-helix is selected as the main focus because it constitutes the largest class of protein secondary structures and plays a major role in mediating protein-protein interactions. To quantify side-chain mass effects, α-helices with different side-chain masses are constructed to perform thermal analysis at the atomic level. **Figure 5.1**a illustrates a simulation model of α-helix that comprises 32 repeat units of the glycine amino acid on the side chain. As shown in **Figure 5.1**b, each residue consists of three backbone atoms (-N-C_α-C-) and serval side chain/atoms including a side group (R), an oxygen atom

(O), a hydrogen atom (H) bonded with a nitrogen atom (N), and another hydrogen atom (H) bonded to α-carbon atom (C_α). Here, four side-chain groups are considering including glycine (GLY/G: -H), alanine (ALA/A: -CH_3), leucine (LEU/L: -$CH_2CH(CH_3)$), and phenylalanine (PHE/P: -CH_2-C_6H_5). To eliminate phonon scattering on boundaries, periodic boundary conditions are applied to three directions. The lateral sizes are large (60 nm) to prevent periodic images of the α-helix protein from interacting with each other along both *y* and *z* direction.

5.3.2 Molecular Dynamics (MD)

All atomic simulations in this work are performed using LAMMPS [19]. CHARMM22 force field [20] is employed for describing interatomic interactions, which has been verified by previous studies to be the most efficient force field to describe peptides and proteins. The particle-particle particle-mesh method (PPPM) is used to describe the long-range Coulomb's interactions with a root mean square accuracy of 10^{-6}. Prior to simulating thermal conduction, initial molecular configurations are first optimized, and then relaxed by energy minimization with the conjugate gradient method, followed by equilibrium MD under the NVT ensemble with the Nose-Hoover thermostat at 300K for 10 ns with a time step of 0.25 fs. Heat flux is imposed by the Langevin thermostats under the NVE ensemble. The system is simulated for 20 ns to reach the steady state, and another 10 ns to obtain thermal conductivities by averaging the temperature gradient and heat flow. Global angular momentum is zeroed out at every step to eliminate possible global rotations.

5.3.3 Thermal Conductivity Calculations

Nonequlibrium molecular dynamics (NEMD) is employed for calculating thermal conductivity of α-helices with different side-chain mass. For example, a simulation system of α-helix with the G residue is shown in **Figure 5.1**a. To avoid the entropic state, atoms within one slab at each end are fixed as the heat insulation. Although forces acting on the two ends may induce tensile stresses, a previous study have indicated that such effects on thermal conduction can be ignored [21]. To produce a temperature gradient, the temperature of two regions next to the insulation walls are fixed using the Langevin thermostat, 325 K for the heat source and 285 K for the heat sink. Energies (ΔE) are added to the heat source and subtracted from the heat sink with the same amount, which are recorded to calculate heat flux (J) using $J = \Delta E/A\Delta t$, where A is the effective cross sectional area and Δt is time step. When steady state is reached, thermal conductivity is calculated using $k = J/(\mathrm{d}T/\mathrm{d}x)$, where k is the thermal conductivity and $\mathrm{d}T/\mathrm{d}X$ is the temperature gradient, which is obtained by fitting the linear region displayed in **Figure 5.1**c.

5.3.4 Phonon Spectral Energy Density

PSED analysis is employed to directly predict phonon properties such as dispersion relation, relaxation time, group velocities and mode-based thermal conductivity [22-24]. Importantly, this approach takes atomic velocities from MD simulation as an input parameter, which inherently includes phonon-phonon scattering, inharmonic effects, and normal and Umklapp scattering [25]. To obtain PSED, the smallest atomic group that characterizes the helical structure is defined as the unit cell, and each helical model has several unit cells along the heat flux direction. With Parseval's theorem and lattice dynamic

[26, 27], atomic trajectories in the real space are projected onto normal vibration modes in the frequency space, $q\left(\begin{matrix}\boldsymbol{\kappa}\\ \nu\end{matrix};t\right)$. Here, $\boldsymbol{\kappa}$ denotes the wave vector, ν is phonon branch and t is time. PSED is obtained by averaging the contribution made by all atoms to the amplitude of normal modes, i.e.

$$\Phi(\boldsymbol{\kappa},\omega)=\frac{1}{4\pi\tau_0 N_T}\sum_{\alpha}\sum_{j}^{N_A}m_j\left|\int_0^{\tau_0}\sum_{l}^{N_T}\dot{u}_{\alpha}\left(\begin{matrix}l\\ j\end{matrix};t\right)\times\exp\left[i\boldsymbol{\kappa}\cdot\boldsymbol{r_0}\left(\begin{matrix}l\\ 0\end{matrix}\right)-i\omega t\right]dt\right|^2 \qquad (5.1)$$

Here, $\Phi(\boldsymbol{\kappa},\omega)$ denotes PSED as a function of $\boldsymbol{\kappa}$ and angular frequency ω, N_T is the overall number of unit cells, N_A is the total number of atom in an unit cell, τ_0 is the simulation time, m_j is the j-th atomic mass, $\dot{u}_{\alpha}\left(\begin{matrix}l\\ j\end{matrix};t\right)$ is the j-th atomtic velocity in the l-th unit cell at simulation time t along the α-th direction, and $\boldsymbol{r_0}\left(\begin{matrix}l\\ 0\end{matrix}\right)$ resprents the equilibrium postion of the l-th unit cell. The wave vector of one-dimensional systems is defined as $\kappa_x=2\pi n_x/a_x N_T$, where a_x is length of the unit cell along the *x*-direction, and n_x is an integer ranging from 0 to N_T-1. Then, κ_x can be mapped into $N_x/2$ points ranging from 0 to π/a_x, which corresponds to the first Brillouin zone from Γ to K point. In this work, atomic velocities are reported from MD simulations under the NVE ensemble at 298 K, with an integral time of τ_0 = 1 ns.

5.3.5 Phonon Dispersion

Based on the PSED, dispersion curves are obtained by discerning peaks of phonon branches and fitting these peaks into continuous curves along the wave vector direction. In general, dispersion curve is a function of frequency ($f=\omega/2\pi$, in the unit of THz) and the reduced wave vector ($\xi=\kappa_x/(2\pi/a_x)$, dimensionless). In this work, the obtained dispersion curves have a resolution of 0.001 THz $\times$ 0.01.

5.3.6 Phonon Density of States

To further evaluate effects of side-chain mass on thermal transport, PDOS is also performed to reveal thermal transport mechanisms, which is calculated by Fourier transformation of velocity autocorrelation function (VACF) for the selected or all atoms following the expression

$$\mathrm{PDOS}(\omega) = \frac{1}{\sqrt{2\pi}} \int_0^{+\infty} \mathrm{e}^{-i\omega t} \frac{\langle v(t) \cdot v(0) \rangle}{\langle v(0) \cdot v(0) \rangle} \, dt \tag{5.2}$$

where PDOS is a function of angular frequency ω, $v(t)$ denotes the atomic velocity, and $\langle \cdot \rangle$ describes an average over those selected atoms.

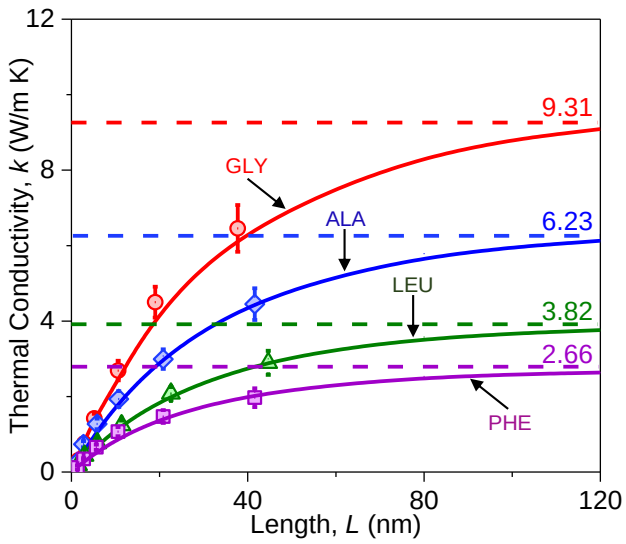

Figure 5.2. Thermal conductivity of α-helix with different residue as a function of their lengths. Simulation results for α-helix with each residue are fitted by an empirical function having two parameters, L_c and $k_{x,\infty}$. Dashed lines represent the thermal conductivity in the diffusive limit.

5.4 Results and Discussion

5.4.1 Thermal Conductivity

Figure 5.2 plots thermal conductivities as a function of the length of α-helices with four side chains including G, A, L and P. When the length is varied up to 40 nm, the calculated thermal conductivity of poly-G α-helix increases from 0.31 to 6.46 W m^{-1} K^{-1} (red circles in **Figure 5.2**). Similarly, α-helices with A, L and P residue show the same ascending trend. Thermal conductivity of the poly-A α-helix increases from 0.26 to 4.45 W m^{-1} K^{-1} (blue circles), and that of the poly-L α-helix increases from 0.19 to 2.89 W m^{-1} K^{-1} (green circles), while that of the poly-A α-helix increases from 0.12 to 1.97 W m^{-1} K^{-1} (purple circles). Energy carriers, i.e. phonons, cannot be fully relaxed in the short helical segments in proteins and their thermal transport is limited by the geometry. Since low-frequency phonons usually travel several orders of magnitude longer than high-frequency phonons, thermal conductivity in the diffusion limit cannot be predicted by the popular Matthiessen rule [28, 29] due to the nonlinear relationship between $1/k_x$ and $1/L$. Alternatively, $k_x = k_{x,\infty}\left(1 - e^{-L/L_c}\right)$ [30] is employed to quantify the length effect and to describe the transition from ballistic to diffusive phonon transport. Here, L is the length, $k_{x,\infty}$ denotes thermal conductivity when L is infinite, and L_c is the characteristic length that describes ballistic-to-diffusive transition. Besides, an effective mean free path for fully diffusive phonon transport is defined as $L_{0.99}$, i.e. $\kappa_x|_{L=L_{0.99}} = 0.99\kappa_{x,\infty}$, such that $L_{0.99} \equiv \ln(100)L_c = 4.605L_c$. $k_{x,\infty}$ is calculated to be 9.31 W m^{-1} K^{-1} for the poly-G α-helix, 6.23 W m^{-1} K^{-1} for the poly-A α-helix, 3.82 W m^{-1} K^{-1} for the poly-L α-helix, and 2.66 W m^{-1} K^{-1} for the poly-P α-helix. The effective mean free path $L_{0.99}$ is found to

be about 148.1 nm, 141.8 nm, 133.8 nm and 121.2 nm for the α-helices with G, A, L and P residues, respectively. More importantly, **Figure 5.2** illustrates the prominent side-chain mass effects. Results show that the poly-G α-helix gives the highest thermal conductivity among the four α-helices under investigation, poly-A the second, poly-L the third, and poly-P the lowest. When phonon transport is fully diffusive, $k_{x,\infty}$ of the poly-G α-helix is 49.44% higher than that of poly-A, 143.72% higher than that of poly-L, and 250.00% higher than that of poly-P. Results indicate that higher side-chain mass dramatically hinders thermal conduction in the α-helix.

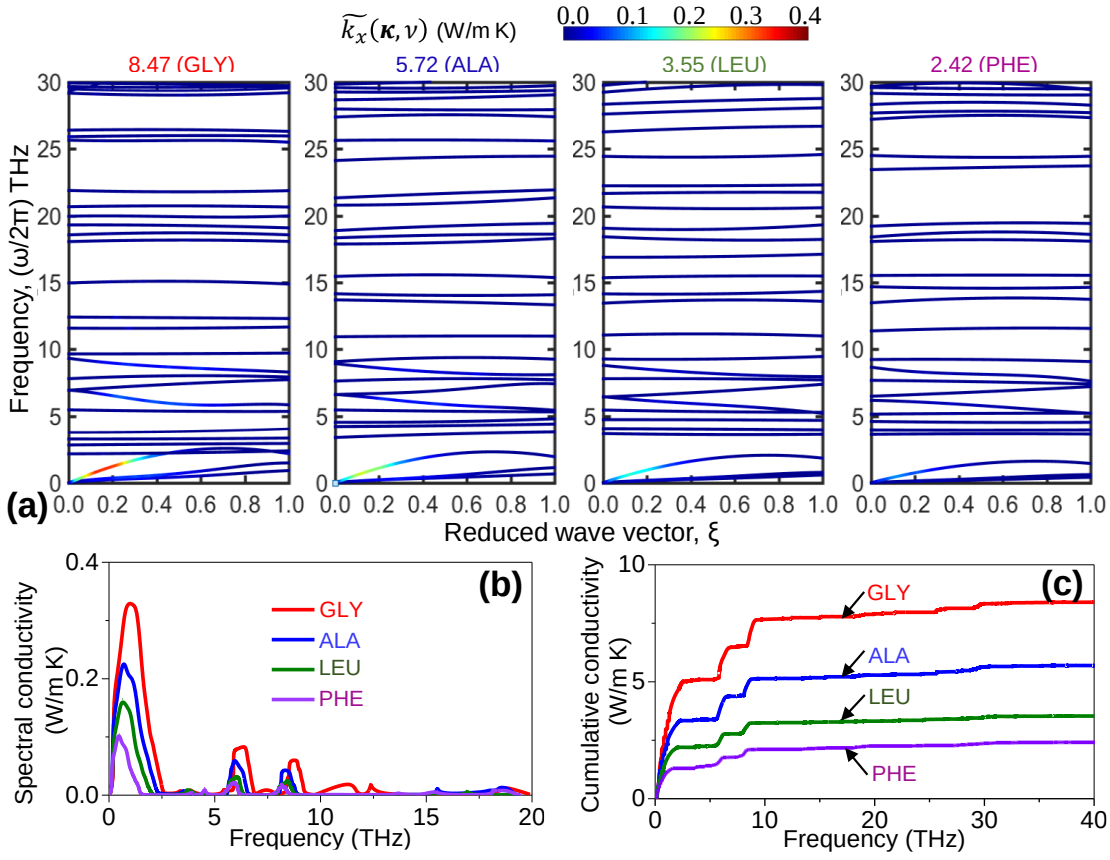

Figure 5.3. Phonon dispersion relations of α-helix with G (red), A (blue), L (green) and P (purple) residue in the first Brillouin zone. Colors denote mode-by-mode contribution to thermal conductivity, i.e. $\widetilde{k_x}(\boldsymbol{\kappa},\nu)$. (b) Spectral and (c) cumulative thermal conductivity of α-helix with different residue.

5.4.2 Mode-Specific Thermal Conductivity

To elucidate the role of side-chain mass in thermal transport mechanisms, phonon properties are further examined by PSED. Using Boltzmann transport equation [31], together with phonon relaxation time approximation [32], the total thermal conductivity can be expressed as $k_x = \sum_{\boldsymbol{\kappa}} \sum_{\nu} \widetilde{k_x}(\boldsymbol{\kappa}, \nu)$. Here, $\widetilde{k_x}(\boldsymbol{\kappa}, \nu)$ denotes the thermal conductivity of each phonon mode, namely, mode-based thermal conductivity, which is described as $\widetilde{k_x}(\boldsymbol{\kappa}, \nu) = c_{ph} v_{g,x}^2(\boldsymbol{\kappa}, \nu) \tau(\boldsymbol{\kappa}, \nu)$, where ν is the phonon branch, $v_{g,x}(\boldsymbol{\kappa}, \nu)$ is phonon group velocity, c_{ph} is the volumetric specific heat, and $\tau(\boldsymbol{\kappa}, \nu)$ is relaxation time. In a classic system, $c_{ph} = k_B/V$, where k_B is the Boltzmann constant and V is system volume.

Phonon vibrational properties are exhibited in **Figure 5.3**a, which describe the dispersion relations of α-helices with G, A, L, and P residues from left to right. The regime with frequency > 30 THz is not displayed. Phonons with higher frequencies are always related to stronger localized interactions, so they have lower group velocities, shorter relaxation times and little contributions to thermal conduction. All α-helices have three lowest-lying acoustic phonon branches, namely two transverse branches (TA1 and TA2) and one longitudinal branch (LA). The two TA branches feature nearly linear dispersion curves, and the LA branch is almost quadratic. Among the three acoustic branches, slope of the LA branch is the largest, TA1 is the second and TA2 is the smallest. In addition to the three acoustic branches, most optical branches practically have a slope of zero indicating little contribution to thermal transport, and some optical branches have a non-zero slope particularly in the frequency range of 5-10 THz. Importantly, by comparing α-helices with G, A, L, and P residue, the three acoustic branches are dramatically softened

when the side-chain mass increases from the G residue to the P residue, indicating that the higher mass slows down heat transfer and decreases the thermal conductivity. For example, the peak frequency within TA1 is reduced from 0.92, 0.67, 0.59 to 0.42 THz, and that within TA2 is reduced from 1.33, 1.14, 0.79 to 0.62 THz, while the change within LA is more pronounced, dropping from 2.19, 1.96, 1.85 to 1.45 THz.

Based on the PSED analysis, **Figure 5.3**a uses line colors to visualize the mode-based thermal conductivity for specific wave vectors and frequencies, i.e. $\widetilde{k_x}(\boldsymbol{\kappa}, \nu)$. The contribution made by each phonon branch can be obtained by summing up the mode-based thermal conductivity $\widetilde{k_x}(\boldsymbol{\kappa}, \nu)$ of specific wave vectors and frequencies. Contributions made by the LA branch is calculated to be 3.26, 2.17, 1.53 and 0.97 W m^{-1} K^{-1} for the α-helices with G, A, L and P residues, respectively, which accounts for about 40% of the overall thermal conductivities. The TA1 branch contributes 0.63, 0.42, 0.26 and 0.15 W m^{-1} K^{-1}, respectively, representing about 12% of the overall thermal conductivities. The TA2 branch contributes 1.07, 0.76, 0.40 and 0.23 W m^{-1} K^{-1}, respectively, about 7% of the overall thermal conductivities. Obviously, the LA branch makes the greatest contribution to thermal conduction, followed by TA2 and TA1. The three acoustic branches together contribute about 60.00% of the overall thermal conductivities for all α-helices under investigation, indicating that acoustic phonons dominate the heat transfer processes.

In addition, some optical branches also have a major contribution to thermal transport as defined by their values of $\widetilde{k_x}(\boldsymbol{\kappa}, \nu)$. In view of the mode-based thermal conductivity as shown in **Figure 5.3**b, semi-optical branches in the frequency range of 5-10 THz contribute about 30.35%, 24.95%, 26.52% and 24.91% to the overall thermal

conductivities of α-helices with G, A, L and P residue, respectively. By comparison, high-frequency phonons with the frequency > 20 THz make very little contributions, i.e. 0.53, 0.43, 0.23 and 0.15 W m^{-1} K^{-1} which account for only 6.29%, 7.51%, 6.39% and 6.32% to the overall thermal conductivities. This result is in excellent agreement with the understanding that high-frequency optical phonons do not contribute considerably to thermal conduction due to their short relaxation times and low group velocities. However, we still cannot ignore them since they also play an important role in thermal transport by serving as phonon scattering channels for lower-frequency phonons. **Figure 5.3**c further indicates that, within the frequency ranges of acoustic and low-frequency semi-optical phonons, the cumulative thermal conductivity of all α-helices increases and converges after 20 THz. Hence, acoustic phonons and low-frequency semi-optical phonons dominate energy transfer in α-helices with different side chains. Together, they contribute about 90% of the overall thermal conductivities. Increased side-chain mass dramatically lowers the thermal conductivity by adversely affecting acoustic and low-frequency semi-optical phonons.

Importantly, thermal conductivities obtained by MD simulation shown in **Figure 5.2** can also be verified by the mode-based thermal conductivity results following $k_x = \sum_{\boldsymbol{\kappa}} \sum_{\nu} \widetilde{k_x}(\boldsymbol{\kappa}, \nu)$, which sums up contributions from all phonon modes. By this approach, the total thermal conductivity is calculated to be 8.47 W m^{-1} K^{-1}, 5.72 W m^{-1} K^{-1}, 3.55 W m^{-1} K^{-1} and 2.42 W m^{-1} K^{-1} for the four α-helices, respectively, in good agreement with that predicted by using the nonequilibrium MD simulation.

5.4.3 Phonon Group Velocity

It is well known that the phonon group velocity is an important parameter to characterize phonons. Based on the dispersion curves, group velocities of key branches (TA1, TA2, LA and two selected optical branches) are evaluated by $v_{g,x}(\boldsymbol{\kappa}, \nu) = \partial\omega/\partial\kappa_x$ and plotted in **Figure 5.4** for the α-helices. By comparison, it can be seen clearly that LA branch has the highest group velocity, followed by TA2 and TA1. Besides, group velocities of the two selected optical phonon branches are comparable with that of TA1 and TA2.

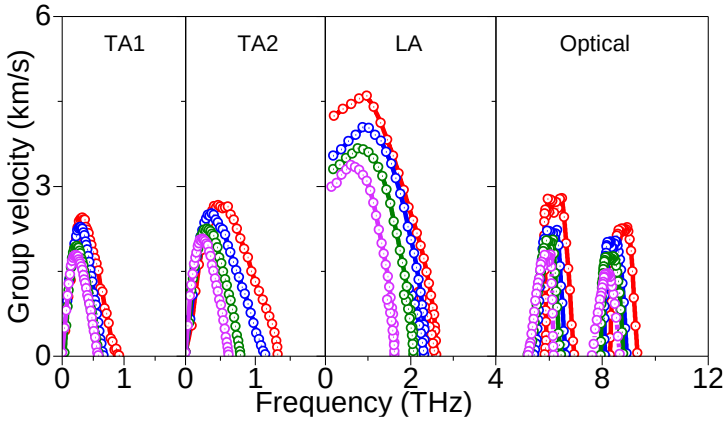

Figure 5.4. Frequency-dependent group velocities for those key phonon branches, such as TA1, TA2, LA and two selected optical branches, primarily contributed to their thermal conductivities in *α*-helix with G (red), A (blue), L (green) and P (purple) residue.

Importantly, α-helices with different residues show strong side-chain mass effects on group velocities. On one hand, the poly-G α-helix has the highest group velocity in all of the key branches, followed by the poly-A, poly-L, and poly-P α-helices. These findings agree well with the ranking of their overall thermal conductivities. On the other hand, a "redshift" is identified as a result of the side chain variation. That is, the increased side-chain mass lowers the group velocity of acoustic and low-frequency semi-optical phonons, leading to reduced thermal conductivities. For instance, the frequency that corresponds to

the peak group velocity of the LA branch, is found to redshift from 0.97 THz for the poly-G α-helix to 0.87 THz for the poly-A α-helix, then to 0.76 THz for the poly-L α-helix, and finally to 0.60 THz for the poly-P α-helix. The same trend is found in other acoustic and important optical phonon modes.

5.4.4 Phonon Relaxation Time

Relaxation time is another important quantity that characterizes thermal transport. To obtain the relaxation time, PSED results are first reconstructed to have a particular form in terms of the relaxation time, i.e. $\Phi(\boldsymbol{\kappa}, f) = \sum_{\nu}^{3n} C(\boldsymbol{\kappa}, \nu)/([4\pi\tau(\boldsymbol{\kappa}, \nu)(f - f_0(\boldsymbol{\kappa}, \nu))]^2 + 1)$, where n is the total atom number, $3n$ denotes the total number of phonon branches, $C(\boldsymbol{\kappa}, \nu)$ is a mode-dependent magnitude, $\tau(\boldsymbol{\kappa}, \nu)$ is the relaxation time, f is the phonon frequency and $f_0(\boldsymbol{\kappa}, \nu)$ denotes the frequency where PSED has a local peak. Following each wave number, $\boldsymbol{\kappa}$, the PSED data can be described as $3n$ single-variable data points with the independent variable of frequency, f. Then the data points are fitted by multiple Lorentzian functions, $\Phi = I/(1 + [(f - f_c)/\gamma]^2)$, near the local peaks. Here, f_c denotes the frequency at the peak center, I is the peak magnitude, and γ is the half-width at the half-maximum. Then, the regenerated PSED function at a specified wave vector can be defined as a superposition of the Lorentzian functions of all phonon branches. Relaxation time for all phonon modes, $\tau(\boldsymbol{\kappa}, \nu)$, can be evaluated by using the parameters of Lorentzian functions.

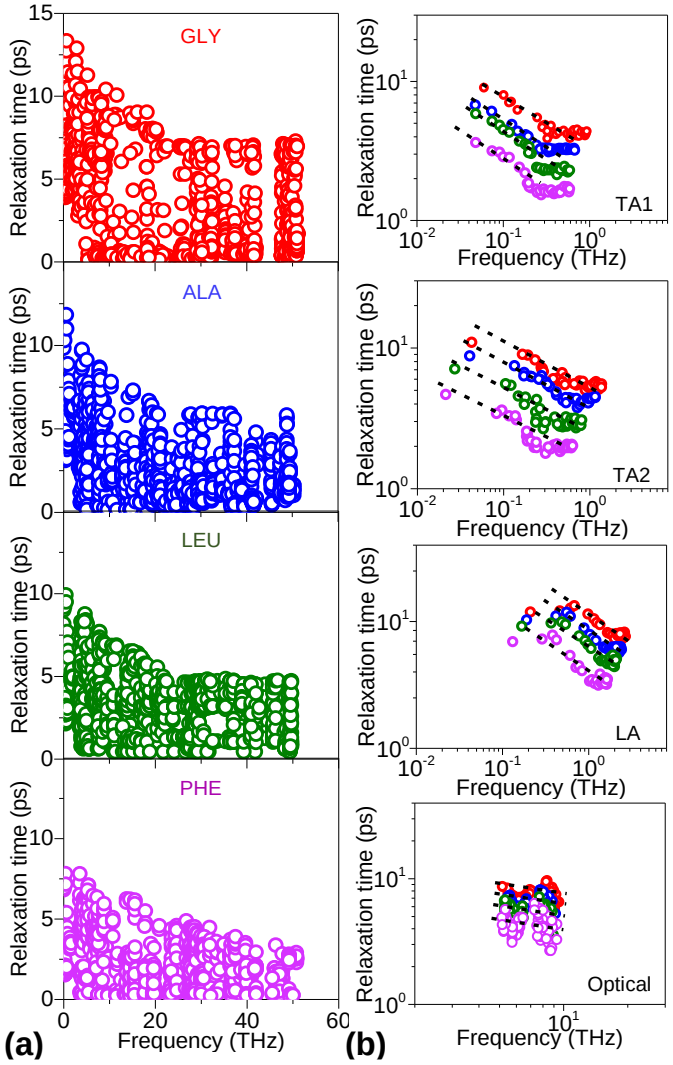

Figure 5.5. (a) Frequency-dependent phonon relaxation times for α-helix with G, A, L and P residue. (b) Relaxation time for those key branches contributed to their thermal conductivities, including three acoustic and two selected optical branches of α-helix with G (red), A (blue), L (green) and P (purple) residue. Back dashed lines show the relationship of between relaxation time and frequency.

Using the above approach, frequency-dependent relaxation time of all phonon modes for the α-helices with G, A, L and P residue in the first Brillouin zone is plotted in **Figure 5.5**a. Phonon-phonon scattering is found to be influenced by the side-chain mass. On one hand, within the low-frequency range, relaxation time has an obvious decrease with

the increase of f where most heat is carried by phonons. The largest τ in this range is found to be about 13.98 ps, 11.83 ps, 9.94 ps and 7.82 ps for the α-helices with G, A, L and P residues, respectively. On the other hand, τ is always below a threshold in the high-frequency regime, which indicates that relaxation time is frequency-independent. The threshold is about 7.04 ps, 5.93 ps, 4.71 ps and 3.92 ps for the four α-helices, respectively. By comparison, relaxation time also shows different upper limits as a result of the different side-chain masses. The poly-G α-helix has the longest τ, and the poly-P α-helix has the shortest τ. The increased side-chain mass causes more phonon scattering within the helical structures.

To further explore the side-chain mass effects, **Figure 5.5**b plots the frequency-dependent phonon relaxation time for key branches including the three acoustic branches and two selected semi-optical branches. All of these branches are situated in the low-frequency range, showing a linear relationship between $\log(\tau)$ and $\log(f)$. In addition, among these key branches, τ of the three acoustic branches show obvious frequency-dependent correlations. With the increase of f, τ monotonously decreases indicating increased phonon scattering. For the α-helices with G, A, L and P residues, the LA branch has the highest rate of descendance, followed by the two transverse acoustic branches, and then the two semi-optical branches. When the residue changes from G, A, L to P in the α-helix, **Figure 5.5**b shows that the increase of side-chain mass reduces the relaxation time for all key branches, which further lowers the thermal conductivity.

5.4.5 Phonon Density of States

The poly-G α-helix is found to have the highest thermal conductivity than its counterparts with A, L and P residues. To understand how side-chain mass affects thermal transport, we further perform PDOS analysis on the α-helices with G, A, L and P residues, as shown in **Figure 5.6**. Although the helices are identical except the different side chains, they show distinct phonon modes across the whole frequency range.

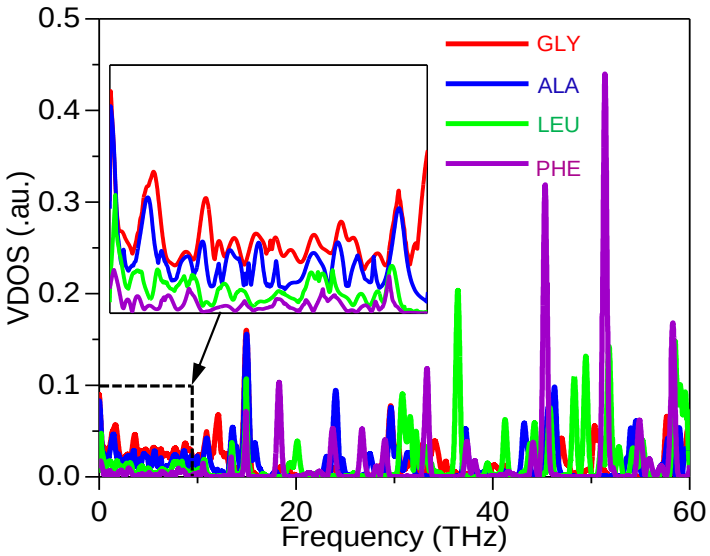

Figure 5.6. Phonon DOS of *α*-helix with different residue including G, A, L and P residue. The inset plots the phonon spectra in the frequency range from 0 to 10 THz.

Within the frequency of 0 to 10 THz, the α-helix with G residues has the highest PDOS, followed by the α-helices with A, L and P residues, indicating that the vibration of phonons is weakened with the increased side-chain mass within the low-frequency range. However, when the frequency exceeds 10 THz, the α-helix with P residues has a higher PDOS at some frequency regions, followed by the α-helices with L, A, and G residues, indicating that the increased side-chain mass can strengthen the local vibration of phonons.

For instance, the highest PDOS reaches 0.44 at 51.42 THz for the poly-P α-helix, 0.20 at 36.44 THz for the poly-L α-helix, 0.09 at 46.36 THz for the poly-A α-helix, while only 0.04 at 46.54 THz for the poly-G α-helix. Based on these findings, phonon dynamics is distinct among the α-helices due to their different side-chain masses. When phonons carry heat through the α-helix, the increased side-chain mass can weaken the vibration of phonons within the low-frequency range, significantly decreasing thermal conduction. Besides, despite the local vibration of phonons can be strengthened with the increase of side-chain mass at high-frequency region, it contributes little to thermal conduction.

5.5 Conclusion

To summarize, thermal conduction mechanisms in four representative α-helices with G, A, L and P residues are studied to reveal the intrinsic side-chain mass effects. The α-helix is shown to have length-dependent thermal conductivities. With the same length, thermal conductivity of the α-helix is found to decrease with increasing side-chain mass, demonstrating negative contribution of side-chain mass to heat transfer. When phonon transport is fully diffusive, the poly-G α-helix has the highest thermal conductivity among the four, i.e. 9.31 W m^{-1} K^{-1}, 49.44% higher than the ploy-A α-helix, 143.72% higher than the ploy-L α-helix, and 250.00% higher than the ploy-P α-helix. These different thermal conductivities are caused by the residues having different masses and unique phonon properties. Phonon dynamic analysis using the spectral energy density is performed to obtain the dispersion relations, mode-based thermal conductivity, cumulative thermal conductivity, relaxation time, group velocity, and vibration density of states. These results all indicate that the side-chain mass affects the properties of low-frequency acoustic

phonons and semi-optical phonons, leading distinct thermal transport behaviors. These findings suggest that the α-helix can be engineered to produce functional biomaterials with tunable thermal performance.

REFERENCES

[1] Mülhaupt, R., 2013, "Green Polymer Chemistry and Bio-based Plastics: Dreams and Reality," Macromol. Chem. Phys., 214(2), pp. 159-174.

[2] Leitner, D. M., 2001, "Vibrational Energy Transfer in Helices," Phys. Rev. Lett., 87(18), p. 188102.

[3] Fujisaki, H., and Straub, J., 2005, "Vibrational energy relaxation in proteins," PNAS, 102, pp. 6726-6731.

[4] Lervik, A., Bresme, F., Kjelstrup, S., Bedeaux, D., and Rubi, J., 2010, "Heat transfer in protein–water interfaces," Physical chemistry chemical physics : PCCP, 12, pp. 1610-1617.

[5] Helbing, J., Devereux, M., Nienhaus, K., Nienhaus, G. U., Hamm, P., and Meuwly, M., 2012, "Temperature Dependence of the Heat Diffusivity of Proteins," J. Phys. Chem. A, 116(11), pp. 2620-2628.

[6] Zhang, L., Chen, T., Ban, H., and Liu, L., 2014, "Hydrogen bonding-assisted thermal conduction in ??-sheet crystals of spider silk protein," Nanoscale, 6.

[7] Sagnella, D. E., and Straub, J. E., 2001, "Directed Energy “Funneling" Mechanism for Heme Cooling Following Ligand Photolysis or Direct Excitation in Solvated Carbonmonoxy Myoglobin," J. Phys. Chem. B, 105(29), pp. 7057-7063.

[8] Botan, V., Backus, E., Pfister, R., Moretto, A., Crisma, M., Toniolo, C., Nguyen, P., Stock, G., and Hamm, P., 2007, "Energy transport in peptide helices," PNAS, 104, pp. 12749-12754.

[9] Kjelstrup, S., Rubi, J., and Bedeaux, D., 2005, "Energy dissipation in slipping biological pumps," Physical chemistry chemical physics : PCCP, 7, pp. 4009-4018.

[10] Botan, V., Backus, E. H. G., Pfister, R., Moretto, A., Crisma, M., Toniolo, C., Nguyen, P. H., Stock, G., and Hamm, P., 2007, "Energy transport in peptide helices," Proceedings of the National Academy of Sciences, 104(31), p. 12749.

[11] Schoen, P., Michel, B., Curioni, A., and Poulikakos, D., 2009, "Hydrogen-bond enhanced thermal energy transport at functionalized, hydrophobic and hydrophilic silica-water interfaces," Chem. Phys. Lett., 476.

[12] Lin, Z., and Rubtsov, I., 2012, "Constant-speed vibrational signaling along polyethyleneglycol chain up to 60-A distance," PNAS, 109, pp. 1413-1418.

[13] Stucki-Buchli, B., Waldauer, S., Walser, R., Donten, M., Pfister, R., Blöchliger, N., Steiner, S., Caflisch, A., Zerbe, O., and Hamm, P., 2013, "Kinetic response of a photoperturbed allosteric protein," PNAS, 110.

[14] Gnanasekaran, R., Agbo, J. K., and Leitner, D. M., 2011, "Communication maps computed for homodimeric hemoglobin: Computational study of water-mediated energy transport in proteins," J. Chem. Phys, 135(6), p. 065103.

[15] Padgett, C. W., and Brenner, D. W., 2004, "Influence of Chemisorption on the Thermal Conductivity of Single-Wall Carbon Nanotubes," Nano Lett., 4(6), pp. 1051-1053.

[16] Pan, R., Xu, Z., Zhu, Z., and Wang, Z., 2007, "Thermal conductivity of functionalized single-wall carbon nanotubes," Nanotechnology, 18(28), p. 285704.

[17] Liao, Q., Zeng, L., Liu, Z., and Liu, W., 2016, "Tailoring Thermal Conductivity of Single-stranded Carbon-chain Polymers through Atomic Mass Modification," Sci. Rep., 6, p. 34999.

[18] Hu, M., and Poulikakos, D., 2012, "Si/Ge Superlattice Nanowires with Ultralow Thermal Conductivity," Nano Lett., 12(11), pp. 5487-5494.

[19] Plimpton, S., 1995, "Fast Parallel Algorithms for Short-Range Molecular Dynamics," Journal of Computational Physics, 117(1), pp. 1-19.

[20] MacKerell, A. D., Bashford, D., Bellott, M., Dunbrack, R. L., Evanseck, J. D., Field, M. J., Fischer, S., Gao, J., Guo, H., Ha, S., Joseph-McCarthy, D., Kuchnir, L., Kuczera, K., Lau, F. T. K., Mattos, C., Michnick, S., Ngo, T., Nguyen, D. T., Prodhom, B., Reiher, W. E., Roux, B., Schlenkrich, M., Smith, J. C., Stote, R., Straub, J., Watanabe, M., Wiórkiewicz-Kuczera, J., Yin, D., and Karplus, M., 1998, "All-Atom Empirical Potential for Molecular Modeling and Dynamics Studies of Proteins," J. Phys. Chem. B, 102(18), pp. 3586-3616.

[21] Liu, J., and Yang, R., 2010, "Tuning the thermal conductivity of polymers with mechanical strains," Physical Review B, 81(17), p. 174122.

[22] Thomas, J. A., Turney, J. E., Iutzi, R. M., Amon, C. H., and McGaughey, A. J. H., 2010, "Predicting phonon dispersion relations and lifetimes from the spectral energy density," Physical Review B, 81(8), p. 081411.

[23] de Koker, N., 2009, "Thermal Conductivity of MgO Periclase from Equilibrium First Principles Molecular Dynamics," Phys. Rev. Lett., 103(12), p. 125902.

[24] Shiomi, J., and Maruyama, S., 2006, "Non-Fourier heat conduction in a single-walled carbon nanotube: Classical molecular dynamics simulations," Phys. Rev. B, 73(20), p. 205420.

[25] Bao, H., Qiu, B., Zhang, Y., and Ruan, X., 2012, "A first-principles molecular dynamics approach for predicting optical phonon lifetimes and far-infrared reflectance of polar materials," Journal of Quantitative Spectroscopy and Radiative Transfer, 113(13), pp. 1683-1688.

[26] Dove, M. T., 1993, Introduction to Lattice Dynamics, Cambridge University Press, Cambridge.

[27] Rudin, W., 1987, Real and complex analysis, 3rd ed, McGraw-Hill, Inc.

[28] Schelling, P. K., Phillpot, S. R., and Keblinski, P., 2002, "Comparison of atomic-level simulation methods for computing thermal conductivity," Physical Review B, 65(14), p. 144306.

[29] Ziman, J. M., 2001, Electrons and Phonons: The Theory of Transport Phenomena in Solids, OUP Oxford.

[30] Thomas, J. A., Iutzi, R. M., and McGaughey, A. J. H., 2010, "Thermal conductivity and phonon transport in empty and water-filled carbon nanotubes," Phys. Rev. B, 81(4), p. 045413.

[31] Turney, J. E., Landry, E. S., McGaughey, A. J. H., and Amon, C. H., 2009, "Predicting phonon properties and thermal conductivity from anharmonic lattice dynamics calculations and molecular dynamics simulations," Phys. Rev. B, 79(6), p. 064301.

[32] Srivastava, G., 2019, The Physics of Phonons.

CHAPTER 6

CONCLUSIONS AND FUTURE WORK

This dissertation mainly focuses on how hydrogen bonds guide thermal transport in helical protein nanostructures, and interfacial heat transfer across two dissimilar materials. To address these issues, two representative material systems including protein secondary structures and the functionalized electrode/electrolyte interface in solid-state Li ion batteries are demonstrated. Heat flow is conducted along protein chains in the former case, and is conducted normal to the interface in the latter case. Results from both cases indicate that hydrogen bonds improve thermal transport.

To investigate the role of hydrogen bonds in interfacial thermal conduction between the electrode and electrolyte, thermal properties of electrode are first explored. Molecular dynamics in combination with thermal resistance models are employed for understanding thermal transport in monocrystalline $LiCoO_2$ and polycrystalline $LiCoO_2$ and across its grain boundaries. The monocrystalline $LiCoO_2$ shows anisotropic thermal conductivities in the order of 100 W m^{-1} K^{-1}, with the lowest along the direction where the lithium layers and the cobalt oxide layers alternate. The thermal conductivity also decreases with the increased temperature. By comparison, polycrystalline $LiCoO_2$ is more isotropic with much lower thermal conductivities. The difference between monocrystalline and polycrystalline is caused by thermal resistance of grain boundaries, and size-dependent intra-grain thermal conductivities that are unique to polycrystals. The grain boundary thermal conductance is calculated to be in the range of 7.16 - 25.21 GW m^{-2} K^{-1}, which is dominated by the tilt angel and grain size. Further, the size effects of intra-grain thermal

conductivities are investigated by two thermal resistance models. The insights revealed by the findings may facilitate future efforts of battery materials design for improving thermal management.

Fast heat removal is highly desired in Li ion batteries but it is seriously obstructed by high thermal resistance across the electrode/electrolyte interface. To address this issue, SAMs are used as the vibrational mediator to tune interfacial thermal conductance between an electrode, LCO, and a solid state electrolyte, PEO. Embedded at the LCO/PEO interface, SAMs are specially designed to form hierarchical H-bond network with PEO. Dictated by molecular design, the interface between LCO and PEO displays markedly different thermal conductance which has strong implications for heat removal and thermal management. H-bonded interfaces between LCO and PEO show a strongest enhancement in the LCO surface functionalized by PAA, followed by PAM and PVA, over the pristine interface. By comparison, LCO surface functionalized by PE which is a non-H-bonded interface enhances thermal conduction least. Apparently, the unique hierarchical H-bond network carried by SAMs is a primary contributor to the significantly improved thermal conduction across LCO/PEO interfaces. The contribution strongly depends on the type, location and density of H-bonds. In addition, even though multiple types of H-bonds coexist in each system, the primary H-bond, which almost accounts for about 80% of all H-bonds at the interface, largely determines the adhesion energy and thermal conductance across LCO/PEO interfaces. Importantly, all SAM-decorated interfaces are shown to have: (1) alleviated some discontinuities in the temperature field, (2) stand-up configurations with extended chains, and (3) enhanced coupling of vibrational modes. They synergistically

improve interfacial thermal transport, in which H-bonds play a positive role. The results are expected to improve fundamental understanding and applications of H-bonded interface engineering for improved thermal management of multi-material systems including the lithium-ion batteries.

To study the role of hydrogen bonds in helical protein nanostructures, three representative α-helices are analyzed including the 3_{10}-helix, α-helix and π-helix. There helices are specially designed to have the same simplest all-Glycine amino acid sequence interlocked by different H-bond networks that widely exist in proteins as building blocks. This design allows for an in-depth analysis of the role of H-bond configuration on the thermal transport mechanisms, while neglecting other factors including amino acid sequence and side chains. MD simulation shows that π-helix has the highest thermal conductivity in the diffusive limit, which is 109.88% higher than that of α-helix and 207.23% higher than that of 3_{10}-helix. Then, contributions made by the H-bond to heat transfer is underpinned by transport mechanisms including spectral energy density, dispersion, mode-specific transport, group velocity, and relaxation time. The three acoustic branches together account for about 60% of the overall thermal conductivity, in which LA branch contributes about two thirds. Additionally, semi-optical branches in the 5-10 THz range also contribute about 30 %. The different H-bond configurations cause an increase in group velocities and a blueshift in key frequencies defining the group velocity from 3_{10}-helix to π-helix. The unique H-bond connectivity in the π-helix also raises the relaxation time indicating lower scattering. Particularly, the LA branch diverges from the relationship of $\tau \propto f^{-1.77}$ at small wave vectors indicating predominant Normal scattering. Finally, calculations based

on DFT and QTAIM indicate that π-helix has the strongest H-bonds, despite the fact that all these H-bonds are of the same type. The insights not only enrich the fundamental understanding of energy transport in proteins, but may also stimulate a rational design of helical molecular structures with configurable H-bond networks to enable new energy transport mechanisms and desired thermal properties.

To comprehensively understand thermal transport mechanisms in helical proteins, it is important to explore the effects of side-chain mass on heat transfer. To this end, α-helices with four side-chain types such as G, A, L and P residues are studied. The α-helix is shown to have length-dependent thermal conductivities. With the same length, thermal conductivity of the α-helix is found to decrease with increasing side-chain mass, demonstrating negative contribution of side-chain mass to heat transfer. When phonon transport is fully diffusive, the poly-G α-helix has the highest thermal conductivity among the four, i.e. 9.31 W m^{-1} K^{-1}, 49.44% higher than the ploy-A α-helix, 143.72% higher than the ploy-L α-helix, and 250.00% higher than the ploy-P α-helix. These different thermal conductivities are caused by the residues having different masses and unique phonon properties. Phonon dynamic analysis using the spectral energy density is performed to obtain the dispersion relations, mode-based thermal conductivity, cumulative thermal conductivity, relaxation time, group velocity, and vibration density of states. These results all indicate that the side-chain mass affects the properties of low-frequency acoustic phonons and semi-optical phonons, leading distinct thermal transport behaviors. These findings suggest that the α-helix can be engineered to produce functional biomaterials with tunable thermal performance.

Despite numerous efforts have been taken to study the role of hydrogen bonds in thermal conduction, there are still many topics expected to be studied further. For example, the effect of hydrogen bonds configuration on the interfacial thermal conductance between two dissimilar materials; the effect of hydrogen bonds strength on heat transfer along intra- or inter-chain polymers; the effect of hydrogen bonds types on thermal transport of different materials; the effect of geometry of hydrogen bonds on thermal transport, such as one-center, two-center, three-center and four-center hydrogen bonds. Insights from these essential studies may provide a reasonable guide to advance hydrogen-bonding conductive materials for the required thermal properties.

APPENDICES

APPENDIX A

SUPPLEMENTAL MATERIAL OF CHAPTER 2

APPENDIX B

SUPPLEMENTAL MATERIAL OF CHAPTER 3

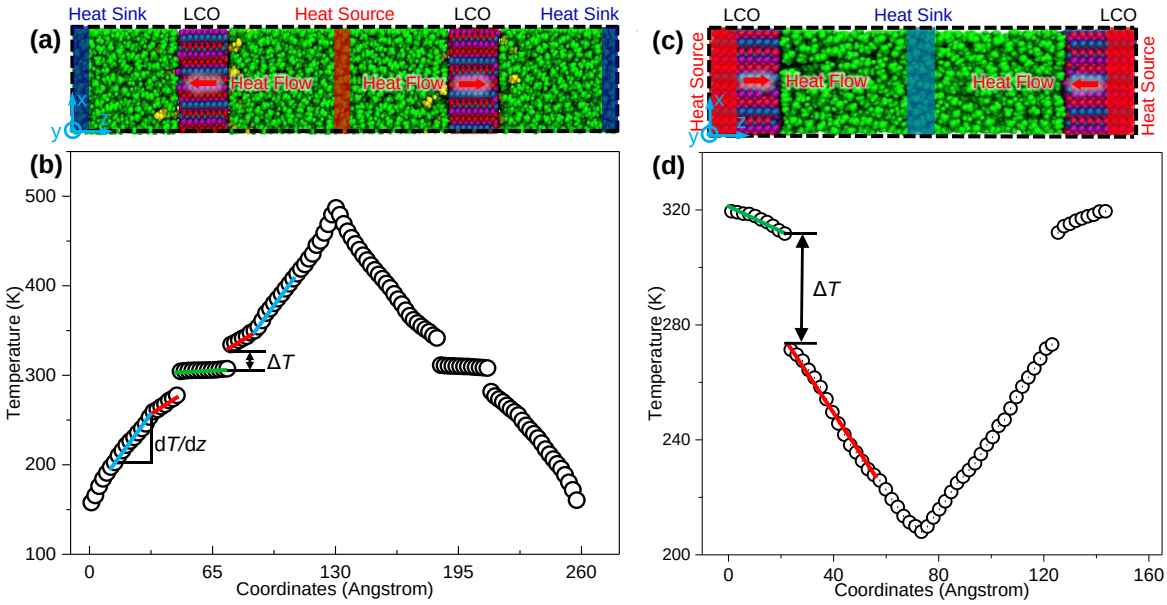

Figure B.1. (a) A simulation system for RNEMD calculation and (b) the associated temperature profile. Δ*T* is the temperature drop across an LCO/PEO interface, and d*T*/dz represents the temperature gradient within PEO. (c) A simulation system for NEMD calculation and (d) the associated temperature profile, where the heat source and the heat sink are fixed at 320 K and 210 K, respectively.

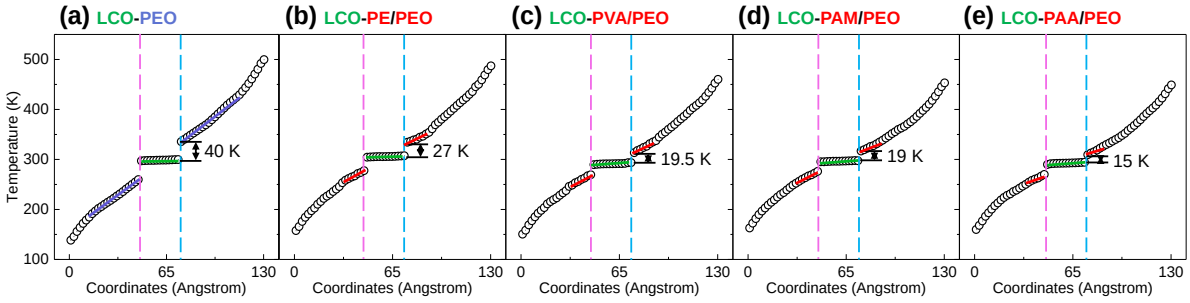

Figure B.2. RNEMD temperature profiles for (a) LCO/PEO, (b) LCO-PE/PEO, (c) LCO-PVA/PEO, (d) LCO-PAM/PEO and (e) LCO-PAA/PEO. Only the left part is shown due to the symmetric simulation system. Between the two vertical dashed lines is the LCO

crystal. At the two sides is PEO or PEO with SAM chains.

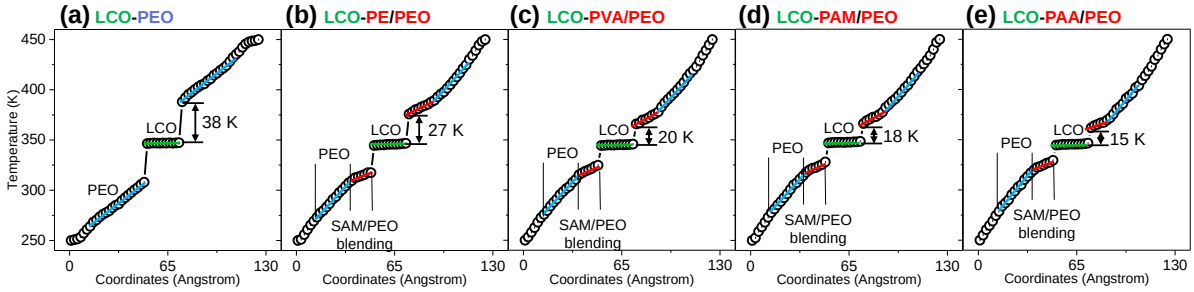

Figure B.3. NEMD temperature profiles of (a) LCO/PEO, (b) LCO-PE/PEO, (c) LCO-PVA/PEO, (d) LCO-PAM/PEO and (e) LCO-PAA/PEO.

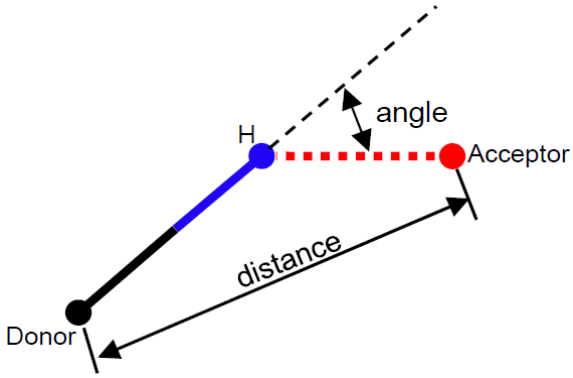

Figure B.4. A H-bond is identified with the following criteria: (1) the distance between the H-bond donor (D) and acceptor (A) is not longer than 3.0 Å; and (2) the angle between H-donor and H-acceptor is not larger than 20˚.

APPENDIX C

SUPPLEMENTAL MATERIAL OF CHAPTER 4

C.1

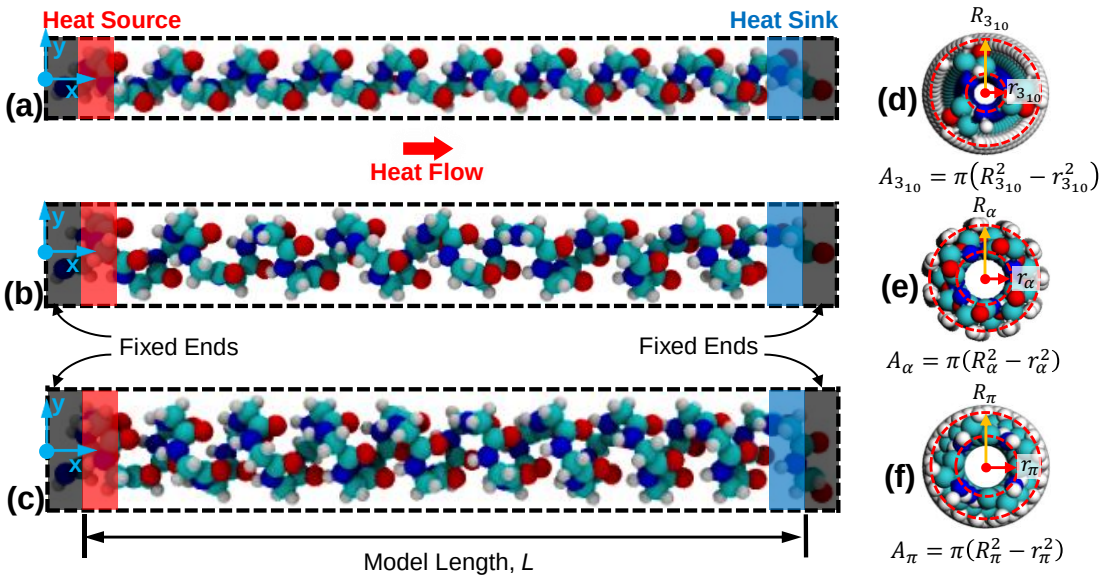

Figure C.1. Setup of the NEMD simulation for predicting thermal conductivities of the (a) 3_{10}-, (b) α-, and (c) π-helices. Heat flow is generated by adding energy into the heat source (red region) and removing the same amount of energy from the heat sink (blue region). *L* is the characteristic length. The simulation cell is divided into *N* slabs. The two end slabs are fixed for heat insulation. Periodic boundary conditions are applied along all three directions. Cross-sectional view of the (d) 3_{10}-, (e) α-, and (f) π-helix models. The cross-sectional area is calculated using averaged inner and outer radii of the helices.

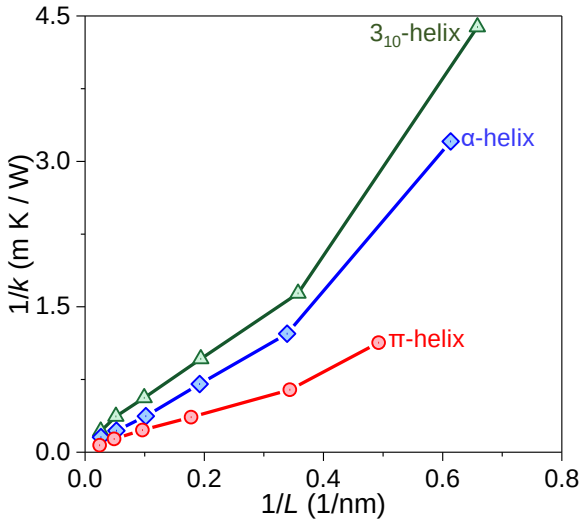

Figure C.2. Inverse of thermal conductivity versus inverse of length for the isomer helices.

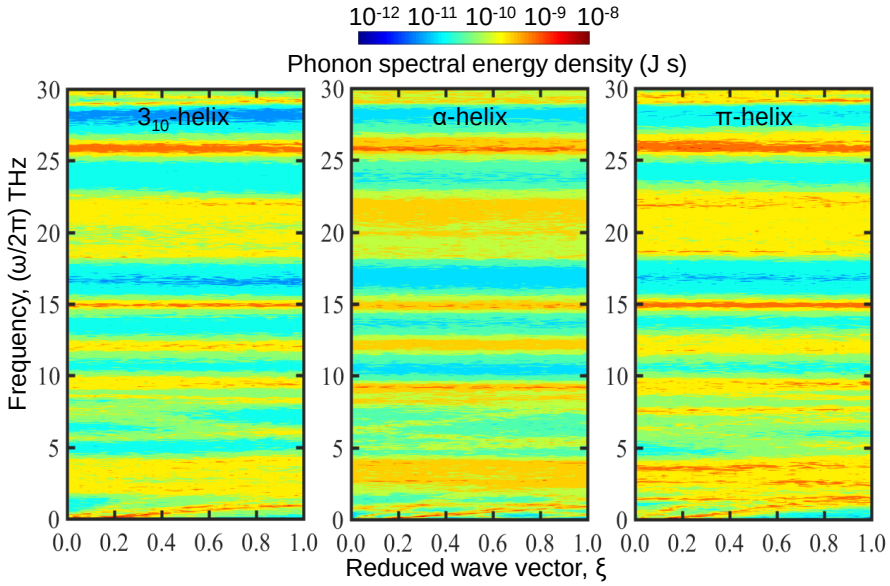

Figure C.3. Phonon spectral energy density for the three isomer helices at T = 298 K. Shading on these plots represents the magnitude of phonon spectral energy density for different phonon mode combining specific $\boldsymbol{\kappa}$ and ω.

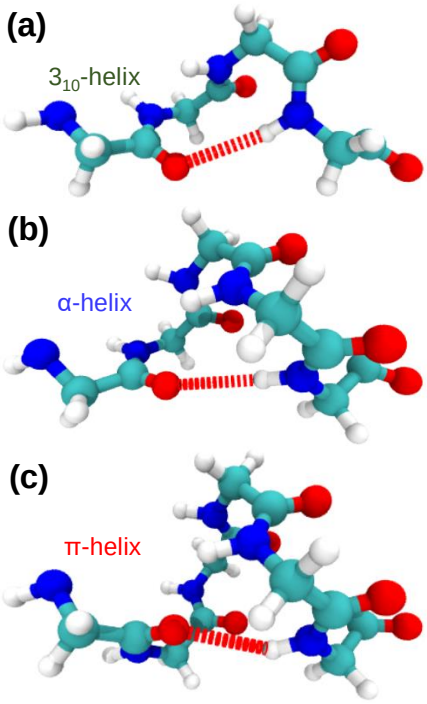

Figure C.4. Intercepted helices for DFT-based quantum-chemical analysis of H-bond: (a) the 3_{10}-helix segment has four residues; (b) the α-helix segment has five residues; and (c) the π-helix segment has six residues.

CURRICULUM VITAE

Jinlong He

Education

- **Ph.D.** in **Mechanical Engineering**

  Utah State University, Logan, UT, November 2020

  — Dissertation: Molecular Mechanisms and Design of Hydrogen-Bonded Materials for Thermal Applications

  — Advisor: Dr. Ling Liu

- **M.S.** in **Civil Engineering**

  Southwest Jiaotong University, Chengdu, China, June 2012

  — Thesis: Anti-seismic Performance Analysis for Long-span Steel Truss Deck-Type Railway Arch Bridge

  — Advisor: Dr. Yongjiu Qian

- **B.S.** in **Civil Engineering**

  Southwest Jiaotong University, Chengdu, China, June 2009

  — Thesis: Design and Load Test for Highway Prestressed Concrete Continuous Rigid Frame Bridge

  — Advisor: Dr. Rui Kang and Dr. Keyue Zhang

Journal Publications

- **He, J.**, Zhang, L., and Liu, L., "Tuning Thermal Transport of Helical Protein Nanotudes through Side-Chain Mass Modification," (To be Submitted)
- **He, J.**, Alden, A., Cui, X., Lua, J., Liu, L., Effects of Manufacturing-Induced Residual Thermal Stress on Strength of Unidirectional Fiber-Reinforced Composites with Microvoids," (To be Submitted)
- **He, J.**, Zhang, L., and Liu, L., "Hydrogen-Bond Configuration Modulates Energy Transfer Efficiency in Helical Protein Nanotubes," (**Nanoscale**, Under Revision)
- **He, J.**, Zhang, L., and Liu, L., 2020, "Improving thermal conduction across cathode/electrolyte interfaces in solid-state lithium-ion batteries by hierarchical hydrogen bond network,“ **Materials & Design**, 194, pp.108927
- Alden, A., **He, J.**, Cui, X., Lua, J., Liu, L., 2020, "Effects of microvoids on strength of unidirectional fiber-reinforced composite materials," **Composites Part B: Engineering**, 187, pp. 107844
- **He, J.**, Zhang, L., and Liu, L., 2019, "Thermal transport in monocrystalline and polycrystalline lithium cobalt oxide," **Physical Chemistry Chemical Physics**, 21(23), pp. 12192-12200.

Positions Held

- **Graduate Research Assistant**

  — MAE Department, Utah State University, Logan, UT

01/2018 – Present

— Civil Engineering, Southwest Jiaotong University, Chengdu, China

09/2012 – 12/2016

- **Graduate Teaching Assistant**

— MAE Department, Utah State University, Logan, UT

12/2016 – 05/2017 Fracture Mechanics

09/2017 – 12/2017 Solid Mechanics

Outreach

Tutor of Native American STEM Mentorship Program, 2017, 2018